

STUDY OF MAGNETIC PROPERTIES OF NANOSTRUCTURES ON SELF-ASSEMBLED PATTERNS

THOMAS MALWELA

A thesis submitted in partial fulfillment
of the requirements for the degree of

Magister of Scientiae



**DEPARTMENT OF PHYSICS
UNIVERSITY OF THE WESTERN CAPE**

**Supervisor: Prof. K. T. Hillie, Council for Scientific and Industrial
Research**

**Co-supervisor: Prof. M. B. Tchoula Tchokonte, University of the
Western Cape**

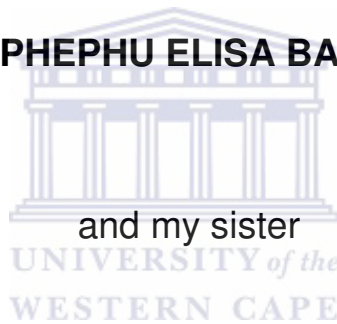
DATE SUBMITTED: FEBRUARY 2010

I dedicate this thesis to my wife

MASHUDU FAITH MUDZUNGA

my mother

MPHEPHU ELISA BALOYI



and my sister

TSAKANI MARGRET BALOI

for making me realize my potentials and their unlimited
support.

KEYWORDS

“STUDY OF MAGNETIC PROPERTIES OF NANOSTRUCTURES ON SELF-ASSEMBLED PATTERNS”

THOMAS MALWELA

Self-Assembly

Aluminium Anodization

Nanopores

Electrodeposition

Cyclic Voltammetry

Co nanostructures

MnO_x (x = 1,2) nanostructures

Nanomagnetism

Atomic Force Microscopy

Magnetic Force Microscopy

Magnetic properties

Magnetic domains

Domain Walls

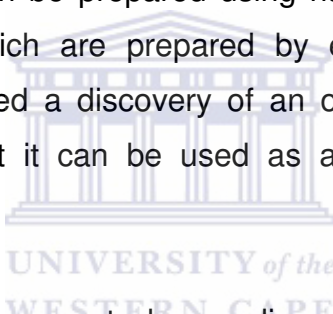


ABSTRACT

“STUDY OF MAGNETIC PROPERTIES OF NANOSTRUCTURES ON SELF-ASSEMBLED PATTERNS”

T. MALWELA

The fabrication of ordered magnetic nanostructured materials have attracted a lot of interests in nanotechnology due to their unique electronic and optoelectronic properties which differ from the same bulk materials. These ordered nanostructured materials can be prepared using nanoporous anodic aluminium oxide (AAO) templates which are prepared by electrochemical oxidation of aluminium foils. This followed a discovery of an ordered pore arrangement in porous anodic alumina that it can be used as a template for nanostructure fabrication.



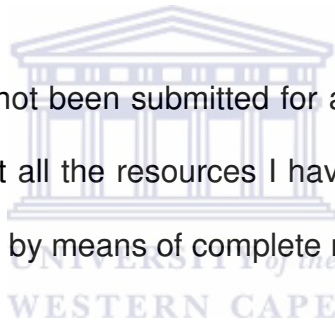
In the current study, we give a report when oxalic acid was used as an electrolyte to synthesize an AAO template with hexagonal pore array. Optimum parameters were observed as 0.4 M of oxalic acid, anodizing voltage of 45 V, temperature of approximately 8 °C and the period of 120 minutes. Atomic force microscope (AFM) and High resolution scanning electron microscope (HRSEM) showed that template has an average pore diameter of 103 nm. Co and MnO_x (x = 1,2) nanostructures were selectively deposited in the pores of the template using a novel atomic layer deposition (ALD) technique. The diameter sizes and the array of the nanostructures and the template were corresponding. Energy dispersive x-rays (EDX) and X-ray photoelectron spectroscopy (XPS) confirmed the presence of Co and MnO_x (x =1,2) on the samples while x-ray diffraction (XRD) provided an indication of their orientations. Magnetic force microscopy as main characterization tool showed the existence of multi-domains on both Co and MnO_x (x =1,2) nanostructures.

DECLARATION

I declare that

***“STUDY OF MAGNETIC PROPERTIES OF
NANOSTRUCTURES ON SELF-ASSEMBLED
PATTERNS”***

is my own work, that it has not been submitted for any degree or examination in any other university and that all the resources I have used or quoted have been indicated and acknowledged by means of complete references.



Thomas Malwela

Signed:

ACKNOWLEDGEMENTS

I would like to appreciate the following people and the institutions contributed to the success of this work through their advices, guidance and encouragements.

Prof. Thembela Hillie (NCNSM, CSIR) for the outstanding supervision of the dissertation, guidance and countless fruitful discussions.

Prof. Moise Tchoula Tchokonte (Department of Physics, University of the Western Cape) who acted as co-supervisor, for his continuous support, guidance and fruitful discussions.

Mr. T. Mkwizu (EAP, MSM, CSIR) for technical support, advices and guidance on the electrochemistry part of the study.

Dr. Simon Dlamini (NCNSM, CSIR) who constantly provided advices, guidance and unbounded support.

Dr. Gerald Malgas (NCNSM, CSIR) for the undivided guidance, encouragement and support.

Mr. Manfred Scriba (NCMSM, CSIR) for technical contributions.

National Centre for Nano-Structured Materials of the CSIR for offering the opportunity to conduct research at the institution.

Mashudu for your love, inspiration and support when much needed.

My family and friends for their constant love, support, inspiration and encouragement.

My sister, Margret, who made me realize my potentials and the lovely support she displayed.

My mother for always believing in me and the unlimited love.

Group fellows, Gebhu, Gugu and Sibusiso who were always available for the support and discussion when much needed.

Joseph, Grace, Irene, Collen, Ellen, Daphney, Martha and Gladwin for the lovely support.

National Centre for Nano-Structured Materials (CSIR), Department of Science and Technology and University of the Western Cape for the financial support during the study.

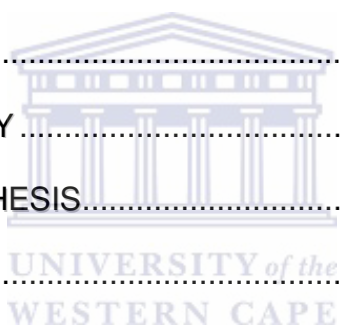


Finally I would like to thank God, the source of wisdom and knowledge.

THANK YOU

CONTENTS

TITLE	i
KEYWORDS	iii
ABSTRACT	iv
DECLARATION	v
ACKNOWLEDGEMENTS	vi
CHAPTER ONE: INTRODUCTION.....	1
1.1. OVERVIEW	1
1.2. AIMS OF THE STUDY	6
1.3. OUTLINE OF THE THESIS.....	7
REFERENCES	8
CHAPTER TWO: THEORETICAL BACKGROUND.....	13
2.1. MAGNETISM	13
2.1.1. Introduction	13
2.1.2. Origin of magnetism.....	14
2.1.2.1. Diamagnetism	16
2.1.2.2. Paramagnetism.....	17
2.1.2.3. Ferromagnetism.....	18
2.1.2.4. Ferromagnetic Domains.....	19
2.1.2.5. Antiferromagnetism.....	21



2.1.2.6. Anisotropy Energy	22
2.1.3. The Theory of Magnetic Force Microscopy.....	23
2.2. ELECTROCHEMICAL CELL.....	24
2.2.1. Electrolytes	26
2.2.2. Electrodes.....	26
2.3. ALUMINIUM ANODIZATION.....	28
2.4. ANODIZATION PARAMETERS	31
2.4.1. Pre – treatment of Aluminium foil.....	31
2.4.2. Anodization voltage	31
2.4.3. Anodizing time	32
2.4.4. Type of electrolyte and the concentration	32
2.4.5. Temperature	33
2.5. ELECTRODEPOSITION.....	33
REFERENCES	37
CHAPTER THREE: EXPERIMENTAL DETAILS	40
3.1. EXPERIMENTAL PROCEDURES	40
3.1.1. Pre – treatment of Aluminium	40
3.1.2. Aluminium Anodization	40
3.1.3. Electrodeposition on Anodized Alumina.....	41
3.1.3.1. Electrochemical Bath Deposition	41
3.1.3.1.1. Cyclic Voltammetric (CV) Measurements	42
3.1.3.1.2. Procedure for Manganese Oxide Deposition.....	43

3.1.3.2.	Flow-cell Based Electrodeposition	43
3.1.3.2.1.	Procedure for Cobalt Deposition.....	44
3.2.	EXPERIMENTAL TECHNIQUES	45
3.2.1.	Atomic Force Microscopy (AFM).....	45
3.2.1.1.	Static Mode.....	47
3.2.1.2.	Dynamic Mode.....	48
3.2.1.2.1.	Non-Contact Mode	48
3.2.1.2.2.	Intermittent Mode	48
3.2.1.3.	AFM's Tip Artefacts.....	49
3.2.2.	Magnetic Force Microscopy (MFM).....	50
3.2.2.1.	Magnetic Force Imaging	50
3.2.3.	Scanning Electron Microscopy.....	53
3.2.3.1.	Introduction.....	53
3.2.3.2.	Resolution.....	54
3.2.3.3.	Depth of Field and Working Distance	54
3.2.3.4.	Secondary Electrons.....	56
3.2.3.5.	Effect of Accelerating Voltage.....	58
3.2.3.6.	X-Ray Emission	58
3.2.4.	X-ray Diffraction.....	59
3.2.4.1.	Introduction	59
3.2.4.2.	Crystal Lattice	60
3.2.4.3.	Bragg's Law	60
3.2.5.	X-ray Photoelectron Spectroscopy (XPS).....	61

3.3.	CHARACTERIZATION.....	62
3.3.1.	Atomic Force Microscopy (AFM).....	62
3.3.2.	Magnetic Force Microscopy (MFM).....	63
3.3.3.	Scanning Electron Microscopy (SEM).....	63
3.3.4.	X-Ray Diffraction (XRD).....	64
3.3.5.	X-Ray Photoelectron Spectroscopy (XPS).....	64
	REFERENCES	65
	 CHAPTER FOUR: ALUMINIUM ANODIZATION	67
4.1.	INTRODUCTION.....	67
4.2.	RESULTS AND DISCUSSION.....	68
4.2.1.	Anodization.....	68
4.2.2.	Electrodeposition of Cobalt.....	79
4.2.3.	Electrodeposition of Manganese oxide	87
4.3.	CONCLUSION	94
	REFERENCES	96
	 CHAPTER FIVE: MFM ANALYSIS	97
5.1.	INTRODUCTION.....	97
5.2.	RESULTS AND DISCUSSION	98
5.2.1.	MFM analysis on Co nanostructures	98
5.2.2.	MFM analysis on MnO _x (x = 1,2) nanostructures.....	104
5.3.	CONCLUSION	106

REFERENCES	108
CHAPTER SIX: CONCLUSION	109
APPENDIX A	113

LIST OF TABLES AND FIGURE CAPTIONS

Figure 2. 1: Demonstration of the magnetic moment associated with (a) an orbiting electron and (b) spinning electron.....	14
Figure 2. 2: The atomic dipole configuration for a diamagnetic material which opposes the applied magnetic field.	16
Figure 2. 3: The atomic dipole configuration for a (a) paramagnetic material without and (b) with external magnetic field.....	17
Figure 2. 4: The atomic dipole for a ferromagnetic material which exists in the absence of an applied external field and in the presence of the external field.....	18
Figure 2. 5: Schematic of a ferromagnet showing four domains with zero net magnetization.	19
Figure 2. 6: (a) illustrates the magnetic domains with randomly oriented spins and (b) magnetic domains with spins aligned in the direction of an externally applied magnetic field.....	20

Figure 2. 7: Schematic representation of the change in movement orientation within a 180° Bloch wall [2.5].	20
Figure 2. 8: A schematic showing how ferromagnetic domains respond to the external magnetic field.	21
Figure 2. 9: The atomic dipole configuration for an antiferromagnetic magnetic material showing a zero net magnetic moment.	22
Figure 2. 10: Schematic diagram of the electrochemical cell set – up.	25
Figure 2. 11: Schematic structure of anodic alumina [2.13]	28
Figure 2. 12: Approximate regions in which various steps of ion transport occurs leading to electrodeposition [2.27].	36
Figure 3. 1: Three-electrode set up used in electrodeposition and cyclic voltammetric investigations.	42
Figure 3. 2: Schematic diagram of automated flow-cell electrodeposition system [3.3].	44
Figure 3. 3: Schematic diagram of atomic force microscope [3.6].	46
Figure 3. 4: Inter-atomic force as function of distance graph.	47
Figure 3. 5: Image artefact caused by contaminated tip.	49
Figure 3. 6: MFM Lift Mode principle demonstrated on a sample with blue areas representing regions which are magnetic.	51
Figure 3. 7: Schematic diagram of the signals generated during the incident beam – sample interaction.	53

Figure 3. 8: The effect of the working distance on the depth of field seen for the specimen.	55
Figure 3. 9: The influence of working distance on the amount of spherical aberration and resolution of the final image.....	56
Figure 3. 10: Energy distribution of secondary electrons [3.7].	57
Figure 3. 11: Characteristic x-ray emission by an atom.	58
Figure 3. 12: Geometrical illustration of the Braggs' Law [3.9].....	61
Figure 4. 1: AFM height images of aluminium anodized at (a) 40 V, (b) 45 V and (c) 50 V in 0.4 M Oxalic for 20 minutes at approximately 18 °C. ...	69
Figure 4. 2: HRSEM images of anodized Al foil in 0.4M oxalic acid at (a) 40 V, (b) 45 V and (c) 50 V for 20 minutes at approximately 18 °C respectively.	72
Figure 4. 3: (a) AFM height image and (b) its 3D surface plot of aluminium anodized at 45 V in 0.4 M Oxalic for 60 minutes at approximately 8 °C respectively.	74
Figure 4. 4: SEM (a) cross-section view and (b) the peeled area of anodized Al foil in 0.4M oxalic acid at 45 V for 60 minutes at approximately 8 °C respectively.	76
Figure 4. 5: (a) AFM height image and (b) its 3D surface plot of aluminium anodized at 45 V in 0.4 M Oxalic for 120 minutes at approximately 8 °C respectively.	77

Figure 4. 6: SEM images of anodized Al foil in 0.4M oxalic acid at 45 V for 120 minutes at approximately 8 °C.....	78
Figure 4. 7: AAO template coated at the back by Au-Pd film and supported by copper adhesive tape.	79
Figure 4. 8: Cyclic voltamogram on aluminium foil (unanodized) measured in solution containing 0.12 M CoSO ₄ + 0.49 M H ₃ BO ₃ at pH 5.	80
Figure 4. 9 : Cyclic voltamogram on anodized alumina coated with Au-Pd film measured in solution containing 0.12 M CoSO ₄ + 0.49 M H ₃ BO ₃ at pH 5.....	81
Figure 4. 10: AFM height topography (a) and SEM top view (b) of cobalt nanostructures prepared on AAO template from a mixture of 0.12 M CoSO ₄ and 0.49 M H ₃ BO ₃ applying the voltage of -1.1 V.....	82
Figure 4. 11: EDX spectrum of cobalt nanostructures prepared on AAO template from a mixture of 0.12 M CoSO ₄ and 0.49 M H ₃ BO ₃ applying the voltage of -1.1 V.	84
Figure 4. 12: XRD pattern of cobalt nanostructures prepared on AAO template from a mixture of 0.12 M CoSO ₄ and 0.49 M H ₃ BO ₃ applying the voltage of -1.1 V.	85
Figure 4. 13: XPS spectra Co nanostructures prepared on AAO template from a mixture of 0.12 M CoSO ₄ and 0.49 M H ₃ BO ₃ applying the voltage of -1.1 V.....	86

Figure 4. 14: A zoomed XPS spectra from the one in figure 4.13 of Co nanostructures with peaks corresponding to reference spectra of Co.....	87
Figure 4. 15: Cyclic voltammogram on anodized alumina coated with Au-Pd film measured in a solution containing 0.3 M of manganese (II) chloride tetrahydrate ($\text{MnCl}_2 \cdot 4\text{H}_2\text{O}$).....	88
Figure 4. 16: AFM height topography (a) and SEM top view (b) of MnO_x ($x = 1,2$) nanostructures prepared on AAO template from a solution of 0.3 M $\text{MnCl}_2 \cdot 4\text{H}_2\text{O}$ when the voltage was set to +1.1 V.	89
Figure 4. 17: EDX spectrum of MnO_x ($x = 1,2$) nanostructures prepared on AAO template from a solution of 0.3 M $\text{MnCl}_2 \cdot 4\text{H}_2\text{O}$ when the voltage was set to +1.1 V.	90
Figure 4. 18: XRD pattern of MnO_x ($x = 1,2$) nanostructures prepared on AAO template from a solution of 0.3 M $\text{MnCl}_2 \cdot 4\text{H}_2\text{O}$ when the voltage was set to +1.1 V.	91
Figure 4. 19: XPS spectra MnO_x ($x = 1,2$) nanostructures prepared on AAO template from a solution of 0.3 M $\text{MnCl}_2 \cdot 4\text{H}_2\text{O}$ when the voltage was set to +1.1 V.	92
Figure 4. 20: A zoomed XPS spectra from the one in figure 4.16 of MnO_x ($x = 1,2$) nanostructures with peaks corresponding to reference spectra of MnO_2	93

Figure 5. 1: (a) AFM height topography, (b) the corresponding MFM image and (c) a zoomed area from the square box on an MFM image of cobalt nanostructures prepared on AAO template imaged at the lift scan height of 5 nm.....99

Figure 5. 2: (a) Line profile of the image contrast taken along a line perpendicular to a dark contrast, measured on the nanostructure marked “A” in figure 5.1 and (b) represents both the attractive (upwards arrows) and repulsive (downwards arrows) interactions on the nanostructure..... 100

Figure 5. 3: (a) AFM height topography, (b) the corresponding MFM image and (c) a zoomed area of an MFM image of cobalt nanostructures prepared on AAO template imaged at the lift scan height of 4 nm.....102

Figure 5. 4: (a) Line profile of the image contrast taken along a line perpendicular to the wall, measured on the nanostructure marked “B” in figure 5.3 (b) illustrates both the attractive (upwards arrows) and repulsive (downwards arrows) interactions on the nanostructure..... 103

Figure 5. 5: (a) AFM height topography, (b) the corresponding MFM image and (c) a zoomed area from a square box on an MFM image of MnO_x (x = 1,2) nanostructures prepared on AAO template imaged at the lift scan height of 8 nm. 104

Figure 5. 6: (a) Line profile of the image contrast taken along a line perpendicular to the wall, measured on the nanostructure marked “B” in figure 5.3 (b) illustrates both the attractive and repulsive interactions on the nanostructure..... 105

Table 4. 1: Influence of anodizing potential to pore diameters and depths. 73



CHAPTER ONE: INTRODUCTION

1.1. OVERVIEW

Unknowingly to researchers the concept of nanotechnology has been the subject of research for the past few decades. More interests and investigations on the subject gained momentum after Eric Drexler (1981) suggested the term ‘nanotechnology’, which was inspired by Richard Feynman’s (1959) concept on atomic manipulation and nano-factories [1.1]. Materials at nano-scale level show interesting properties due to quantum confinement, physical proximity and self-organization [1.2]. These include nano-scaled magnetic materials in which a single domain can be formed in the absence of external fields. Immediately after the fabrication, the structure becomes a magnetic dipole [1.3]. This opened new research opportunities in the science and engineering of materials, especially when assembling nano-scale structures and fabricating nano-devices [1.4]. These nano-scale structures have potential applications in various areas of nanotechnology such as photonics [1.5], electronics [1.6], magnetic storage devices [1.7], etc.

Nano-scale magnetism is one of the subjects that received interest since the nineteen fifties due to the desire to fabricate denser and reliable recording media for the recording industry [1.8]. When the magnetic particles become smaller, their storage densities increase. The quest to have single domains, thus below 40 nm in bulk, is important for new spin technologies [1.9]. Recently, the Nobel Prize winners in physics Albert Fert and Peter Grunberg in 2007

discovered giant magnetoresistance (GMR) [1.10]. They studied the resistance brought by spin up and spin down of electrons when the electric current is passed through multilayers (i.e. ferromagnetic/nonmagnetic/ferromagnetic layer). The remarkable discovery widened scientific and technological opportunities including an intense influence on the technique of data storage and magnetic sensors. The advent of nanotechnology will turn the driving force of GMR for new applications. Fabricating a large array of nano-scale magnetic elements and tailoring brought new challenges on developing nano-patterning techniques for synthesizing these nanostructures [1.5]. The techniques should be able to fabricate ordered arrays of nanostructures with controllable size, shape and spacing [1.11, 1.12].

However, there are two approaches for synthesizing these nanostructures which include the bottom-up and top-down synthesis. The bottom-up approach involves understanding the building blocks of nano-scale structures, i.e. building atom by atom or molecule by molecule [1.13]. The types of bottom-up approaches include self-organized growth, self-assembled growth and the template-assisted growth. The self organized growth is driven by the kinetic energy and depends on the flux of the materials to be deposited, the state and the orientation of the substrate [1.14]. The self-assembled growth is more thermodynamically dependent where molecules diffuse from high concentration to low concentration [1.14]. Recently self-assembly has been used in the synthesis of nanostructures at the liquid-liquid surfaces using phase change catalysis [1.15]. The template assisted growth (patterning) uses a template to

control the shape, size, spacing and the array of the nanostructure [1.16]. Our study mainly focuses on the template assisted growth as a nano-patterning method.

It should be noted that there are different types of nano-patterning methods developed for synthesizing nanostructure arrays which involves lithographic methods such as electron-beam [1.17], ion-beam [1.2] and X-rays [1.18]. Other methods of patterning that include self-assembly processes utilize diblock-copolymers [1.19, 1.20, 1.21]. These methods have been employed to fabricate nanostructures with controlled size, shape and spacing. Some of these methods have their drawbacks, e.g. e-beam lithography can easily write hundreds or thousands of nanodot patterns with great accuracy and without complications but writing hundred millions of nanodots is a process that take time and also limited by a microscope's field of view [1.11]. On the hand, the self-assembly process is limited to the classes of materials and produces nanostructures with poor controlled spatial and size distribution. Another commonly employed template is the track etched polymeric membranes which are commercially available [1.19]. A membrane with variety of pore sizes can be produced but these pores are randomly distributed with low porosity.

Due to these limitations, anodic aluminium oxide (AAO) with a highly ordered hexagonal pore distribution which is characterized by flexibility, high throughput and high structural controllability emerged as the favourable template [1.16]. It is a cost effective technique which can be easily assembled and be up scaled in a laboratory. This patterning technique has been a subject of interest

for several decades and was found to be an ideal template due to the highly ordered pore distribution [1.22]. The AAO template can be synthesized by anodizing the aluminium foil. These porous anodic aluminium oxide templates are prepared by electrochemical oxidation of high purity aluminium foils (99.99%) in which a two-step anodization is carried out in acidic solutions [1.22, 1.23, 1.24, 1.25, 1.26]. The porous structure exhibits hexagonally arranged cells with cylindrical pores in the centre. The pores are perpendicular to the surface of aluminium foil [1.27]. Aluminium anodization showed that by varying anodization parameters, hexagonal close-packed arrays with controllable variation of pore diameters, depths and spacing can be produced [1.22, 1.28, 1.29, 1.30, 1.31]. These anodization parameters include voltage, time, type of electrolyte (acid) and its concentration; and temperature. For example, sulphuric acid prepares pores with smaller diameter (10-30 nm), oxalic acid prepares the medium sized pores (30-80 nm) and phosphoric acid prepares large pores (larger than 80 nm) [1.16]. The anodizing voltage was found to have more influence on pore diameters than the electrolyte, time and temperature [1.32]. O'Sullivan et al [1.33] observed the linear relationship between the anodizing potentials and pore diameters, when forming alumina at various voltages in the range of 80 to 120 V for 1 h in 0.4 M phosphoric acid. It is therefore vital to optimize the anodizing parameters in order to fabricate the AAO template desired uniform hexagonal pore distribution and size.

Previous research on AAO template shows that it has been successfully used as a pattern transfer when synthesizing nickel nano-metals [1.34,1.35,

1.36], cobalt nanowires **[1.37, 1.38]**, carbon nanotubes transistor **[1.39]**, metal nanodots and nanorods **[1.40]**. In the preparations of all these materials, AAO templates showed a diverse compatibility when used as a starting material. Some of these nano-metals were fabricated using standard electrodeposition techniques **[1.36, 1.41, 1.42]**. For electrodeposition, the back side of the template was coated with a conductive layer that serves as an electrode during deposition **[1.43]** and due to the non-conductivity of the alumina, deposition selectively takes place in the pore that are exposed to the electrolyte **[1.22]**.

The current study will utilize AAO template for the deposition of magnetic (Co and MnO_x ($x = 1,2$)) nanostructures using a novel electrochemical deposition technique in which materials grow layer by layer **[1.44]**.

Atomic force microscopy (AFM) will be used to study the topographic feature of both AAO template and deposited nanostructures. AFM is a versatile technique that uses a sharp tip to image both conducting and non-conducting samples providing atomic resolution, 3-D images of sample surfaces in ambient, vacuum and liquid environments **[1.45]**. This technique was developed by Binnig *et al.* (1985) **[1.46]** to detect ultra small forces at nano-Newton range acting between the tip and the sample surface. AFM can be operated in static or dynamic mode. It is nondestructive technique which has been used to study a wide range of materials which includes biological materials **[1.47]**, polymeric materials **[1.48]** and semiconductors **[1.49]**. Magnetic force microscopy (MFM) is a special mode of AFM that uses a tip coated with ferromagnetic material to detect the magnetic interaction between the tip and the sample. With a typical

MFM, domains with resolution of 100 nm can be imaged [1.50]. However, imaging domains with the maximum resolution of about 10 nm has been reported on the work already done on the subject [1.51]. In this study, magnetic force microscopy (MFM) will be employed to investigate the magnetic behavior of Co and MnO_x ($x = 1,2$) nanostructures prepared on AAO templates.

1.2. AIMS OF THE STUDY

In this study, the combinations of anodizing parameters suitable for producing a highly ordered hexagonal nanoporous alumina structure (AAO template) via aluminium anodization will be investigated. Using a two-electrode electrochemical cell, anodizing parameters will be varied and optimized. The deposition of these magnetic nanostructures will be done using a novel electrochemical atomic layer deposition (EC-ALD). Electrodeposition parameters will also be optimized to ensure that deposition of Co and MnO_x ($x = 1,2$) nanostructures selectively take place in the pores of AAO template and to determine the length of the deposit.

Atomic force microscopy will be used to examine the topography while magnetic force microscopy (MFM) will be employed to study the magnetic domains/collective behavior of these magnetic nano-materials. Techniques such as X-ray diffraction (XRD) will be employed for quantitative analysis while X-ray photoelectron spectroscopy (XPS) and energy dispersive X-rays (EDX) will be used for compositional analysis. Scanning electron microscopy (SEM) will also be used to study the morphology.

1.3. OUTLINE OF THE THESIS

Chapter two will provide a theory on magnetism and the classes of magnetic properties, magnetic force microscopy (MFM), electrochemical cell and its constituents will be discussed in detail. Aluminium anodization together with the parameters that govern anodizing experiments will be covered. This will be followed by a brief discussion on electrodeposition and the factors needed to be considered prior deposition.

Chapter three will discuss the experimental procedures used for aluminium anodization and synthesizing magnetic nanostructures. A discussion on how AFM is operated and the types of operational modes will be covered followed by a brief description of MFM as a technique of choice will be used to study the physical properties. A brief discussion on techniques such as scanning electron microscopy, XRD and XPS will be provided.

Chapter four will give report on optimum parameters found during the synthesis of AAO templates and the electrodeposition of Co and MnO_x ($x = 1,2$) nanostructures. SEM, EDX and XPS results will be provided.

Chapter five provides the MFM results and interpretations.

Chapter five will give the conclusion and future work.

REFERENCES

- [1.1]. K. E. Drexler, Engines of Creation: The Coming Era of Nanotechnology, Anchor Books, 1986
- [1.2]. A. D. Yoffe, Advances in Physics, Vol. 42, No. 2 (1993) 173 – 266
- [1.3]. S. Y. Chou, Proceedings of the IEEE, Vol. 85, No. 4 (1997) 652 – 671
- [1.4]. C. Dupas, P. Houdy, M. Lahmani, Nanoscience – Nanotechnologies and Nanophysics, Springer, 2006
- [1.5]. H. Chik, J. M. Xu, Materials science and engineering, R 43 (2004) 103 – 138
- [1.6]. D. Goldhaber-Gordon, M. S. Monternerlo, J. C. Love, G. J. Opiteck, J. C. Ellenbogen, Overview of Nanoelectronic devices, Published in The Proceedings of the IEEE (1997)
- [1.7]. B. Aktas, L. Tagirov, F. Mikailov, Magnetic Nanostructures, Springer, 2007
- [1.8]. Z. L. Wang, Characterization of Nanophase Materials, Wiley-VCH Verlag, GmbH, 2000
- [1.9]. S.A. Koch, R.H. te Velde, G. Palasantzas, J.Th.M. De Hosson, Applied Surface Science 226 (2004) 185–190
- [1.10]. The Discovery of Giant Magnetoresistance, Compiled by the Class for Physics of the Royal Swedish Academy of Sciences, 2007
- [1.11]. G. Cao, D. Liu, Advances in Colloid and Interface Science, 136 (2008) 45 – 64
- [1.12]. Y. Piao, H. Lim, J. Y. Chang, W. Lee, H. Kim, Electrochimica Acta, 50 (2005) 2997 – 3013

- [1.13]. N. Yao, Z. L. Wang, Handbook of Microscopy for Nanotechnology, Kluwer academic publishers, 2005
- [1.14]. J. V. Barth, G. Cstantini, K. Kern, Nature, vol. 437 (2005),
doi:10.1038/nature04166
- [1.15]. S. N. Mlondo, P. J. Thomas, P. O'Brien, J. AM. Chem., Soc., 131 (2009)
6072 – 6073
- [1.16] Y. Lei, W. Cai, G. Wilde, Progress in materials science, 52 (2007) 465 –
539
- [1.17]. W. B. Choi, J. U. Chu, K. S. Jeong, E. J. Bae, J. W. Lee, J. Kim, J. O. Lee,
Appl. Phys. Lett., Vol. 79, No. 22 (2001) 3696 – 3698
- [1.18]. W. Chu, H. I. Smith, M. L. Schattenburg, Appl. Phys. Lett. Vol. 59, No.13
(1991) 1641 – 1643
- [1.19]. C. R. Martin, Science, Vol. 266 (1994) 1961 – 1966
- [1.20]. M. Lazzari, M. A. Lopez-Quintela, Adv. Mater., Vol. 15, No. 19 (2003) 1 –
12
- [1.21]. T. Thurn-Albrecht, J. Schotter, G. A. Kastle, N. Emley, T. Shibauchi, L.
Krusin-Elbaum, K. Gaurini, C. T. Black, M. T. Tuominen, T. P. Russel,
Science, Vol. 290 (2000) 2126 – 2129
- [1.22]. H. Masuda, K. Fakuda, Science, Vol. 268 (1995), 1466 – 1468
- [1.23]. A. P. Li, F. Muller, A. Birner, K. Nielsch and U. Gosele, J. Appl. Phys, Vol.
84, No. 11 (1998) 6023 – 6026
- [1.24]. O. Jessensky, F. Muller and U. Gosele, Appl. Phys. Lett. Vol. 72, No. 10
(1998) 1173 – 1175

- [1.25]. G. D. Sulka, S. Stroobants, V. Moshchalkov, G. Borghs, J. –P. Celis, J. Electrochemical Society, Vol. 149, No. 7 (2002) D97 – D103
- [1.26]. N. V. Myung, J. Lim, J. –P. Fleurial, M. Yun, W. West, D. Choi, Institute Of Physics Publishing, Nanotechnology ,15 (2004) 833 – 838
- [1.27] H. Masuda, H. Yamada, M. Satoh, H. Asoh, N. Nakao, T. Tamamura, Appl. Phys. Lett. Vol. 71, No. 19 (1997) 2770 - 2772
- [1.28]. Y. F. Mei, X. L. Wu, T. Qiu, X. F. Shao, G. G. Siu, P. K. Chu, Thin Solid Films, 492 (2005) 66 – 70
- [1.29]. A. Bai, C. Hu, Y. Yang, C. Lin, Electrochemi. Acta (2007), doi: 10.1016/j.electacta.2007.09.039
- [1.30]. B. –Y. Yoo, R. K. Hendricks, M. Ozkan, N. V. Myung, Electrochimica Acta, 51 (2006) 3543 – 3550
- [1.31]. L. Ba, W. S. Li, J. Phys. D: Appl. Phys., 33 (2000) 2527 – 2531
- [1.32]. G. D. Sulka, K. G. Parkola, Electrochimica Acta, 52 (2007) 1880 – 1888
- [1.33]. J. P. O’Sullivan, G. C. Wood, Proc. Roy. Soc. Lond. A., 317 (1970) 511 – 543
- [1.34]. G. P. Sklar, K. Paramguru, M. Misra, J. C. LaCombe, Nanotechnology, 16 (2005) 1265 – 1271
- [1.35]. K. Nielsch, R. B. Wehrspohn, J. Barthel, J. Kirschner, U. Gosele, S. F. Fischer, H. Kronmuller, Appl. Phys. Lett., Vol. 79, No. 9 (2001) 1360 – 1362
- [1.36]. K. Pirota, D. Navas, M. Hernandez-Velez, K. Nielsch, M. Vazquez, Journal of Alloys and Compounds, 369 (2004) 18 – 26

- [1.37]. N. B. Chaure, P. Stamenov, F. M. F. Rhen, J. M. D. Coey, *Journal of Magnetism and Magnetic Materials*, 290 – 291 (2005) 1210 – 1213
- [1.38]. P. Yang, M. An, C. Su, F. Wang, *Electrochimica Acta*, 54 (2008) 763 – 767
- [1.39]. W. B. Choi, J. U. Chu, K. S. Jeong, E. J. Bae, J. W. Lee, J. J. Kim, J. O. Lee, *Appl. Phys. Lett.* 79, No. 22 (2001) 3696
- [1.40]. S. –L. Oh, Y. –R. Kim, L. Malkinski, A. Vovk, S. L. Whittenburg, E. –M. Kim, J. –S. Jung, *Journal of Magnetism and Magnetic Materials*, 310 (2007) e827 – e829
- [1.41]. A. Huczko, *Appl. Phys. A*, 70 (2000) 365 – 376
- [1.42]. O. Azzaroni, M. Fonticelli, P. L. Schilardi, G. Benitez, I. Caretti, J. M. Albella, R. Gago. L. Vazquez, R. C. Salvarezza, *Nanotechnology*, 15 (2004) S197 – S200
- [1.43]. T. N. Narayanan, M. M. Shaijumon, P. M. Ajayan, M. R. Anantharaman, J. *Phys. Chem., C* 112 (2008) 14281 – 14285
- [1.44]. V. Venkatasamy, N. Jayaragu, S. M. Cox, C. Thambidurai, M. Mathe, J. L. Stickney, *Journal of Electrochemical Chemistry*, 589 (2006) 195 – 202
- [1.45]. G. Binning, Ch. Gerber, E. Stroll, T. R. Albrecht, C. F. Quate, *Europhys. Lett.*, Vol. 3, No.12 (1987) 1281 – 1286
- [1.46]. G. Binning, C. F. Quate, Ch. Geber, *Phys. Rev. Lett.*, 56 (1986) 930 – 933
- [1.47]. A. Engel, D. J. Muller, *Nature Structural Biology*, Vol. 7, No. 9 (2000) 715 – 718
- [1.48]. A. Knoll, R. Magerle, G. Krausch, *Macromolecules*, 34 (2000) 4159 – 4165

[1.49]. S. C. Minne, H. T. Soh, Ph. Flueckiger, C. F. Quate, Appl. Phys. Lett.
Vo.66, No. 6 (1995) 703 – 705

[1.50]. M. R. Koblischka, U. Hartmann, T. Sulzbach, Thin Films, 428 (2003) 93 –
97

[1.51]. P. B. Fischer, M. S. Wei, S. Y. Chou, J. Vac. Sci. Technol., B 11 (1993)
2570 – 2573



CHAPTER TWO: THEORETICAL BACKGROUND

2.1. MAGNETISM

2.1.1. Introduction

Even though magnetism is one of the oldest subjects of solid state physics, nanomagnetism research receives more attention and lots of problems still pose challenges [2.1]. Size reduction of objects to atomic size affects the properties of the objects, for example, the size of the magnetic domain is about 1 μm and magnetic particles smaller than this will be a mono-domain [2.2]. The term “nano” in nanomagnetism is not uniquely defined, i.e. the bulk magnetic material constitutes small scale sized magnetic domains. In simple terms all magnetic systems can be considered nanostructured.

Even though much work have already been done on small metals with their well known electronic and geometrical structures, the field is still expanding due to huge number of systems and the complexities of magnetic materials. Small magnetic particles are of industrial significance in the fabrication of magnetic media. Magnetic materials are further used as sensors, i.e. in giant magnetoresistance used as heads to read magnetically stored data. The sections that follow will cover the basic concepts of magnetism. The origin and classification of magnetic properties will also be briefly discussed.

2.1.2. Origin of magnetism

All matter is composed of atoms which are made up of electrons and a nucleus at its centre. The constituents of the nucleus are the protons and the neutrons. The electrons orbit around the nucleus with a constant motion. Electrons are negatively charged and they produce a magnetic field as they move through space. The magnetic field induced by the rotating electrons originates from the magnetic moment which is a fundamental object of magnetism and it has the unit ampere meter squared (Am^2). The magnetic moment of a free atom originate from three principal sources [2.3] (figure 2.1).

- The spin with which electrons are endowed,
- The orbital angular momentum about the nucleus,
- and the change in the orbital momentum induced by the applied magnetic field.

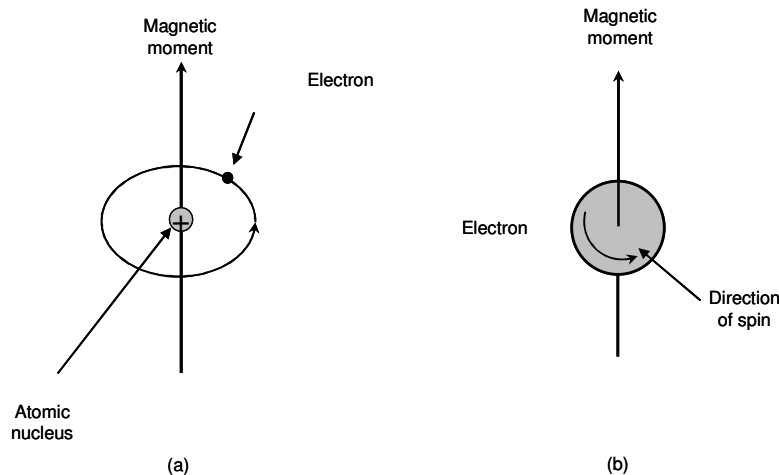


Figure 2. 1: Demonstration of the magnetic moment associated with (a) an orbiting electron and (b) spinning electron.

The first two sources give paramagnetic contributions to magnetization and the third gives a diamagnetic contribution. Spin magnetic moment can either be spin up or spin down. According to Pauli Principle two electrons with opposite spins can be accommodated in a given orbital. In completely filled shells, electrons spin cancel each other and there will be no net magnetic moment while in incomplete shells, unpaired electrons spin will not cancel and there will be a net magnetic moment. Magnetic properties of solids are grouped in three classes:

- Diamagnetism,
- Paramagnetism,
- Ferromagnetism, antiferromagnetism and ferrimagnetism.



A material in the presence of an external magnetic field H acquires a magnetization σ , which is a magnetic moment per unit volume. The magnetization is characterized by the magnetic susceptibility χ defined as:

$$\sigma = \chi H \quad (1)$$

χ measures the ease with which a material acquires a magnetization in the presence of an applied field.

In the present study, we will confine our discussion on diamagnetism, paramagnetism, ferromagnetism, ferromagnetic domains, antiferromagnetism and anisotropy energy.

2.1.2.1. Diamagnetism

Diamagnetism is associated with the tendency of electrical charges partially to shield the interior of a material from an applied magnetic field. In Diamagnetism, materials have very weak and negative susceptibility ($\chi < 0$) from applied magnetic field with a magnitude of the order of 10^{-5} [2.4]. Diamagnetic materials are slightly repelled by a magnetic field and do not retain the magnetic properties when the field is removed. Diamagnetism properties result from Lenz's law which states that if the magnetic flux enclosed by a current loop is changed by the application of a magnetic field, the induced current will oppose the original current and give rise to the magnetic moments that opposes the applied magnetic field. Figure 2.2 illustrates how the dipole moments oppose the applied field when an electron which was orbiting around the nucleus is considered as a little current loop.

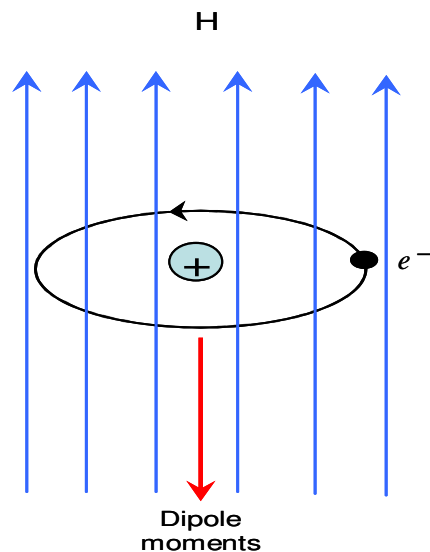


Figure 2. 2: The atomic dipole configuration for a diamagnetic material which opposes the applied magnetic field.

Diamagnetism is found in all elements and is usually is very weak to be detected and can be neglected for electrons in the shell which are associated with permanent magnetic moments.

2.1.2.2. Paramagnetism

In Paramagnetism, materials have a small and positive susceptibility from applied magnetic fields with magnitudes of the order 10^{-3} to 10^{-5} [2.4]. Paramagnetism is associated with the outermost electrons which are tightly bound to the atom contrary to inner electrons which causes diamagnetism. Paramagnetic materials in the presence of an external magnetic field, the magnetic moments are aligned parallel to the direction of the field as illustrated in figure 2.3. When the external field is removed, the moments return to their random orientations. Paramagnetic properties are due to the presence of some unpaired electrons and from the realignment of the moments caused by external fields.

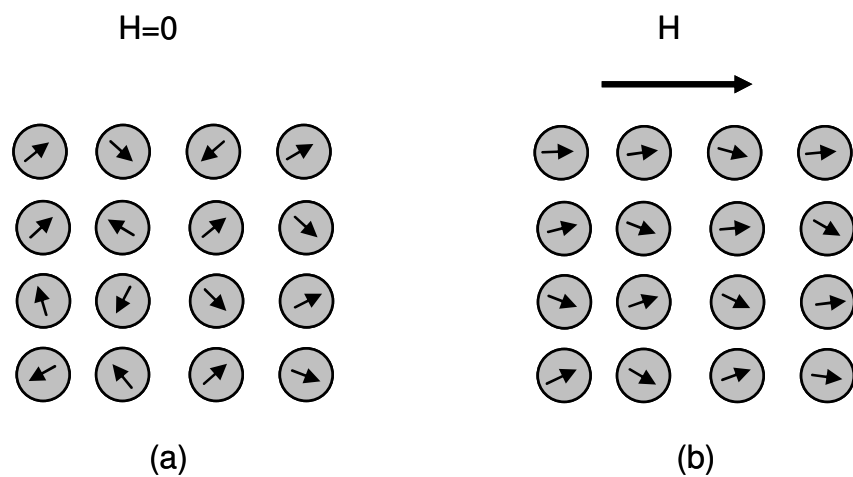


Figure 2. 3: The atomic dipole configuration for a (a) paramagnetic material without and (b) with external magnetic field.

The effect of paramagnetism is found in compounds of transition, rare-earth elements and actinides with partially filled 3d, 4f and 5f electron shells respectively. Atoms with an odd number of electrons will have a net magnetic moment resulting from the total angular momentum electrons according to quantum mechanics.

2.1.2.3. Ferromagnetism

The origin of ferromagnetism in metals was first interpreted by Heisenberg as a result of the fact that all magnetic moments of the atoms are aligned with some orientation throughout the crystal by the effect of the exchange interaction between the incomplete inner shells of two adjacent atoms. Ferromagnetic materials have large and positive susceptibility ($\chi > 0$) in the presence of the applied external magnetic field. Magnetization also exists in the ferromagnetic material in the absence of the applied magnetic field. The existence of spontaneous magnetic moments in zero applied magnetic fields suggests that the electron spins and magnetic moments are arranged in a regular pattern. (See figure 2.4)

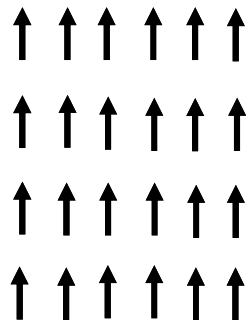


Figure 2. 4: The atomic dipole for a ferromagnetic material which exists in the absence of an applied external field and in the presence of the external field.

In a ferromagnetic material, the Curie point (T_c) is the temperature above which the moments are randomly oriented and the material loses its magnetic moments. This region is known as the paramagnetic phase. Below T_c , the magnetic moments are aligned parallel to each other and the materials possess spontaneous magnetic moments. This region is known as an ordered ferromagnetic phase, e.g. $T_c = 1043\text{K}$ for iron [2.3]. In the ordered phase, different regions within the iron are magnetized in different directions (figure 2.5), such that net magnetization is zero. A particular region within which the magnetization is different from zero (spontaneous magnetization) is called a domain. Well known examples of ferromagnets are the transition and rare-earth metals such as Fe, Co, Ni and Gd.

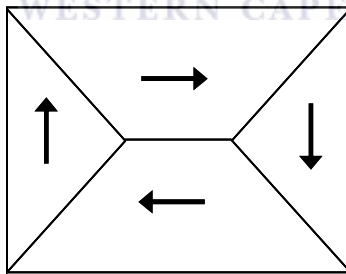


Figure 2. 5: Schematic of a ferromagnet showing four domains with zero net magnetization.

2.1.2.4. Ferromagnetic Domains

Domains are small regions in a specimen within which each local magnetization is saturated, illustrated by figure 2.6. They have a transition layer

that separates adjacent regions magnetized in different directions called Bloch walls (see figure 2.7). The spin direction between the domains is continuous across a single plane and it slowly occurs over many atomic planes. The direction of magnetization for different domains should not be parallel.

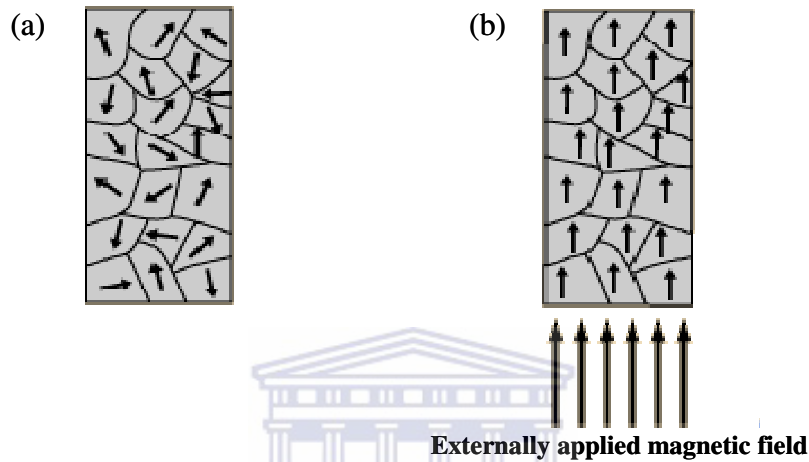


Figure 2. 6: (a) illustrates the magnetic domains with randomly oriented spins and (b) magnetic domains with spins aligned in the direction of an externally applied magnetic field.

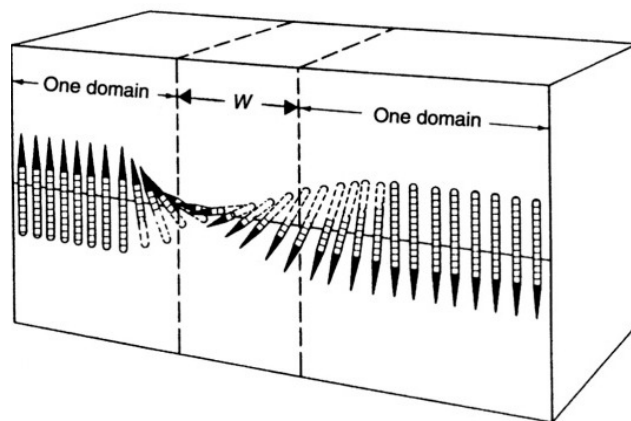


Figure 2. 7: Schematic representation of the change in movement orientation within a 180° Bloch wall [2.5].

The thickness of a Bloch wall depends on the anisotropy energy and on the exchange coupling constant J . When an external magnetic field is applied to a ferromagnetic specimen, the increase in the gross magnetic moment takes place by two independent processes: (i) when a weak field is applied, the volume of domains favourably orientated with respect to the field increases at the expense of unfavourably orientated domains, and (ii) when the strong field is applied the domain magnetization rotates towards the direction of the field. Figure 2.8 illustrates these two processes.

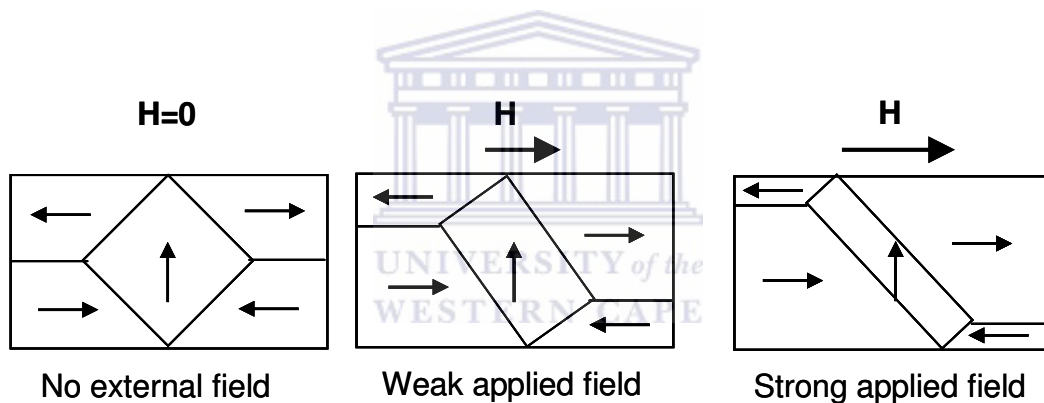


Figure 2. 8: A schematic showing how ferromagnetic domains respond to the external magnetic field.

2.1.2.5. Antiferromagnetism

An antiferromagnetic material is formed by two magnetized sublattices whose orientations are opposite to each other. This arrangement leads to no spontaneous magnetization (see figure 2.9). However the internal structure of these materials is similar to that of the ferromagnet.

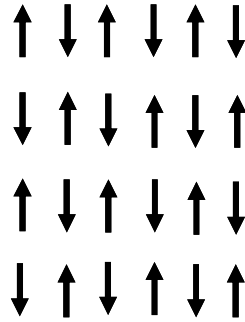
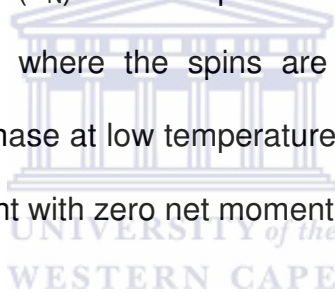


Figure 2. 9: The atomic dipole configuration for an antiferromagnetic magnetic material showing a zero net magnetic moment.

Antiferromagnetic materials are characterized by a critical temperature called the Neel Temperature (T_N). This temperature separates the paramagnetic phase at high temperature where the spins are randomly oriented and the ordered antiferromagnetic phase at low temperature where the spins are ordered in an antiparallel arrangement with zero net moment.



2.1.2.6. Anisotropy Energy

Anisotropy energy in a ferromagnetic crystal is the energy required to direct the magnetization along certain crystallographic axes. This energy, originates from the spin-orbit interactions. However, small magnetic particles usually form monodomains. So the orientations of their magnetic moments are determined by the crystal shape and structure through the anisotropic effects. Shape anisotropy is responsible for the preferential orientation of magnetization. Magnetization prefers the alignment along easy axes of magnetization.

2.1.3. The Theory of Magnetic Force Microscopy

Ferromagnetic domains can be imaged by magnetic force microscopy (MFM) which uses a sharp tip coated with a thin film of ferromagnetic material. It measures the forces that act between the local magnetized tip and the samples. These forces can be derived from sample-tip interaction energy of either a tip magnetization in the stray field of the sample or the sample magnetization in the stray field of the tip [2.6].

The interaction energy (E_{inter}) can be written as:

$$E_{inter} = - \int_{tip} \mathbf{J}_{tip} \cdot \mathbf{H}_{sample} dV = - \int_{sample} \mathbf{J}_{sample} \cdot \mathbf{H}_{tip} dV \quad (2)$$

where \mathbf{J}_{tip} is the magnetization of the tip, \mathbf{H}_{sample} the stray field of the sample, \mathbf{J}_{sample} the magnetization of the sample and \mathbf{H}_{tip} the stray field of the tip. The first integral supports the interpretation of magnetic force microscopy. The magnetized tip interacts with the stray of field of the sample. The interaction energy including the derived force or gradient force gives information about the stray field. Patterns with different magnetization with identical stray field cannot be distinguished. The second integral shows that the tips with different internal magnetization distribution are equivalent. To get more insight from the interaction integral in equation (2), they were transformed by partial integration:

$$E_{inter} = - \int_{surface} \lambda_{sample} \cdot \Phi_{tip} dV - \int_{surface} \sigma_{sample} \cdot \Phi_{sample} dS \quad (3)$$

with

$$\lambda_{\text{sample}} = -\text{div}\mathbf{J}_{\text{sample}} \quad \text{and} \quad \sigma_{\text{sample}} = \mathbf{n}\cdot\mathbf{J}_{\text{sample}} \quad (4)$$

where λ_{sample} is the volume charge and σ_{sample} is the surface charge of the sample, while Φ_{tip} is the scalar potential of the tip stray field obeying the expression in equation (5):

$$\mathbf{H}_{\text{tip}} = -\text{grad}\Phi_{\text{tip}} \quad (5)$$

To get the force, the interaction energy, Φ_{tip} , is replaced by $\frac{d\Phi_{\text{tip}}}{dz}$ and for a microscope operated in the force gradient, the second derivative, $\frac{d^2\Phi_{\text{tip}}}{dz^2}$, has to be inserted in equation (3). MFM maps the polar magnetization component to image narrow domains of perpendicular recording medium as black and white lines depending on their polarity.

2.2. ELECTROCHEMICAL CELL

Electrochemical cell is a method used to generate voltage and current from chemical reactions [2.7]. It is made up of two half-cells in which each half-cell consist of an electrode, an anode where oxidation occurs and cathode where reduction occurs (see figure 2.10). The two electrodes are both immersed in the electrolyte. This electrolyte serves as a conduction medium which provides the flow of ions to and from the electrodes where redox reactions take place.

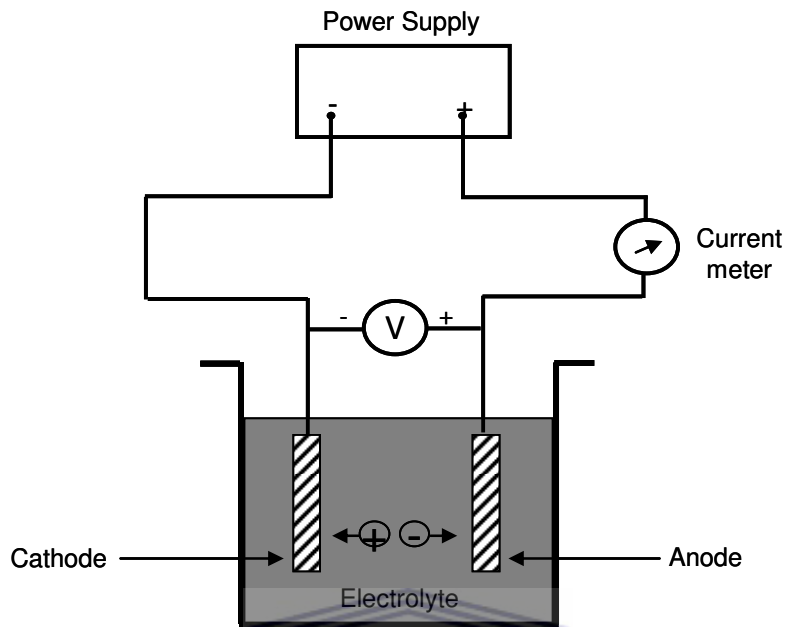


Figure 2. 10: Schematic diagram of the electrochemical cell set – up.

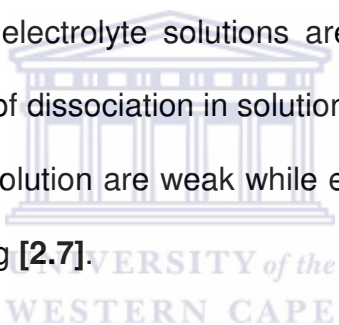
In the presence of electric field, E , ions in an electrolyte solution will experience the electric driving force (f_{dr}) which will cause the ions to migrate in the direction given by the field. The electric driving force is represented as follows:

$$f_{dr} = z_j F E \quad (6)$$

where $z_j F$ is the charge with j ions and E is the electric field. Ionic movements lead to the transport of charge. The charge species flow from one electrode to another; as a result there is an electric current in the electrolyte [2.8]. In sections 2.2.1 and 2.2.2, the functions of the electrolyte and the electrode in the electrochemical cell are discussed further.

2.2.1. Electrolytes

An electrolyte can be referred to a passage of an electric current that promote charge transfer which makes it work like an electrically conduction medium. The charge is carried by the movement of ions. Normally, an electrolyte is prepared by dissolving a salt in a solvent such as water to dissolve the molecules which dissociate into ions. These ions are in a continuous chaotic kinetic molecular motion. The number of dissolved ions is proportional to the amount of the current that can be carried by an electrolyte [2.9], and the electrolyte should be sufficiently conductive for it to be used in electrochemical reactions. Commonly used electrolyte solutions are acids, bases or salts and they have different degrees of dissociation in solutions. Thus electrolytes with low degree of dissociation in a solution are weak while electrolytes which completely dissociate in water are strong [2.7].



2.2.2. Electrodes

Electrodes are materials employed to pass an electric current through them, thus the anode and the cathode. The electrodes are both immersed in the electrolyte and connected to the power supply, i.e. anode is connected to the positive terminal while the cathode connected to the negative terminal. When the electric field is applied across them, the charge is transported through them by the movement of electrons. The electrode potential is described by Nernst equation:

$$E = E_0 - \left(\frac{RT}{nF}\right)\ln Q \quad (7)$$

where E_0 is the standard electrode potential, Q is the ions unity, F is the Faraday constant, R is the gas constant and T is the temperature. When the negative electrode potential is more than the energy level of the vacant molecular orbital in the electrolyte solution, electrons will be transferred from the electrode to the solution. This is a cathodic reaction which takes place on the cathode. For more positive electrode potential than the energy level of the occupied molecular orbital, electrons will be transferred from the electrolyte to the electrode. This is an anodic reaction which takes place in anode. Once the equilibrium is reached, the reaction will stop.

The electrodes that are commonly used are: 1) solids – Pt and Au, 2) liquids metals – Hg and amalgams, 3) Carbon – graphite and 4) semiconductors – indium-tin oxide and silicon. Pt electrode will be suitable to our study because it does not oxidize at any temperature and is insoluble in acids such as hydrochloric and nitric acid.

Firstly, we will consider the anodic reaction in which we anodize an aluminium foil in an acid medium. The section will cover the parameters that govern the reactions and how to optimize them. Secondly, we will discuss the cathodic reaction when we cover the subject on electrodeposition.

2.3. ALUMINIUM ANODIZATION

Aluminium anodization is the electrochemical oxidation of aluminium surface to form a stable oxide film or porous alumina films. This process is carried out in acidic medium. The commonly used acids are: oxalic acid, sulphuric acid, phosphoric acid and chromic acid [2.10]. Aluminium foil is attached to the anode (working electrode) while platinum mesh (counter electrode) attached to the cathode (see figure 2.10). This process is governed by anodizing parameters [2.11, 2.12]. Once optimized, anodizing parameters produce porous alumina that has a honeycomb structure with close-packed arrays of columnar cells (see figure 2.11).

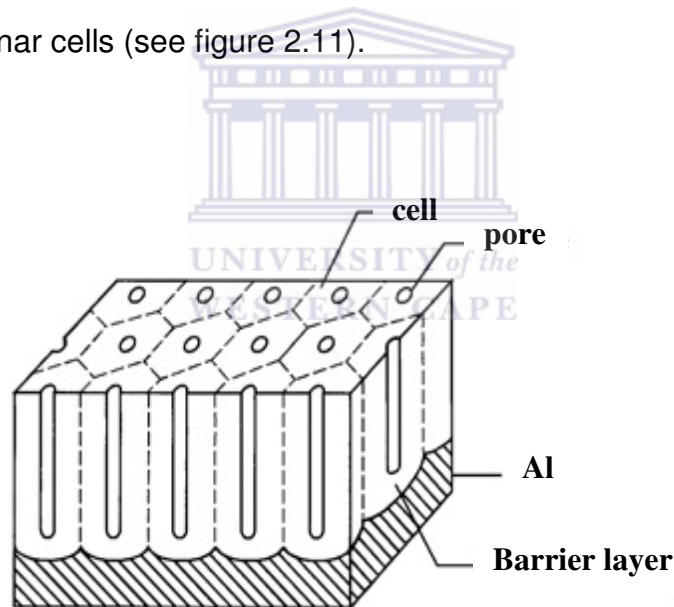


Figure 2. 11: Schematic structure of anodic alumina [2.13]

These columnar cells are perpendicular to the surface. The cell size is determined by the applied voltage [2.13] while the size of pores is governed by the electrolyte composition, temperature, and the anodizing period.

In the presence of electric field, oxidation occurs on the entire metal/oxide interface by the migration of oxygen containing ions (i.e. O^{2-} or OH^-) from the electrolyte. The ions O^{2-} will react with Al^{3+} ions to form Al_2O_3 :



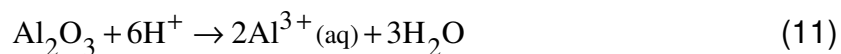
On the other hand, Al^{3+} ions migrate towards oxide/electrolyte interface and distribute in the oxide layer near the oxide/metal interface. Pores are formed as Al^{3+} drifts through the oxide layer while some of Al^{3+} gets into the electrolyte contributing in the formation of oxide. The half-reaction of processes is represented by equation (9):



At the same time, another process that also takes place is the electrolysis of water which occurs at the pore bottom near the electrolyte/oxide interface. Its half-reaction is represented by equation (10):



Finally, an electric-field enhanced oxide dissolution that happens at the electrolyte/oxide interface is described by equation (11):



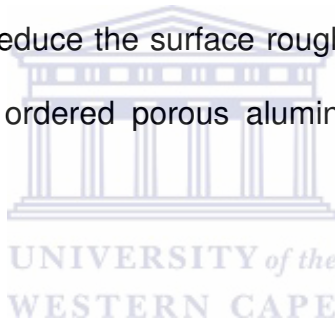
During the anodization processes O^{2-} will migrate within the alumina film, as a result $\text{Al}/\text{Al}_2\text{O}_3$ interface will be formed (equation 8) and on the other hand Al^{3+} will migrate outward in the film forming $\text{Al}_2\text{O}_3/\text{electrolyte}$ interface (equation 9). As Al^{3+} drifts through the oxide layer, pores that are perpendicular to the surface will be formed. Consequently, there will be repulsive forces between the neighbouring pores at the metal/oxide interface that promote the formation of hexagonal pore distributions. The volume expansion accompanying the aluminium oxidation gives rise to the mechanical stress at the interface between alumina and aluminium [2.14]. The expansion depends on the experimental conditions, viz; an increase in anodizing time will increase the expansion.

To synthesize the desired AAO template with hexagonal pore distribution, various parameters need to be optimized. These parameters are equally important and each needs to be optimized to produce the desired pore diameters, pore depths and interpore distances. These parameters includes: type of electrolyte, concentration, voltage, temperature and time [2.12]. The effects of these parameters on pore formation during anodization are discussed in the next section.

2.4. ANODIZATION PARAMETERS

2.4.1. Pre – treatment of Aluminium foil

Aluminium substrate should be annealed below its melting point to obtain large single crystal grains, i.e. the larger the grains are, the larger are the regions of self – ordered porous aluminium [2.15]. The temperature at which the foil is annealed does affect pore formation. Yu et al. [2.16] anodized aluminium foil which was annealed at 200 °C, 400 °C and 600 °C, they found that foil annealed at 600 °C is suitable to prepare large scale ordered AAO nanopores. Electropolishing is used to reduce the surface roughness and is the prerequisite for the formation of self – ordered porous alumina with a large domain size [2.17].



2.4.2. Anodization voltage

Research conducted on the subject shows that there is a linear relationship between the interpore distances and anodizing voltage [2.18], as well as the cell size and voltage [2.19]. Lower anodization voltage shows that there is lack of uniformity in the interpore distances and pore diameter [2.20]. For higher voltages, evidently, pore arrangement is disordered due to the increase of the volume expansion and cracks [2.10]. The anodizing voltage also depends on the type of the electrolyte used. Electrolytes have their own restrictions due to the conductivity and the pH. The optimal potentials for sulphuric acid ranges from 5 – 40 V, oxalic acid ranges from 30 – 120 V and phosphoric acid ranges from 80 –

200 V. The voltage range provides the minimum and maximum voltage values which are more favourable for pore formation of each electrolyte.

2.4.3. Anodizing time

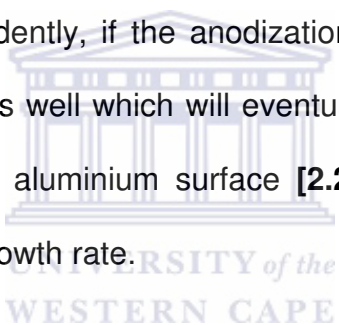
The influence of the anodizing time pore formation depends on other anodizing parameters. Pancholi *et al.* [2.21] when using an optimum voltage of 40 V found that long-time anodization improved the ordering of the pore arrays. Long-time anodization also rearranges the cell and minimizes defects dislocations [2.14]. Longer anodization time under appropriate constant voltage may cause defects at the boundaries of the domains [2.19].

2.4.4. Type of electrolyte and the concentration

The type of the electrolyte should be properly selected in order to obtain the desired pore diameters. To produce large pore diameters phosphoric acid must be use, for medium – sized pore diameters oxalic acid must be used and to produce small pore diameters sulphuric acid must be used [2.22]. These restrictions are due to the conductivity and the pH of the electrolytes. An increase in acid concentration shows a little increase in pore diameters [2.18] and reduced barrier thickness. It should be noted that an increase in acid concentration means an increase in acid conductivity. Increasing the concentration of the electrolyte shifts the optimal condition of the temperature [2.23]. Continuous stirring of the electrolyte removes hydrogen bubbles, local heat on the surface and to allow uniform diffusion of anions into pore channels.

2.4.5. Temperature

Ordered pore formation depends on the anodization temperature employed even though it has less influence on the pore ordered domain size than acid concentration [2.24]. Low temperatures prevent the oxide layer from being dissolved in acidic electrolytes and also help to avoid local heating at the bottom of the pore [2.25]. The local heating causes an inhomogeneous distribution of the electric field. The oxide layer may crack or burst if the temperature is not controlled. Lower anodization temperatures show that there is higher symmetry on pore distribution and that the symmetry continuously decreases with increasing temperature. Evidently, if the anodization temperature is higher, the reaction rate will be faster as well which will eventually lead to more disorder of pore distribution across the aluminium surface [2.26]. Lowering the anodizing temperature will lower the growth rate.



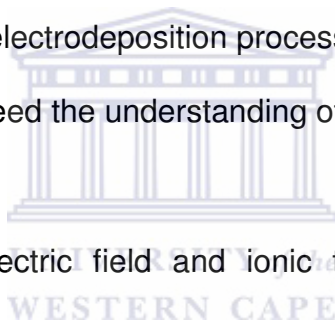
2.5. ELECTRODEPOSITION

Electrodeposition is the technique that uses electrical current to reduce cations of a desired material from a solution and deposit on conductive object (electrode). In a simple form, electrodeposition or electroplating consists of an electrolyte containing metal ions (e.g. CoSO_4), working electrode and a counter electrode. As a tool of materials technology, electrodeposition has attracted attention and is a method used to obtain films with wide range of materials including semiconductors, high- T_c superconductors, polymer films, etc [2.27]. Among other applications, electrodeposition has been used to prepare metallic

mirrors and corrosion-resistant surfaces. These applications were fueled by some of the advantages of this technique which include:

- The possibility of growing uniform films over large area and regular shaped surfaces as well,
- Non-equilibrium alloys can be electrodeposited,
- Different industrial understanding can be drawn up,
- Low cost, high throughput and availability.

Despite these advantages, electrodeposition process covers the physical and the chemical phenomena that need the understanding of the following aspects:



- The influence of electric field and ionic transport of the discharged process,
- The thermodynamic and kinetic factors related to the electrodeposition process,
- Factors governing the composition, structure and morphology,
- The function of additives during electrodeposition.

All these factors need to be optimized to produce the desired results.

Consider the electrodeposition system that consists of an electrolyte containing metal ions, an electrode on which deposition will take place, reference electrode and a counter electrode. The current in the electrolyte is brought by the

cations when they move towards the cathode while anions move towards the anode. Using the electrolyte that contains **A** metal ions as an example, electrodeposition can be outlined as follows:

When the electric field is applied, A^{2+} will move to the cathode and the elemental deposition can be written as



The **A** metal ions will be reduced to form **A** (solid) on the working electrode. As electrodeposition proceeds, the ionic concentration in the bath is reduced and need to be replaced by adding the cobalt salts. The electroplated **A** depends directly on the current existing at the particular region of the substrate. Uniform current distribution produces uniform film while poor electrolyte conductivity produces non-uniform deposition. Using highly conductive electrolyte may offset some of the edges effect because ions can swiftly move across the surface.

The electrodeposition discussed above (with the aid of figure 2.12) can be summarized in the following successive steps:

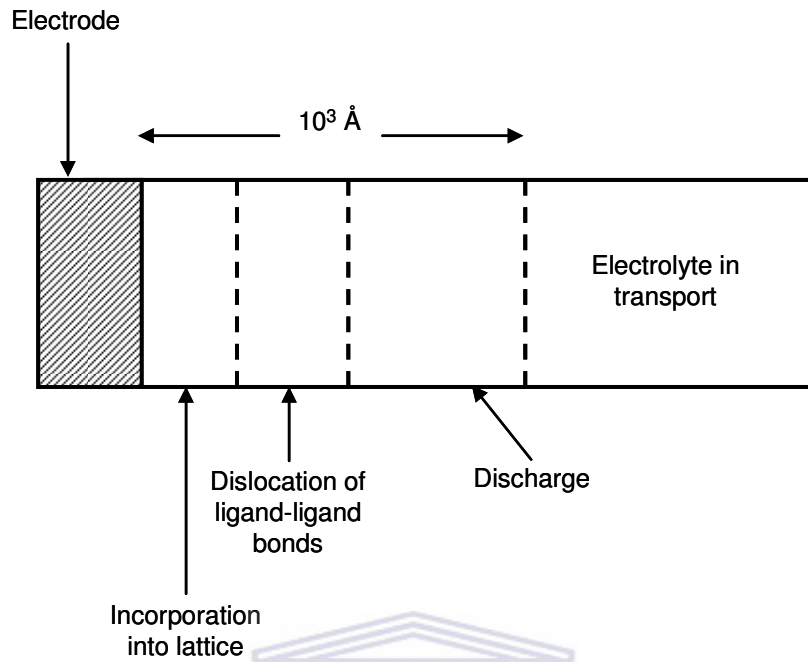
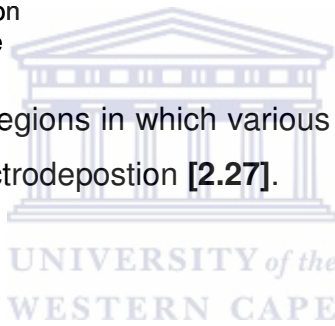


Figure 2. 12: Approximate regions in which various steps of ion transport occurs leading to electrodeposition [2.27].



- (1) Ionic transport,
- (2) Discharge,
- (3) Breaking up of ion-ligand bond,
- (4) Incorporation of adatoms onto the substrate followed by nucleation and growth.

REFERENCES

- [2.1]. D. L. Mills, J. A. C. Bland, Nanomagnetism - Ultrathin Films, Multilayers and Nanostructures, Elsevier B. V, 2006
- [2.2]. Z. L. Wang, Characterization of Nanophase Materials, Wiley-VCH GmbH, 2000
- [2.3]. C. Kittel, Introduction to Solid State Physics, Eighth Edition, New York: J. Wiley, 2005
- [2.4]. M. N. Rudden, J. Wilson, Elements of Solid State Physics, John Wiley & Sons Ltd, 1980
- [2.5]. K. H. J Buschow, F. R. De Boer, Physics of Magnetism and Magnetic Materials, Kluwers Academic Publishers, 2003
- [2.6]. A. Hubert, R. Schafer, Magnetic Domains, The Analysis of Magnetic Microstructures, Springer-Verlag Berlin Heidelberg, 1998
- [2.7]. V.S Bagosky, Fundamentals of Electrochemistry, second edition, John Wiley & Sons, Inc., 2006
- [2.8]. C. H. Hamann, A. Hammett, W. Vielstich, Electrochemistry, first edition, Wiley-VCH Verlag GmbH, 1998
- [2.9]. S. Glasstone, An Introduction to Electrochemistry, Sixth Printing, Toronto: Van Nostrand, 1942
- [2.10]. A. P. Li, F. Muller, A. Birner, K. Nielsch and U. Gosele, J. Appl. Phys, Vol. 84, No. 11 (1998) 6023 – 6026
- [2.11]. Y. F. Mei, X. L. Wu, T. Qui, X. F. Shao, G. G. Siu, P. K. Chu, Thin Solid Films, 492 (2005) 66 – 70

- [2.12]. A. Bai, C. Hu, Y. Yang, C. Lin, *Electrochim. Acta* (2007), doi:
10.1016/j.electacta.2007.09.039
- [2.13]. R. B. Wehrspohn, *Ordered Porous Nanostructures and its Applications*,
Springer Science + Business Media, Inc. New York, 2005
- [2.14]. H. Chik, J. M. Xu, *Materials Science and Engineering*, R 43 (2004) 103 –
138
- [2.15]. A. Cai, H. Zhang, H. Hua and Z. Zhang, *Institute of Physics Publishing*,
Nanotechnology, 13 (2002) 627 – 630
- [2.16]. W. H. Yu, G. T. Fei, X. M. Chen, F. H. Xue, X. J. Xu, *Phys. Lett. A* (2006)
292 – 395
- [2.17]. D. Crouse and Y. Lo, *Applied Physics letters*, Vol. 76, No.1 (2000) 49 – 51
- [2.18]. J. P. O’Sullivan and G. C. Wood, *Proc. Roy. Soc. Lond, A*, (1970) 511 –
543
- [2.19]. H. Masuda and K. Fakuda, *Science*, Vol. 268, (1995) 1466 – 1468
- [2.20]. G. D. Sulka, K. G. Parkola, *Thin Solid Films*, 515 (2006) 338 - 345
- [2.21]. A. Pancholi, V. G. Stoleru, C. D. Kell, *Nanotechnology*, 18 (2007) 215607
(8pp)
- [2.22]. Y. Lei, W. Cai, G. Wilde, *Progress in materials science*, 52 (2007) 465 –
539
- [2.23]. M. A. Kashi and A. Ramazani, *J. Phys. D: Appl. Phys.*, 38 (2005) 2396 –
2399
- [2.24]. L. Ba and W. S. Sang, *J.Phys. D: Appl. Phys.*, 33 (2000) 2527 – 2531

- [2.25]. J. Choi, Fabrication Of Monodomain Porous Alumina Using Nanoimprint Lithography, Dr. -Ing. Dissertation, Martin-Luther-Universitat Halle-Wittenberg, 05/02/2004
- [2.26]. O. Jessensky, F. Muller and U. Gosele, Appl. Phys. Lett. Vol. 72, No. 10 (1998) 1173 – 1175
- [2.27]. R. K. Pandey, S. N. Sahu, S. Chandra, Hamdbook Of Semiconductor Electrodeposition, Marcel Dekker, Inc, 1996

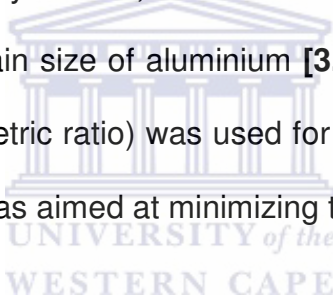


CHAPTER THREE: EXPERIMENTAL DETAILS

3.1. EXPERIMENTAL PROCEDURES

3.1.1. Pre – treatment of Aluminium

Prior to the formation of nanoporous aluminium oxide, 1 x 1 cm samples were cut from a 10 µm thick aluminium foil (99.99 % purity, Goodfellow) and rinsed with ethanol. The samples were then annealed at 400 °C for 4 h using an elite furnace manufactured by Lenton, which was aimed at reducing dislocation density and increase the grain size of aluminium [3.1]. The mixture of perchloric acid and ethanol (1:4 volumetric ratio) was used for electropolishing the samples at constant voltage, which was aimed at minimizing the surface irregularities.



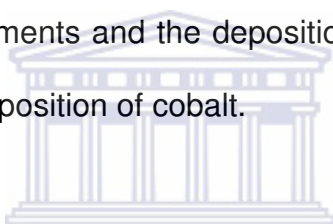
3.1.2. Aluminium Anodization

Electrochemical oxidation of aluminium was carried out with a two-electrode cell using the pre-treated aluminium foil. The first anodization step was carried out in 0.4 M of oxalic acid for 20 minutes with constant voltage supply of 40 V while the bath temperature was maintained at approximately 18 °C by the ice bath. To maintain uniform ionic distribution in a solution, the magnetic stirrer was used. After the first anodization step, the sample was then rinsed with methanol for a minute and chemically etched in the mixture of 1.8 wt% chromic acid and 6.0 wt% phosphoric acid for about 2 minutes. Second anodization step was carried out under the same conditions as the first. The experiment was

repeated while varying the anodizing voltages from 40 V to 50 V, the concentration from 0.4 M to 0.5 M, anodizing periods were varied between 20 minutes and 3 hours while the temperatures were lowered from approximately 18 °C to 8 °C. These set of anodizing parameters were tried and characterized to investigate how they influence the pore diameters, depths and interpore distances growth.

3.1.3. Electrodeposition on Anodized Alumina

Two types of electrochemical cells were used, electrochemical bath for cyclic voltammetry measurements and the deposition of manganese oxide while the flow-cell was used for deposition of cobalt.



3.1.3.1. Electrochemical Bath Deposition

A three-electrode cell was used to carry out cyclic voltammetric studies on AAO template as depicted in Figure 3.1. The cell incorporated (i) a custom-modified beaker containing the electrolyte and the AAO template used as working electrode (ii) a Ag/AgCl/3M KCl reference electrode (Model 6.0750.100, Metrohm, Switzerland), (iii) a custom-made platinum mesh as counter electrode, and (iv) an Autolab potentiostat PGSTAT30 , equipped with GPES 4.9.007 software (Eco Chemie BV, The Netherlands) [3.2].

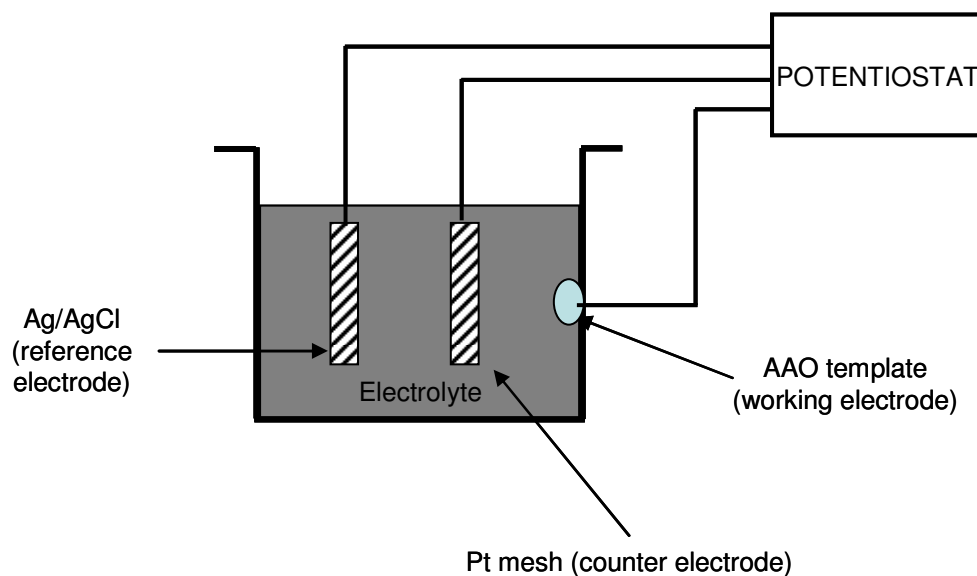
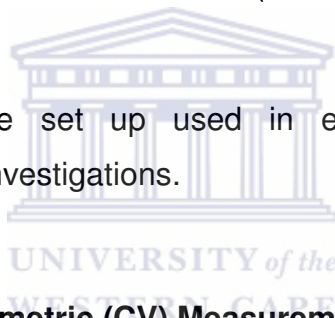


Figure 3. 1: Three-electrode set up used in electrodeposition and cyclic voltammetric investigations.



3.1.3.1.1. Cyclic Voltammetric (CV) Measurements

CV measurements were taken to investigate the chemical behavior of the cobalt solution prepared from a mixture of 0.12 M CoSO_4 + 0.49 M H_3BO_3 with pH 5. CV measurements were done on unanodized aluminium foil and on alumina which was coated at the back with Au-Pd film. Measurements were taken when the voltage ranges from +0.2 V to -1.3 V. For a 0.3 M of manganese (II) chloride tetrahydrate solution, cyclic voltammetry measurements were performed on unanodized aluminium foil and on alumina which was coated at the back with Au-Pd film. Measurements were done when the voltage ranges from +1.2 V to -0.5 V.

3.1.3.1.2. Procedure for Manganese Oxide Deposition

The electrodeposition of manganese oxide was done using 0.3 M of manganese (II) chloride tetrahydrate ($\text{MnCl}_2 \cdot 4\text{H}_2\text{O}$). Electrodeposition was carried out using Electrochemical Deposition technique and Pt mesh was used as a counter electrode, Ag/AgCl/3MKCl as a reference electrode and alumina (attached to Cu adhesive tape) as working electrode. The duration of electrodeposition was about 60 minutes. Finally, the samples were rinsed in de-ionized water and dried in air. This experiment was repeated while varying the deposition period.

3.1.3.2. Flow-cell Based Electrodeposition

The flow-cell used had a 120 μL flow-channel (defined by a 1 mm thick silicone rubber gasket), it consist of two Perspex blocks for holding (i) the reference and counter electrode (all in the upper block), (ii) working electrode **[3.3]** (see figure 3.2). The Ag/AgCl/3 M KCl reference electrode (model 6.0727.000, Metrohm) was placed at the outlet channel of the cell. The AAO template was attached using a Cu adhesive tape on a glassy carbon rod embedded on a brass holder that was secured via fine threading into the Perspex block.

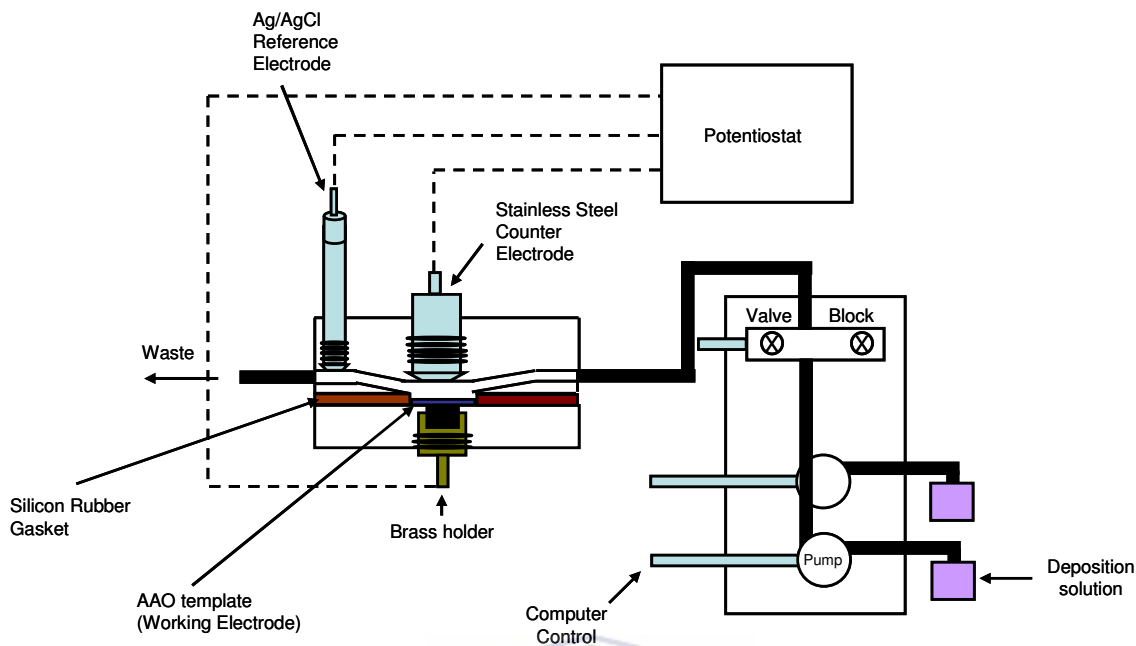
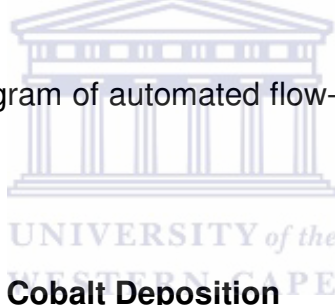


Figure 3. 2: Schematic diagram of automated flow-cell electrodeposition system [3.3].



3.1.3.2.1. Procedure for Cobalt Deposition

A dedicated computer program was used to electrodeposit Co nanostructures. General steps involved, (i) rinsing the flow-cell with 1 M H_3PO_4 , (ii) filled cell with CoSO_4 solution, (iii) applying -1.1 V, in stationary solution for various deposition times and (iv) rinsing the cell with H_3PO_4 . The deposit were rinsed with de-ionized water and dried in air.

3.2. EXPERIMENTAL TECHNIQUES

3.2.1. Atomic Force Microscopy (AFM)

Atomic Force Microscopy (AFM) is a versatile technique that uses a sharp tip to image both conducting and non-conducting samples providing atomic resolution, 3-D images of sample surfaces in ambient, vacuum and liquid environments. This technique was developed by Binning *et al.* (1985) [3.4] to measure ultra small forces present between the tip surface and a sample surface. This development was based on the scanning tunnelling microscope (STM) design which was only used to study surfaces of electrically conductive materials to some degree [3.5]. There are two configurations of AFM, one in which the sample scans the tip and the one in which the tip scans the sample. Tips are mounted at the far end of the cantilever that scans the sample surfaces while the deflection of the cantilever is monitored by the laser beam, see figure 3.3. The reflected laser beam will be detected by the photo-detector and sent to the feedback loop which in turn converts the signal to form a topographic image showing sample features. Commonly used cantilevers are Si_3N_4 that have approximately 200 μm length and the spring constant of 0.06 N/m or 0.12 N/m. Other materials such as carbon nanotubes and tungsten are used as well.

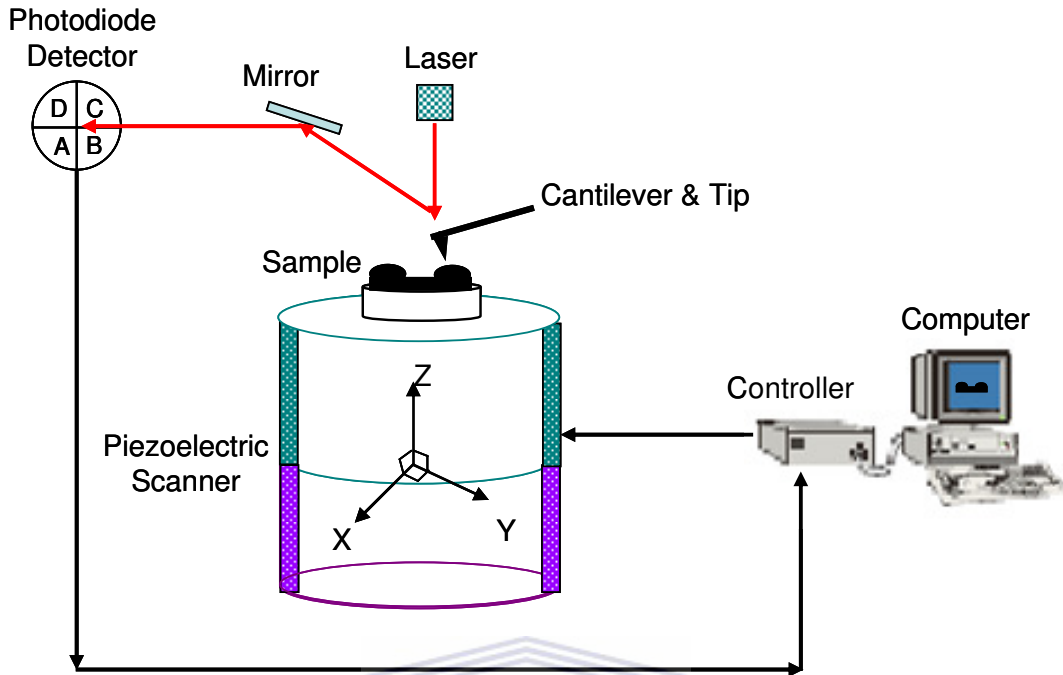


Figure 3. 3: Schematic diagram of atomic force microscope [3.6].

The AFM uses a piezoelectric scanner which the movement depends on the applied voltage across its electrodes; usually it translates in three directions (*x, y and z*) as illustrated in figure 3.3.

The atomic force microscope can either be used in static or dynamic mode. In static mode a tip is brought into close contact with the sample surface throughout the scan and is sometimes referred to as repulsive mode or contact mode. Dynamic mode consists of two types of modes which are: (I) Non-contact mode in which the cantilever is oscillated above the sample and the tip does not touch the sample surface during the scan and (II) Intermittent mode which is sometimes referred to as attractive force mode or tapping mode where the tip

oscillates above the sample surface and taps the sample during the scan. Using figure 3.4, these mode are further discussed in the next sections.

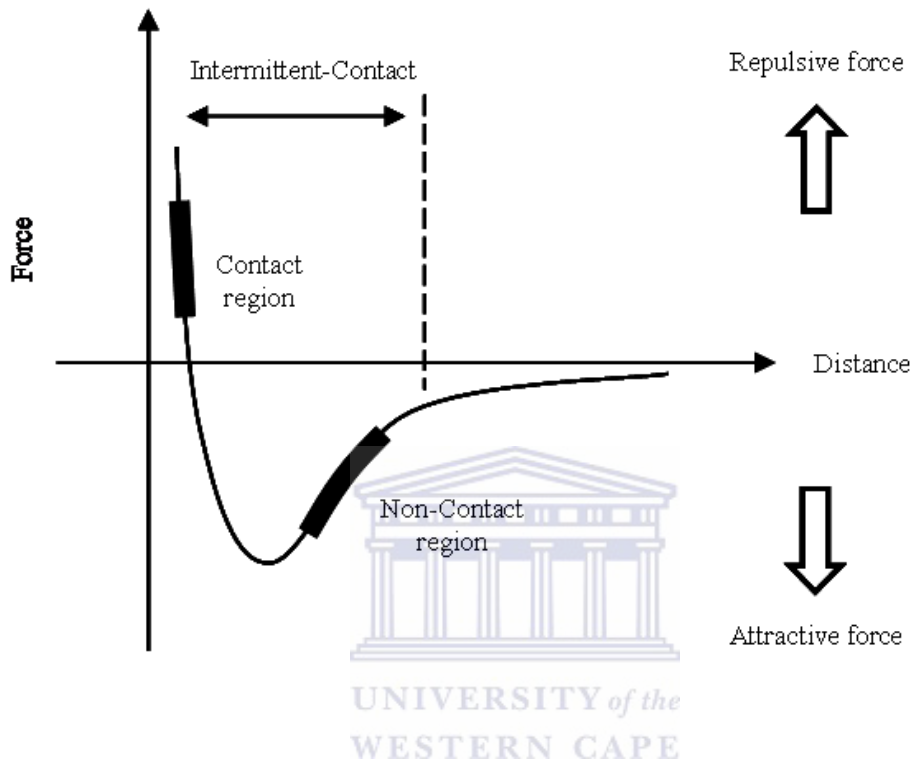


Figure 3. 4: Inter-atomic force as function of distance graph.

3.2.1.1. Static Mode

In contact mode, the tip is brought in contact with the sample surface throughout the scan. “Contact” means that in the repulsive regime of the inter-molecular force curve, as shown in figure 3.4. The interaction force between the tip and the sample is measured by detecting the deflection of the cantilever. The static mode topography will be constructed. The tips are attached to the

cantilever with the spring constant that ranges from 0.01 to 10 N/m. This mode can also be operated in the fluid medium with higher resolution to that of air.

3.2.1.2. Dynamic Mode

3.2.1.2.1. Non-Contact Mode

In non-contact mode, the tip is lifted above the sample surface and oscillated above its resonance frequency. This type of mode is where the cantilever oscillates in a distance which is no longer in the repulsive regime of the inter-molecular curve (see figure 3.4). This means that as the tip oscillates above the sample surface, attractive Van der Waals forces act between the tip and the samples. Consequently these forces will be detected and the topography will be constructed. It should be noted that these attractive forces from the sample are very weak compared to the forces used in contact mode, that is why the tip is given a small oscillation so that AC detection method can be employed to detect small forces between the tip and the sample. The Van der Waals forces extend few nanometers above the sample surface. Imaging the true sample surface above the range of Van der Waals forces will fail. This mode is suitable for imaging soft materials.

3.2.1.2.2. Intermittent Mode

In the intermittent mode, the tip is lifted above the sample and oscillated below its resonance frequency. This tapping mode is in the attractive regime of

the inter-molecular curve (see figure 3.4). When the tip is not in contact with the surface, the bimorph makes it oscillate with high amplitude so that when the oscillating tip approaches the sample surface it taps or lightly touches the surface. The feedback loop maintains the cantilever oscillation amplitude. During the tip-sample surface interaction, the cantilever will be deflected. The reflected laser beam will be sent to the feedback loop and converted to an image that contains information on the vertical height of the sample surface and the characteristics of the sample material itself.

3.2.1.3. AFM's Tip Artefacts

General artefacts in AFM are caused by (I) the shape of the tip, thus a tip with different etched angles will produce images with unequal features from the same area when scanned at 0° and 90° , (II) contaminated tip which normally occurs when scanning adhesive sample (see figure 3.5), (III) dull tip in which wears during the use giving out the image with poor resolution and (IV) a tip that has multiple protrusions which may cause a feature in image appear two or more times.

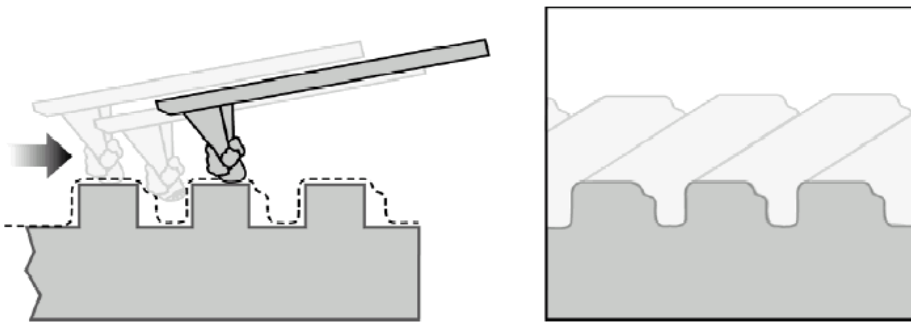


Figure 3. 5: Image artefact caused by contaminated tip.

3.2.2. Magnetic Force Microscopy (MFM)

MFM is a special mode of atomic force microscopy that uses a sharp ferromagnetic probe which interacts with magnetic stray field near the surface. MFM is operated in the non-contact mode where the tip first scans the sample to provide the topographic information, and the second scan will be obtained when the tip is lifted to a non-contact region above the sample in which the magnetic interactions between the tip and the sample will be detected. MFM can be used to investigate the ferromagnetic domains patterns, domain walls, magnetic vortices and flux lines in superconductors.

3.2.2.1. Magnetic Force Imaging

The Multi-mode is set to intermittent mode (tapping mode) and the interleave mode to lift mode. In the first pass, the tip scans over the sample's surface to get topographic information and in the second pass a tip is raised to a height above the sample to get the MFM image. The principle of lift mode is illustrated in figure 3.6. The surface topography and magnetic force images are acquired simultaneously. In the absence of magnetic forces, the cantilever has its resonance frequency f_0 . This frequency is shifted by a value proportional to vertical gradients in the magnetic forces on the tip. The shifts in resonant frequency tend to be very small, i.e., 1-5 Hz for cantilevers having a resonant frequency $f_0 \sim 100$ kHz. These shifts can be detected in three ways: phase detection which measures the cantilever's phase of oscillation relative to the

piezo drive, amplitude detection that tracks variations in oscillation amplitude and frequency modulation that tracks shifts in resonant frequency.

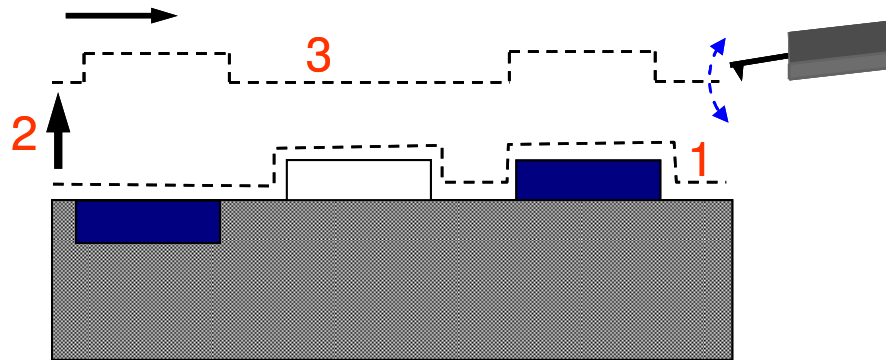


Figure 3. 6: MFM Lift Mode principle demonstrated on a sample with blue areas representing regions which are magnetic.

Where the following numbers in figure 3.6 represent:

- 1 Cantilever traces surface topography on first trace and retrace
- 2 Cantilever ascends to Lift scan Height
- 3 Lifted cantilever profiles topography while responding to magnetic influence on second trace and retrace.

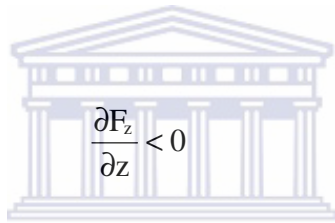
There are different kinds of magnetic domains which contribute to the anisotropy energies. The domain walls (the transition region between the domains) separate the domains and can be defined by the sign of the magneto static interaction between the local surface position and the tip. The types of domain walls include Bloch walls and Neel walls. In an MFM image, the bright contrast represents repulsive force and dark contrast represents attractive force. The Bloch walls can be either represented by dark or bright lines which correspond to an attractive or

repulsive force gradient, respectively. Since the tip is magnetized normal to the surface, the magnetic phase-shift is represented by:

$$\Delta\theta = -\frac{Q}{k} \frac{\partial F_z}{\partial z} \quad (3.1)$$

where F_z is the z-component magnetic force, Q is the quality factor and k is the spring constant.

$$\frac{\partial F_z}{\partial z} > 0 \quad (3.2)$$



$$\frac{\partial F_z}{\partial z} < 0 \quad (3.3)$$

Equation (3.2) represents an attractive interaction which leads to a negative phase shift (dark contrast in the image) while equation (3.3) represents a repulsive interaction which lead to a positive phase shift (bright contrast in the image).

The spatial resolution in MFM imaging is related to the tip-sample distance, i.e. smaller tip-sample distance provide better resolution; conversely, magnetic features smaller than the tip-sample distance may not be resolved. The resolution also depends on the magnetized area of the tip which is actually exposed to the sample stray field.

3.2.3. Scanning Electron Microscopy

3.2.3.1. Introduction

Scanning electron microscope (SEM) is a type of electron microscope that allows the observation and characterization of heterogeneous organic and inorganic materials on nanometer (nm) to micrometer (μm) scale [3.7]. It images the sample surface by scanning it with a high-energy beam of electrons in a raster scan pattern. The electrons interact with the atoms of the sample and produce signals that contain information on sample's topography, composition and other properties such as electrical conductivity. The signals produced when an electron beam interacts with the samples are secondary electrons (SE), backscattered electrons (BSE), characteristic X-rays, cathodoluminescence, specimen current and transmitted electrons (see figure 3.7).

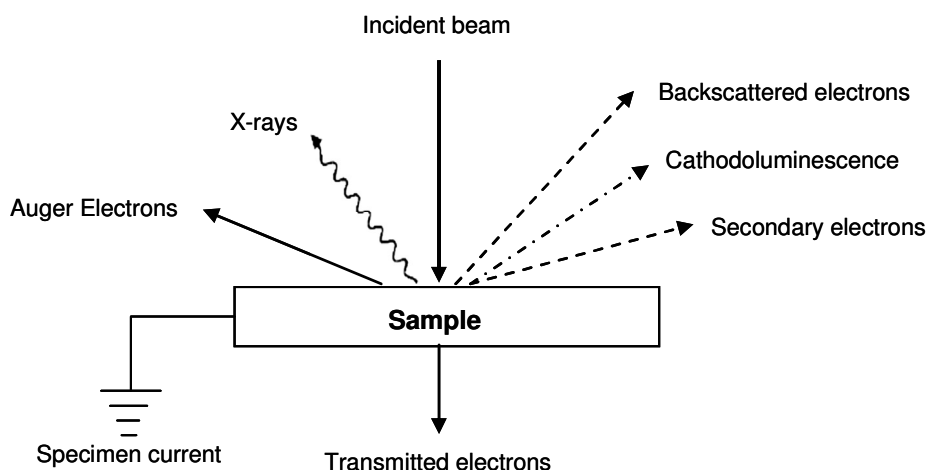


Figure 3. 7: Schematic diagram of the signals generated during the incident beam – sample interaction.

3.2.3.2. Resolution

The resolution can be defined as the closest spacing of two objects which can be viewed through the microscope to be separate entities. Getting images at high magnifications without adequate resolution is not a desired result when operating SEM because there will be no valuable information that can be obtained from the images. Mathematically, the limit of resolution which is the smallest spacing at which two objects are resolved and it can be described by Abbe's equation (3.4).

$$r = \frac{0.612\lambda}{n \sin \alpha} \quad (3.4)$$

where

r	=	limit of resolution,
λ	=	wavelength of the beam,
n	=	refractive index of the medium between the object and the objective lens, and
α	=	aperture angle.

The best resolution (i.e. the smallest r) can be achieved by decreasing λ or increase n or α .

3.2.3.3. Depth of Field and Working Distance

The depth of field (DOF) can be referred to the range of positions for the objects at which our eye cannot detect a change in the sharpness of the image.

The working distance can be defined as the distance between the final condenser lens pole and the top part of the specimen. It influences the depth of field for certain samples. A long working distance, decreases the angle of the aperture resulting in greater depth of field, whereas a shorter working distance results in the sample being scanned with a wider angle (aperture solid angle, α), see figure 3.8.

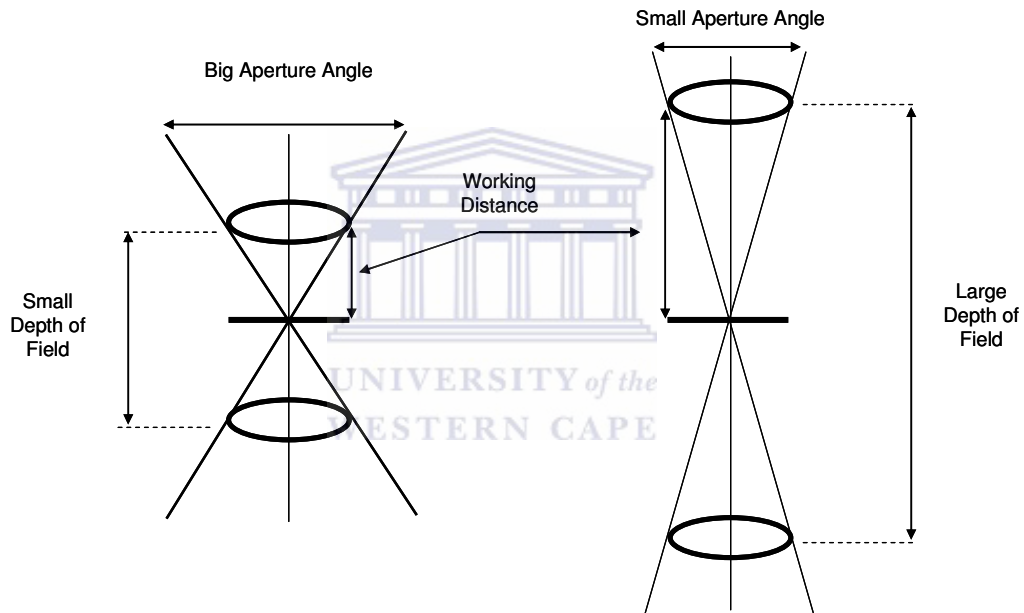


Figure 3. 8: The effect of the working distance on the depth of field seen for the specimen.

The working distance also affects the spherical aberration of the imaging system which in turn influences the resolution of the final image. The spherical aberration results from the geometry of the electromagnetic lenses, which happen when electrons that are near to the beam axis refract less than one focal point, therefore resulting in an enlarged and non-focused spot (see figure 3.9).

Decreasing the working distance makes the spherical aberration to be less, resulting in a smaller but more focused beam spot giving out a better resolved final image.

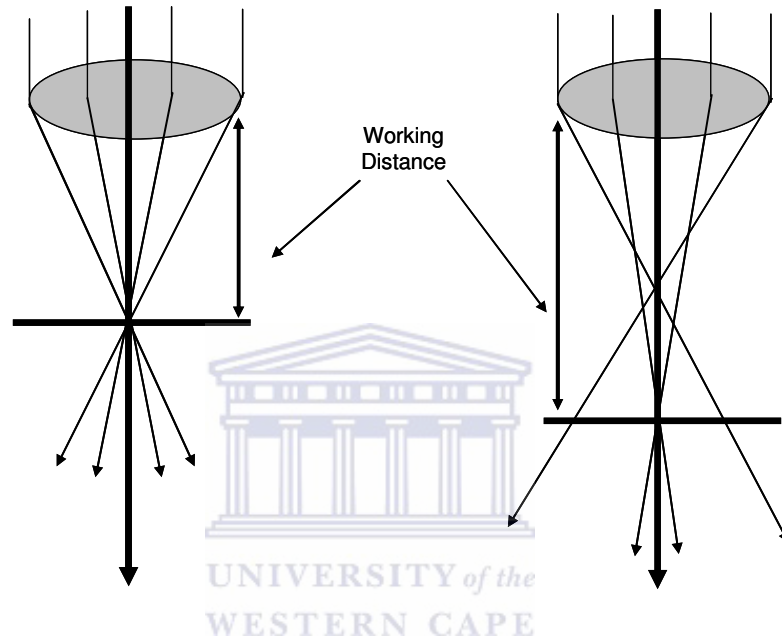


Figure 3. 9: The influence of working distance on the amount of spherical aberration and resolution of the final image.

3.2.3.4. Secondary Electrons

When an incident electron interacts with a sample, the strongest region of the electron energy spectrum is due to secondary electrons (SE). The secondary electrons are produced when an incident electron excites the specimen electron and loses some energy in the process. The excited electron will undergo elastic and inelastic collisions as it moves towards the surface and it will escape the surface if it still has sufficient energy. Their energies are a function of E_0 and

work function (E_w) which determines the amount of energy required to remove electrons from the surface of a materials. Coating a non-conductive specimen with a carbon, gold or gold-palladium layers maximize the number of secondary electron emission. As illustrated in figure 3.10 secondary electrons are emitted in energies less than 50 keV. It represents a small fraction of the electron emitted from the sample.

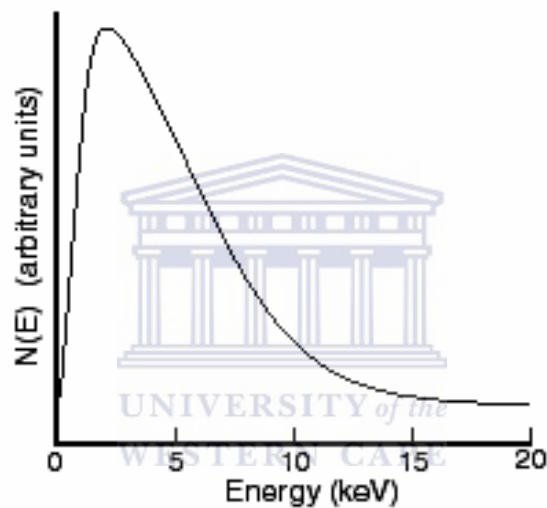


Figure 3. 10:Energy distribution of secondary electrons [3.7].

In many materials the mean free path of secondary electrons is approximately 10 \AA . Even though electrons are generated throughout the excited region by the incident beam, only electrons that originate less than 10 \AA when escaping the specimen will be detected as secondary electrons. The interaction volume is very small compared to BSE and X-rays. As a result SE gives a better resolution than BSE or X-rays and is effectively the same as the electron beam size.

3.2.3.5. Effect of Accelerating Voltage

For low accelerating voltages (≤ 5 kV), the beam interaction with the specimen is in regions close to the surface. It gives the image with detailed information of the surface compared to the images obtained at higher accelerating voltages (15-20 kV) in which the beam penetrates beneath the specimen surface, revealing the information about the interior of the sample.

3.2.3.6. X-Ray Emission

The energy levels of an atom are named energy “shells” and they are labelled as K, L, M, ... with corresponding principle quantum numbers, $n=1, 2, 3, \dots$ (see figure 3.11) [3.8].

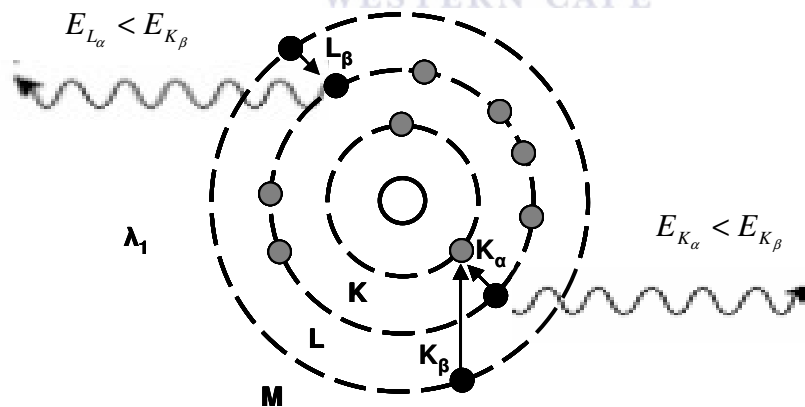
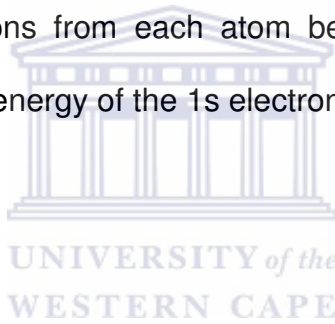


Figure 3. 11:Characteristic x-ray emission by an atom.

When an inner shell electron is excited to leave an atom or to go into a higher unoccupied level, characteristic X-rays are emitted. The electron will be replaced by one of the outer shell electrons conserving energy by emitting an X-ray photon. If you remove an electron from the K-shell (1s) it can be replaced by an electron from either 2p, 3p or any higher occupied state. The transition energy will be released as X-radiation and the emission lines labeled as K_{α} , K_{β} , etc. The X-ray emission for any specimen can provide an analysis of specimen elements constituents, normally in the regions of $1\mu\text{m}$ diameter and $1\mu\text{m}$ depth under normal operating conditions. The K_{α} and K_{β} lines in figure 3.9 have the highest energy X-ray photons from each atom because the energy is nearly closely equal to the binding energy of the 1s electron.



3.2.4. X-ray Diffraction

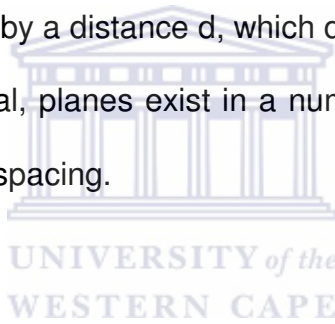
3.2.4.1. Introduction

X-rays are electromagnetic radiation similar to light but with shorter wavelength. Diffraction occurs when waves interfere with a structure whose repeat distance is similar to that of the incident wavelength [3.10]. When it interacts with the sample, the constructive and destructive interference patterns result due to the scattering of the incoming wave fronts by the structure. The wavelength range of x-rays is similar to that of the interatomic spacing found in three-dimensional crystalline structures. This implies that x-rays can be diffracted by these crystalline structures where each atom in the crystalline structure serves

as a scattering center for the incoming wave fronts. This occurrence is known as x-ray diffraction (XRD) and can be employed as a tool for the investigation of the fine, crystalline structure of matter and for quantitative analysis. In the current study, XRD will be employed to study the quantitative on cobalt and manganese oxide deposited on alumina template.

3.2.4.2. Crystal Lattice

A crystal lattice can be thought of as a regular 3-D pattern of atoms in space (cubic, rhombic, etc.). Their arrangement forms a series of parallel planes separated from one another by a distance d , which differs according to the nature of the material. In any crystal, planes exist in a number of different orientations, each with its own specific d -spacing.



3.2.4.3. Bragg's Law

Braggs states that the diffraction of crystalline sample can be elucidated and imaged by using a mirror reflection of the incident x-ray beam from series of crystallographic planes. The Miller indices are parallel to each other and are equally spaced where each plane in a set (hkl) can be considered as a separated scattering object. This set is periodic in the direction perpendicular to the planes and distances between them equals the interplanar distance d_{hkl} . Diffraction from the equally spaced sets is possible at specific angles established from Bragg's law. From figure 3.12, the geometrical analysis results in Bragg's law:

$$2d_{hkl}\sin\theta_{hkl} = n\lambda \quad (3.5)$$

where the n is the order of reflection, λ is the wavelength of the incident wavefront, Δ is the path difference and θ is a Bragg angle.

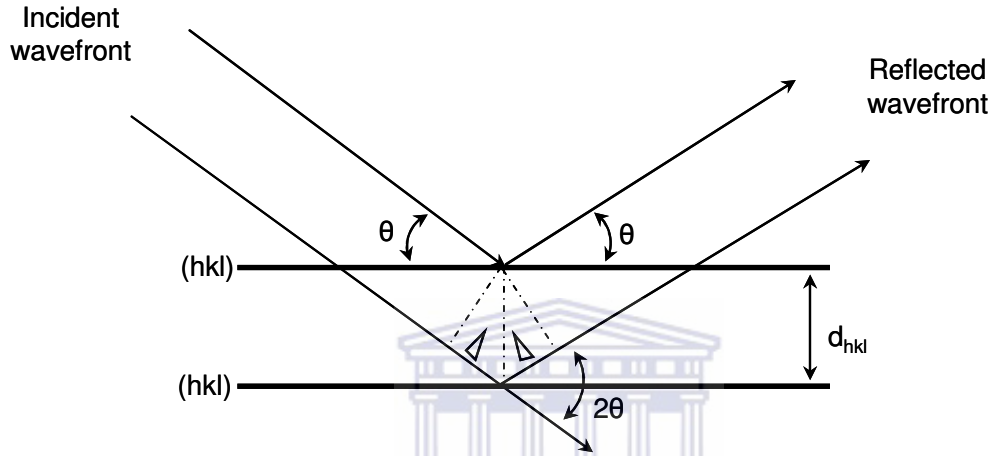


Figure 3. 12: Geometrical illustration of the Bragg's Law [3.9].

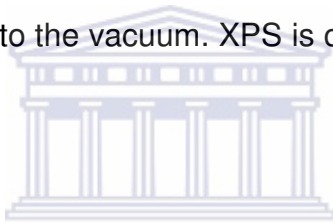
UNIVERSITY of the
WESTERN CAPE

3.2.5. X-ray Photoelectron Spectroscopy (XPS)

XPS uses an electromagnetic wave that interacts with a material or atoms while simultaneously measuring the kinetic energy (KE) [3.10]. It measures electrons that escape the surface of a material from 1 to 10 nm. An electron of a given electronic level is described by its binding energy, E_B which is obtained using the energy conservation law:

$$E_B = h\nu - E_K - \phi \quad (3.6)$$

where E_B is the binding energy, $h\nu$ is the energy of the excitation x-rays, E_K is the kinetic of the emitted photoelectrons and ϕ is the work function. The binding energy E_B is described by the difference between the total energy at the initial state and that at final state of photoelectron emission process. The resulting spectra reflect the electronic structure of a material, giving information on the electron configuration and energy levels within the atoms. The process of photoelectron emission from a solid has three stages: (I) X-rays get absorbed by atoms and photoelectrons are emitted, (II) fraction of the photoelectrons generated within a solid move to the surface, and (III) photoelectrons that reach the surface will be emitted into the vacuum. XPS is operated in ultra high vacuum (UHV) conditions.



3.3. CHARACTERIZATION UNIVERSITY of the WESTERN CAPE

3.3.1. Atomic Force Microscopy (AFM)

The topography examinations were carried out with Digital Instruments Multimode NanoScope Version IV atomic force microscope (AFM) using 0.5 – 2 Ω cm phosphorous (n) doped Si probes with a radius of curvature of 10 nm. The tip has a spring constant of $K \sim 3$ N/m and the resonance frequency $f \sim 75$ kHz. The samples were imaged with the tapping mode (TM).

3.3.2. Magnetic Force Microscopy (MFM)

MFM measurements were taken with Digital Instruments Multimode NanoScope Version IV using Si probes coated with thin film of Fe (MESP-LC) with a radius of curvature of 20 nm, tip height of 10 μm , spring constant of $k \sim 2.8$ N/m and the resonance frequency of $f \sim 75$ kHz. The MFM was run in Tapping Mode and the measurements were taken when the lift heights were varied between 4 nm and 20 nm.

The Si probes (MESP) coated with CoCr thin film with radius of curvature 25 nm, tip height 10 μm , spring constant of $k \sim 2.8$ N/m and the resonance frequency of $f \sim 75$ kHz was also used. Lift height were also varied between 4 nm and 20 nm.



3.3.3. Scanning Electron Microscopy (SEM)

High-resolution scanning electron microscopy, JEOL-JSM 7500F instrument, was used for imaging. Alumina samples (AAO templates) were coated with a thin layer of carbon to minimize the charging effect. Secondary electrons imaging was obtained using a gentle-beam mode with the accelerating voltage of 2.0 kV and the working distance of 4.5 mm. A Neon 40 instrument was also used for imaging using an inlens detector with the accelerating voltage of 5 kV and the working distance of 5 mm. EDX measurements were performed when accelerating voltage was set to 15 kV.

3.3.4. X-Ray Diffraction (XRD)

X-ray diffraction measurements were taken on Co and MnO_x (x = 1,2) nanostructures using Phillips X'pert X-ray diffractometer operating at 45.0 kV and 40.0 mA with CuK_α radiation. XRD data were collected in the range of 5° to 160° with the step size of 0.02°. Peaks were identified using ICDD cards obtained from International Center for Diffraction Data [3.11].

3.3.5. X-Ray Photoelectron Spectroscopy (XPS)

XPS measurements were obtained from Co and MnO_x (x=1, 2) using PHI 5000 Versaprobe – Scanning ESCA Microprobe. The sample surface was cleaned by 2 kV and 2μA on 2 x 2 mm area using Ar ion gun. The instrument was operated at 15 kV and 25 W using a monochromatic Al x-ray beam. Peaks were compared to the spectra listed in the handbook of X-ray photoelectron spectroscopy [3.10].

REFERENCES

- [3.1]. J. Choi, Fabrication Of Monodomain Porous Alumina Using Nanoimprint Lithography, Dr. –Ing. Dissertation, Martin-Luther-Universität Halle-Wittenberg, 05/02/2004
- [3.2]. The Autolab potentiostat, <http://www.ecochemie.nl/>.
- [3.3]. T. S. MKwizu, M. K. Mathe, I. Curoswski, Langmuir, In Press, 2009
- [3.4]. G. Binning, C. F. Quate, Ch. Gerber, Phys. Rev. Lett., 56 (1986) 930 – 933
- [3.5]. B. Bushan, Handbook of Nanotechnology, Issue no. 3, Vol. 24, Springer, 2004
- [3.6]. Digital instruments, MultiMode SPM Instruction Manual, Veeco Instruments Inc. (1996, 1997, 2004)
- [3.7]. J. Goldstein, Scanning Electron Microscopy and X-ray Microanalysis, Third Edition, Springer 2003
- [3.8]. J. W. S. Hearle, J. T. Sparrow, P. M. Cross, The Use of the Scanning Electron Microscope, Pergamon Press Ltd, 1972
- [3.9]. V. K. Pecharsky, P. Y. Zavalij, Fundamentals of Powder Diffraction and Structural Characterization of Materials, Springer Science + Business Media, Inc., 2005
- [3.10]. N. Ikeo, Y. Iijima, N. Niimura, M. Sigematsu, T. Tazawa, S. Matsumoto, K. Kojima, Y. Nagasawa, Handbook of X-ray Photoelectron Spectroscopy, JEOL, 1991

[3.11]. International Center for Diffraction Data, Card Numbers: Co[89-7373],
Al₂O₃[75-0278], Al₂O₃[47-1770], Cu[3-1015] and Cu[3-1015].



CHAPTER FOUR: ALUMINIUM ANODIZATION

4.1. INTRODUCTION

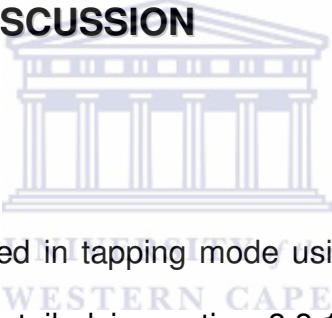
The synthesis of AAO templates has been the subject of interests and employing them to prepare highly ordered nanostructures still receives more attention. These templates were prepared by aluminium anodization which is governed by anodizing parameters detailed in chapter two section 2.4. Investigating the combination of parameters that produce a template with desired hexagonal porous distribution still poses challenges. These parameters depend on each other, if one parameter is changed; it shifts the optimum conditions of the others. Anodization carried out in 0.4 M oxalic acid below 40 V for 60 minutes using a 10 μm thick foil showed no evidence of pore formation whereas anodization carried above 50 V in 0.4 M oxalic acid for 60 minutes produced a template with disordered pore arrangement. It should be noted that our experimental conditions differ from that of O'Sullivan et al. [4.1], where the voltages for anodization in phosphoric acid ranges from 80 to 200 V while for oxalic acid ranges from 30 to 120 V [4.2]. They used a heavy duty aluminium foil (1 mm) and found that pore diameters increased with an increase in anodization voltage. To get an overview on how anodizing parameters influence the pore diameters, pore depths and interpore distances on the template, aluminium anodization carried out in 0.4 M of oxalic acid for 20 minutes at approximately 18 $^{\circ}\text{C}$ at 40 V, 45 V and 50 V were investigated.

Cyclic voltammetric measurements were conducted to identify the voltages suitable to reduce $\text{Co}^{2+}_{(\text{aq})}$ to $\text{Co}_{(\text{s})}$ and $\text{Mn}^{2+}_{(\text{aq})}$ to MnO_x ($x = 1,2$). Deposition parameters were controlled to ensure that deposition selectively takes place in the pores of the templates.

This chapter gives a report on how the anodizing parameters were varied until the combination that produces a template with hexagonal pore array were identified and how the AAO templates were further used when selectively depositing Co and MnO_x ($x = 1,2$) nanostructures in the pores.

4.2. RESULTS AND DISCUSSION

4.2.1. Anodization



The AFM was operated in tapping mode using phosphorus (n) doped Si tips and their parameters detailed in section 3.3.1. Four different areas were scanned on each sample and the representative topographies were selected. Figure 4.1 shows the $2\mu\text{m} \times 2\mu\text{m}$ AFM height topographies obtained from the sample anodized in 0.4 M of oxalic acid for 20 minutes at approximately 18 °C at different voltages. The “grey” scale next to the images shows how high or deep are the parts on the sample. In all the topographies, the sample surfaces were uneven with the evidence of disordered pore distribution and the cracks in figure 4.1(a). The presence of cracks can be ascribed to the local heating at the bottom of the pores which is reported to be due to an inhomogeneous electric field distribution during anodization. This is in agreement with Choi *et al.* [4.2]

observations, which in their study of fabrication of monodomain porous alumina using nanoimprint lithography and its applications found that anodization carried out without controlled temperatures produce alumina samples with cracks and irregular hexagonal pore arrays. The disorder of hexagonal nanopore array can be attributed to the elevated temperatures [4.3]. The reaction rate increases at elevated temperature maximizing the interaction time leading to the formation of disordered hexagonal pore distribution. Setting the temperature to approximately 18 °C in current experiments contributed to formation of these disordered hexagonal pore array.

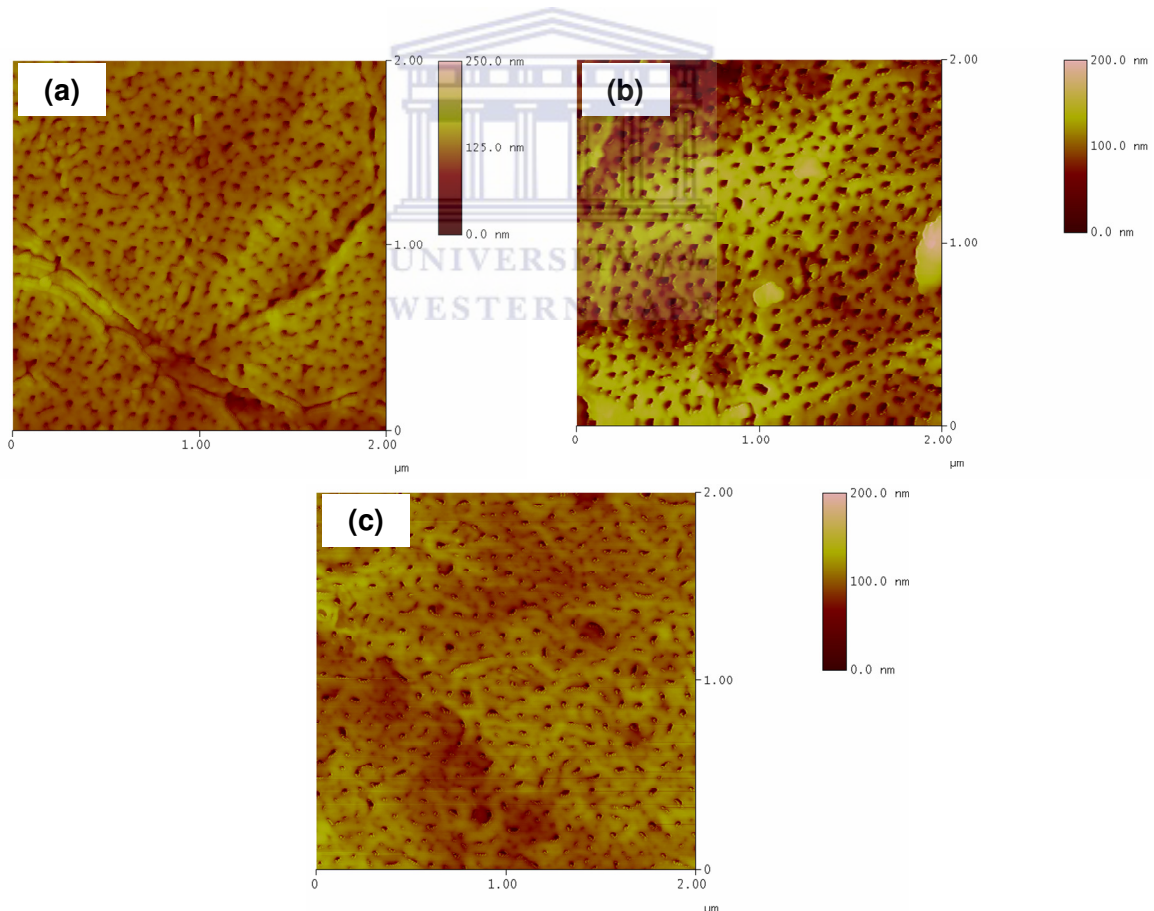


Figure 4. 1: AFM height images of aluminium anodized at (a) 40 V, (b) 45 V and (c) 50 V in 0.4 M Oxalic for 20 minutes at approximately 18 °C.

These observations were supported by the work done by Sulka *et al.* [4.4] where they obtained similar results. In their study they found that anodization carried out at approximately 8 °C and 1 °C using sulphuric acid produced an AAO template with highly ordered hexagonal nanopore array at different cell potentials while anodization carried out at 10 °C produced an AAO template with disordered hexagonal nanopore array. Regardless of the pore arrangement, the topographies in figure 4.1 were compared to investigate how the anodizing voltages influence the pore diameters and depths. When comparing these topographies, it can be seen that the topography in figure 4.1(a) has smaller pores than the one in figure 4.1(b). The results from table 4.1 further support these observations where the topography in figure 4.1(a) has pores with average diameter of 45 nm while figure 4.1(b) has 55 nm. This observation indicates that pore diameters increased with an increase in anodizing voltages at 40 V and 45 V. O'Sullivan *et al.* [4.1] had similar observations when they formed alumina at various constant voltages in the range of 80 to 120 V for 1 h in 0.4 M phosphoric acid at 25 °C, they found that pore diameters increased with an increase in anodizing voltage.

However, the topography in figure 4.1(c) shows pores with the average diameter of 40 nm which is smaller compared to the ones in figure 4.1(a) and (b). The results show that pore diameters decreased with an increase in anodizing voltage, i.e. anodization at 45 V and 50 V. This is contrary with the observation

already being done on the subject [4.1, 4.5]. The observations suggest that for a specific combination of parameters, there are boundaries which if you go beyond, the optimum combination of anodizing parameters will be shifted [4.6]. In the current study this behavior resulted because only the anodizing voltages were varied while the temperature, time and concentration were kept constant. That is, anodization at 50 V shifted the combinations suitable for synthesizing highly ordered AAO template. It was for this reason that Sulka *et al.* [4.7] varied all parameters until the ordered hexagonal pore distribution was achieved [4.5]. Their results were further used to investigate the influence of anodizing potential to pore diameters. Generally, the topographic observations depict that anodization performed at 45 V produced larger and visible pore with the average diameter of 55 nm compared to the ones performed at 40 V with average diameter of 45 nm and 50 V with average diameter of 40 nm.

Figures 4.2(a), (b) and (c) illustrate the HRSEM top view for alumina anodized at 40 V, 45 V and 50 V respectively. Prior analysis, the alumina (AAO templates) samples were sputtered with carbon layer to minimize the charging effect. These top views agree with AFM's observations, with the assistance of the scale bar, figure 4.2(b) clearly shows that it has larger pore diameters compared to 4.2(a) and (c). The bright parts that exist at the edges of the pores in figure 4.2(b) are due to the charging effect. The pores were wider and reduced the uniformity of coating by carbon layer. The effect of elevated anodizing voltages caused the sample in figure 4.2 (c) to appear rougher than the samples in figures

4.2 (a) and (b). This was due to the intensified mean velocity of ionic migration
[4.8]

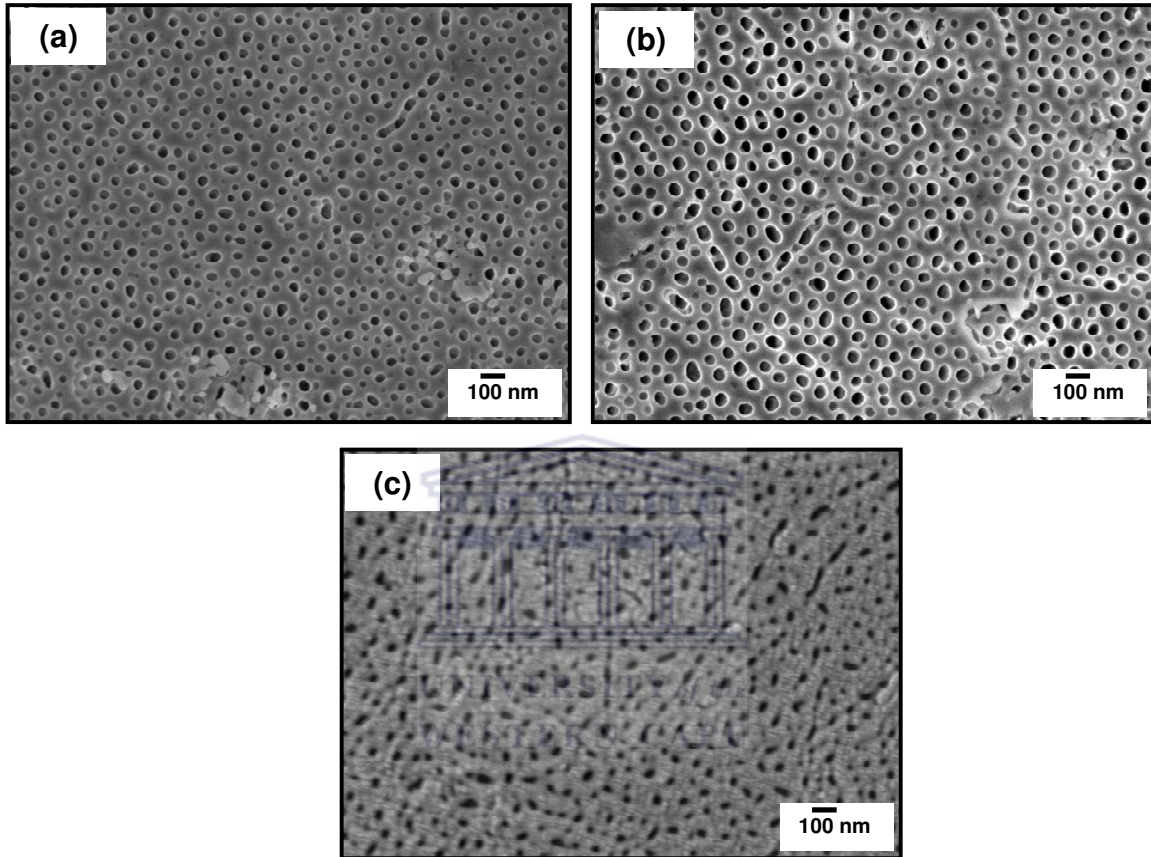


Figure 4. 2: HRSEM images of anodized Al foil in 0.4M oxalic acid at (a) 40 V, (b) 45 V and (c) 50 V for 20 minutes at approximately 18 °C respectively.

Using AFM offline software, section analyses were performed on samples anodized at 40 V, 45 V and 50 V. In all three samples, pore diameters and pore depths were measured from sixty (60) randomly selected pores to generate the statistical data from which the results are summarized in Table 4.1.

Anodizing Voltage [V]	Average Pore Diameters [nm]	Pore Diameters Standard Deviation	Average Pore Depth [nm]	Pore Depths Standard Deviation
40	45	7.63	61	17.5
45	55	9.15	78	33.4
50	40	8.26	72	29.33

Table 4. 1: Influence of anodizing potential to pore diameters and depths.

Pore average diameters in table 4.1 agree with observations on AFM images in figure 4.1 and SEM top views in figure 4.2. Average pore diameters increased in figure 4.1(a) to (b). Figure 4.1(c) showed a decrease and the image texture looks different compared to figure 4.1(a) and (b). Similar trend was also observed on SEM images in figure 4.2. However, the average values further support the topographic observations that pore diameters increased with an increase in anodizing voltages from 40 V to 45 V while the increase in anodizing potential from 45 V to 50 V shows a decrease in pore diameters. Based on these results, combination of anodizing parameters such as 45 V, 0.4 M oxalic, 20 minutes and approximately 18 °C found to have synthesized an AAO template with larger pore diameters and deeper pore depths compared to anodization carried out at 40 V and 50 V. This combination was selected for further investigations. The selection was due to the fact that the AAO template was going to be used to selectively electrodeposit magnetic nanostructures in pore template and choosing a template with larger pores and deeper pore maximizes the probability of deposition into the pores.

Figure 4.3 depicts the (a) 2 $\mu\text{m} \times 2 \mu\text{m}$ AFM height topography and (b) its 3D surface plot of aluminium anodized in 0.4 M of oxalic acid for 60 minutes at approximately 8 $^{\circ}\text{C}$. The topography showed reduced surface unevenness and improved uniformity of the pore distribution compared to the topographies in figure 4.1(b).

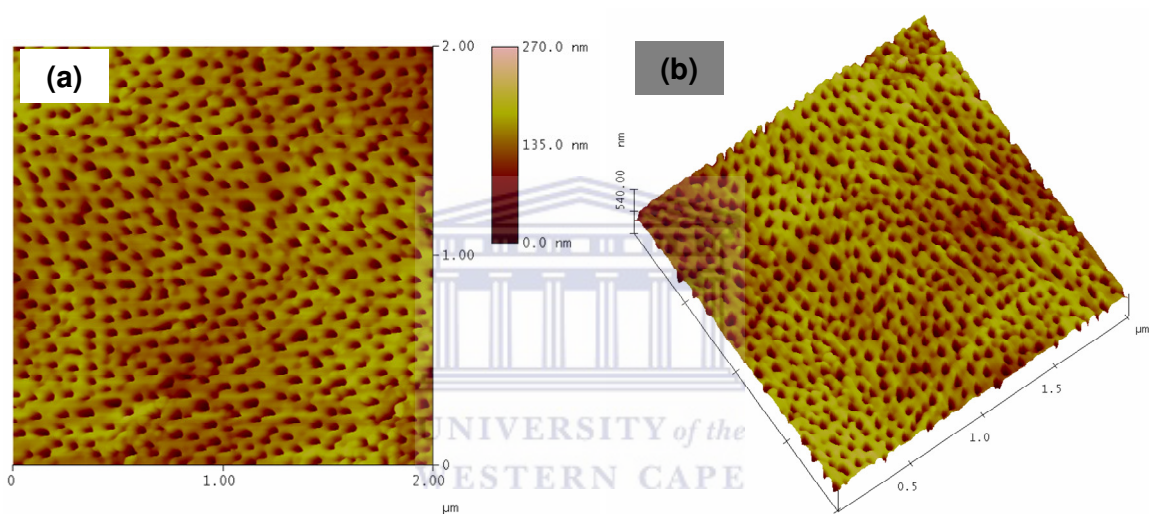


Figure 4. 3: (a) AFM height image and (b) its 3D surface plot of aluminium anodized at 45 V in 0.4 M Oxalic for 60 minutes at approximately 8 $^{\circ}\text{C}$ respectively.

The average pore diameter was found to be 80 nm and the average pore depth was 105 nm. The average values show that lowering the anodizing temperature and that longer anodizing period improves the hexagonal array of pore. Comparing the average values of pore diameters and pore depths obtained from samples anodized at 45 V in 0.4 M oxalic acid for 20 minutes at approximately 18 $^{\circ}\text{C}$ in table 4.1, it can be seen that by lowering the temperature

and expanding the anodization period increases the pore diameters and depths. This observation can be ascribed to the fact that when the temperature was lowered, the reaction rate decreased which increased the interaction time for the self-organization of the pores. The extension of anodizing period also gave more time for the reaction rate to maximize the growth of pore diameters as well as pore depths. The topography in figure 4.3 also showed that anodization carried out at lower temperature yield pore with higher symmetry which agrees with what was observed by Ba *et al.* [4.3] in their study of the influence of anodizing condition on the ordered pore formation in anodic alumina. They reported that higher anodizing temperatures increase the reaction rate at certain acid concentration and high reaction rate lead to more disordered pore distribution. Hence lower temperatures yield higher pore symmetry.

Figure 4.4(a) shows the SEM cross-section view of alumina with pores that grew in cylindrical tubes perpendicular to the surface of aluminium foil and the growth extend through the foil. The area marked by “A” in figure 4.4(b) represents a part in which the layer of sample surface was peeled off while “B” represents part that remained unpeeled. It can be seen that the area represented by “A” has well-ordered hexagonal pore array than the area marked by “B”.

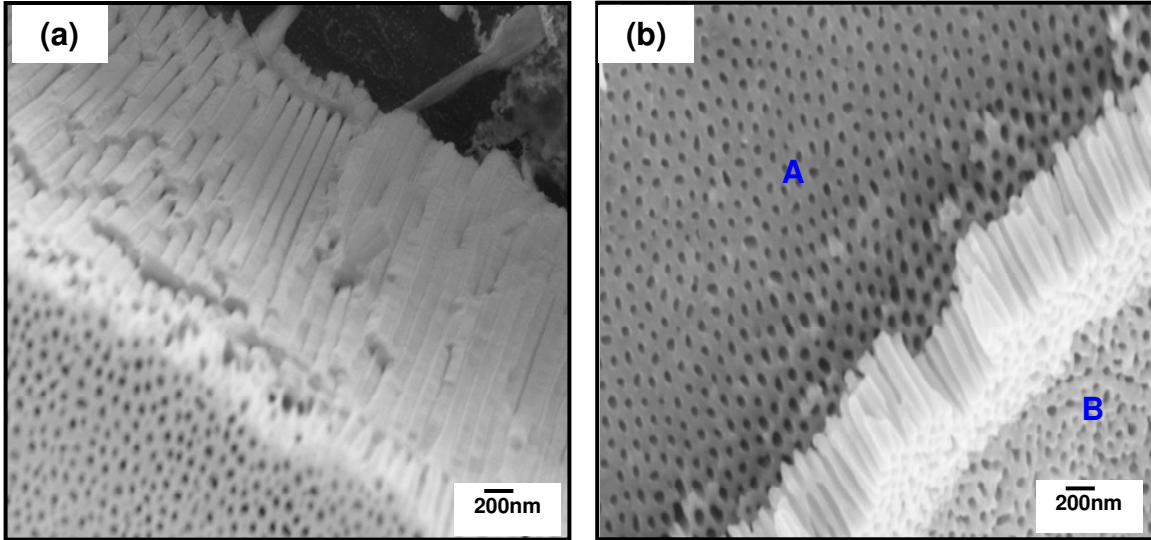
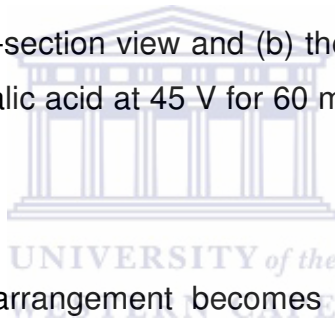


Figure 4. 4: SEM (a) cross-section view and (b) the peeled area of anodized Al foil in 0.4M oxalic acid at 45 V for 60 minutes at approximately 8 °C respectively.



This suggests that pores arrangement becomes more perfect as they grow through the foil. That is the reason why we have to slightly chemically etch the top most part of alumina to reveal the highly ordered pore array. The unpeeled area “B” on the SEM top view in figure 4.4(b) shows similar observations to the AFM’s topography in figure 4.3(a). Figure 4.4(b) for both peeled area “A” and unpeeled area “B” generally shows that the hexagonal array of the pores improved compared to topographies in figure 4.2.

Figure 4.5(a) represents the 2 μm x 2 μm AFM height image and (b) its 3D surface plot of aluminium anodized at 45 V in 0.4 M Oxalic for 120 minutes at approximately 8 °C. The sample surface in figure 4.5(a) shows pores with highly ordered hexagonal array. Its corresponding 3D surface plot in figure 4.5(b)

depicts uneven sample surface and also confirms that pores grew perpendicular to the sample surface (supports the observation in figure 4.4).

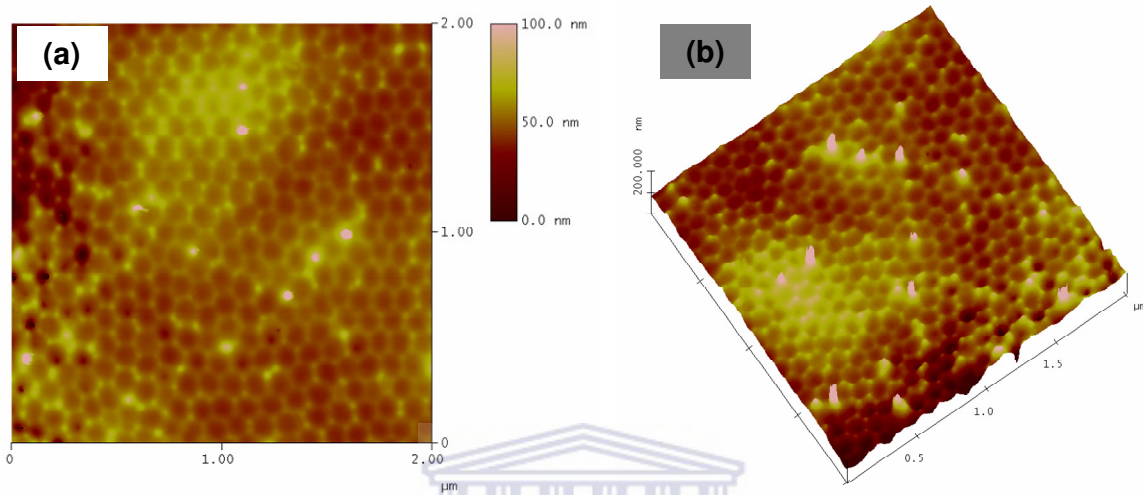


Figure 4. 5: (a) AFM height image and (b) its 3D surface plot of aluminium anodized at 45 V in 0.4 M Oxalic for 120 minutes at approximately 8 °C respectively.

UNIVERSITY of the
WESTERN CAPE

The pore average pore diameter increased from 80 nm to 103 nm when compared to the results obtained when the anodizing period was 60 minutes and these results further confirm that longer anodizing periods do improve the regularity of pore distribution of alumina. Figure 4.6 represents the SEM topview of aluminium foil anodized in 0.4 M oxalic acid at constant potential of 45 V for 120 minutes at approximately 8 °C. The bright spots on the SEM topview can be attributed to the contaminations. The image shows an ordered hexagonal pore structure with brighter edges of the pores. From the SEM top view it can be seen the pore diameters has a diameter sizes of about 100 nm. These values are

very close to the value of pore average diameter size obtained in the AFM topography using section analyses.

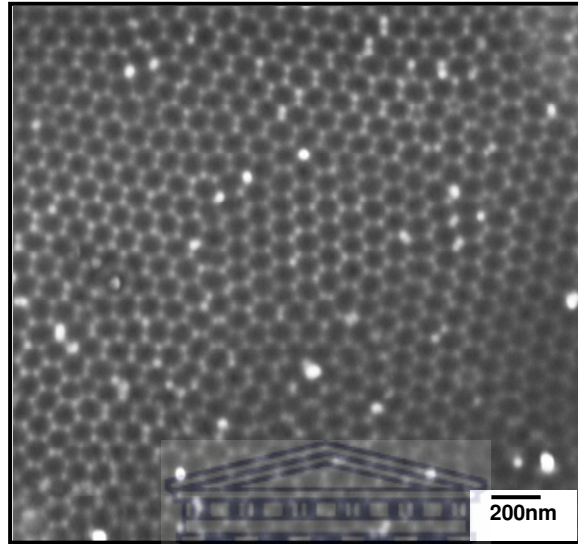


Figure 4. 6: SEM images of anodized Al foil in 0.4M oxalic acid at 45 V for 120 minutes at approximately 8 °C.

The topographic observations show that anodization carried out in 0.4 M oxalic acid at 45 V for 120 minutes at approximately 8 °C produced a desired and highly ordered AAO template. Therefore, these combinations were further used to replicate the template. Templates were used for the deposition of the nanostructures. The next section present the results on Co nanostructures which were selectively deposited in the pores of AAO template and will be followed by the results of MnO_x ($x = 1,2$) nanostructures deposition.

Prior to cyclic voltametric measurements and electrodeposition of nanostructures, the AAO templates were coated at the back with Au-Pd layer and supported with copper adhesive tape (see figure 4.7).

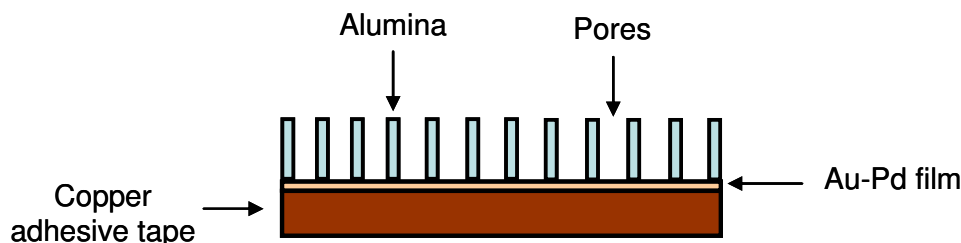


Figure 4. 7: AAO template coated at the back by Au-Pd film and supported by copper adhesive tape.

4.2.2. Electrodeposition of Cobalt

The mechanism of cobalt deposition on the unanodized aluminium foil and anodized alumina coated at the back with Au-Pd film was performed using cyclic voltammetry. Figure 4.8 represents the cyclic voltammogram measured on aluminium foil in a solution of 0.12 M CoSO_4 + 0.49 M H_3BO_3 with pH 5. The reduction of Co^{2+} to $\text{Co}_{(s)}$ started at -0.92 V. When reversing at -1.3 V, the reduction of cobalt continued up to -0.68 V. Only one crossover was seen at -0.48 V in which the predominant dissolution of cobalt started and followed by the anodic current at -0.20 V, beyond which complete dissolution of $\text{Co}_{(s)}$ to Co^{2+} took place. The broadness of the peak is related to different oxidation of cobalt phases such as $\text{Co}(\text{OH})_{2(s)}$ [4.9, 4.10].

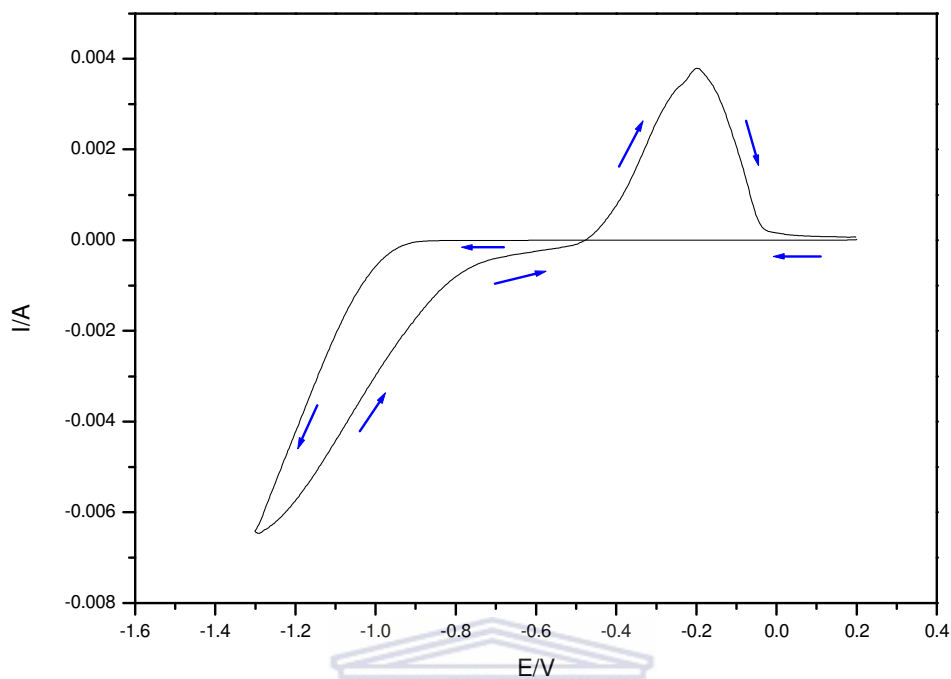


Figure 4. 8: Cyclic voltammogram on aluminium foil (unanodized) measured in solution containing 0.12 M CoSO_4 + 0.49 M H_3BO_3 at pH 5.

Figure 4.9 illustrates measurements which were done on alumina coated at the back with Au-Pd film in 0.12M CoSO_4 + 0.49M H_3BO_3 at pH 5. The reduction of Co^{2+} to $\text{Co}_{(s)}$ began at -0.90 V. When reversing at -1.3 V, the reduction of cobalt continued up to -0.74 V. Two crossovers were seen, at -1.2 V and -0.84 V which correspond to nucleation growth and overpotential respectively [4.10].

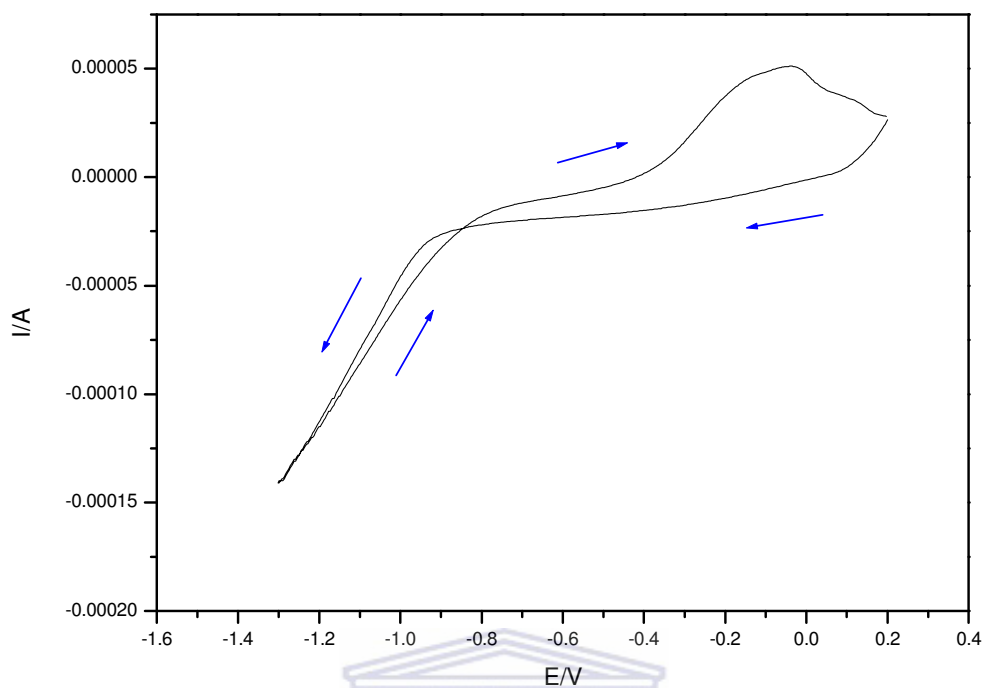


Figure 4. 9 : Cyclic voltamogram on anodized alumina coated with Au-Pd film measured in solution containing 0.12 M CoSO_4 + 0.49 M H_3BO_3 at pH 5.

UNIVERSITY of the
WESTERN CAPE

The predominant dissolution of cobalt began at -0.38 V followed by the anodic peak at -0.04 V.

The CV measurement provided the insights of the reduction of cobalt on aluminium foil (unanodized) and anodized alumina coated at the back with Au-Pd film. In the voltages between -0.89 V and -1.3 V, Co^{2+} ions will be reduced to Co metal and the competing process of hydrogen evolution could also happen. CV suggests that the deposition of cobalt on anodized alumina coated with Au-Pd is energetically more favourable than unanodized aluminium foil. This is because the Au-Pd layer is more conductive than the unanodized aluminium foil which has a thin oxide layer on the surface. Judging from voltages at which the deposition

and the dissolution occur. Based on CV results, electrodeposition of Co nanostructures was carried out at -1.1 V between 30 and 60 minutes.

Figure 4.10 (a) shows the AFM height topography of 2 μm x 2 μm scan area and (b) the SEM top view of cobalt nanostructures prepared on AAO template respectively. The Co nanostructures were selectively electrodeposited in the pores of AAO template from mixture of 0.12 M CoSO_4 and 0.49 M H_3BO_3 when the voltage was set to -1.1 V. Bright areas in figure 4.10(a) represent the highest parts of the sample and it can be seen from the grey scale that highest parts were about 40 nm.

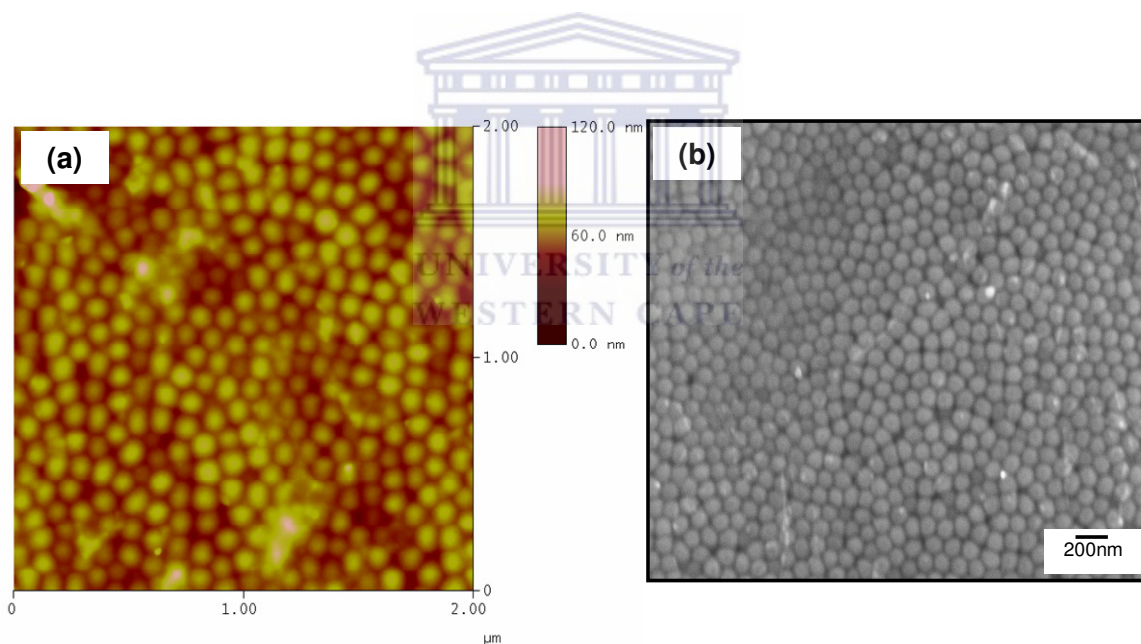


Figure 4. 10:AFM height topography (a) and SEM top view (b) of cobalt nanostructures prepared on AAO template from a mixture of 0.12 M CoSO_4 and 0.49 M H_3BO_3 applying the voltage of -1.1 V.

The uneven sample surface on the cobalt nanostructures was observed which can be attributed to the uneven surface of the AAO template (see figure 4.5).

Small separation that ranges from 12 nm to 20 nm between the nanostructures and few agglomerated nanostructures can be observed. The grown Co nanostructures correspond to the pore hexagonal array of the template. The diameters of the nanostructures correspond to the pore diameters of the template. Their diameters ranged from 80 nm to 110 nm and average heights were about 20 nm. The SEM top view in figure 4.10(b) represents Co nanostructures prepared on AAO template from mixture of 0.12 M CoSO_4 and 0.49 M H_3BO_3 . This top view confirms AFM's observations and it can be seen that the nanostructures conformed to hexagonal array of the template.

The samples (Co nanostructures prepared on AAO) were taken for elemental analysis in which the HRSEM was used to measure energy dispersive x-rays (EDX). Figure 4.11 shows EDX spectrum of Co nanostructures prepared on AAO template from mixture of 0.12 M CoSO_4 and 0.49 M H_3BO_3 when the voltage was set to -1.1 V. Two peaks of Co at 0.77 KeV (indicated by a blue arrow) and 6.9 KeV confirms the presence of Co elements. The O and Al signal results from the AAO. The S peak comes from the cobalt sulphate salt which was used as a precursor for cobalt while the P comes from phosphoric acid which was used for pore widening.

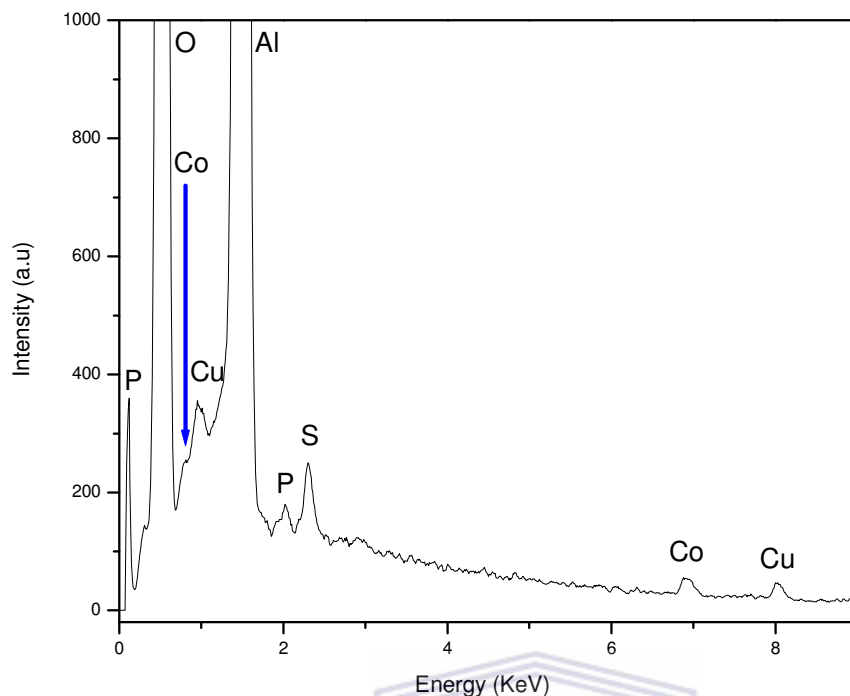


Figure 4. 11:EDX spectrum of cobalt nanostructures prepared on AAO template from a mixture of 0.12 M CoSO_4 and 0.49 M H_3BO_3 applying the voltage of -1.1 V.

UNIVERSITY of the
WESTERN CAPE

The copper peaks result from the copper tape which was used to support the template prior to electrodeposition. For further investigations, the X-ray diffraction was done for elemental composition.

X-ray diffraction measurement were performed on Co nanostructures prepared on AAO template from mixture of 0.12 M CoSO_4 and 0.49 M H_3BO_3 when the voltage was set to -1.1 V using Phillips X'pert X-ray diffractometer detailed in chapter three section 3.3.4. Figure 4.12 illustrates the XRD pattern of Co nanostructures prepared on AAO template. Peaks were identified using ICDD cards obtained from joint committee for powder diffraction studies [4.11]. The Co (002) plane was observed and confirms the presence of cobalt element.

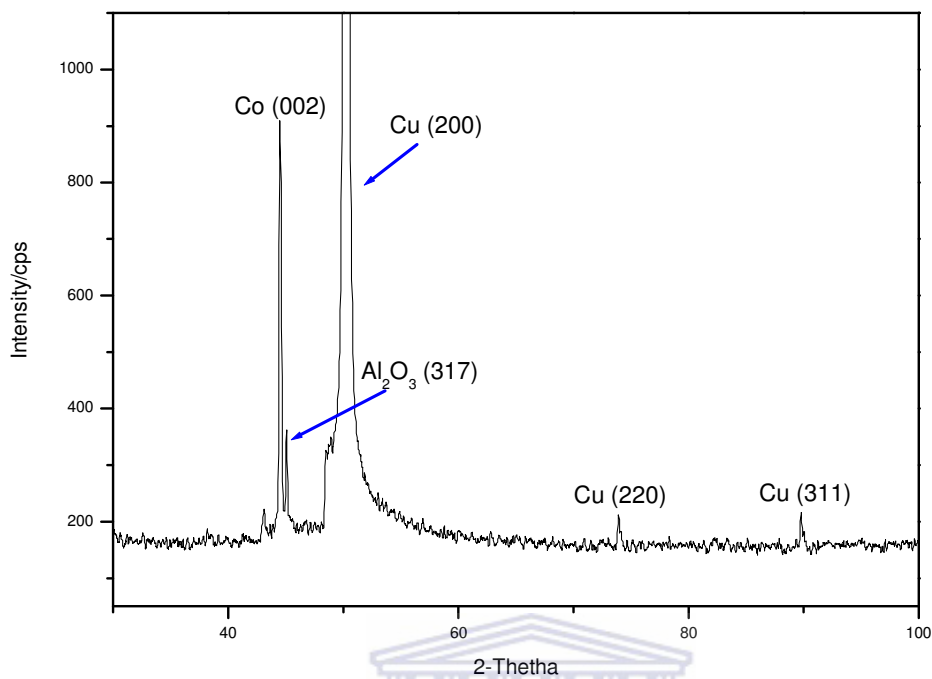


Figure 4. 12: XRD pattern of cobalt nanostructures prepared on AAO template from a mixture of 0.12 M CoSO_4 and 0.49 M H_3BO_3 applying the voltage of -1.1 V.

The Al_2O_3 (317) plane comes from the AAO template (alumina). Planes such as Cu (200), Cu (220) and Cu (311) were also observed which results from the copper adhesive tape used as a supporting material.

X-ray photoelectron spectroscopy (XPS) measurements were conducted on Co nanostructures prepared on AAO templates using PHI 5000 Versaprobe – Scanning ESCA Microprobe. The peaks were identified using the reference spectra listed in the Handbook of X-ray Photoelectron Spectroscopy [4.12]. Figure 4.13 shows the XPS spectra obtained from Co nanostructures prepared on AAO template.

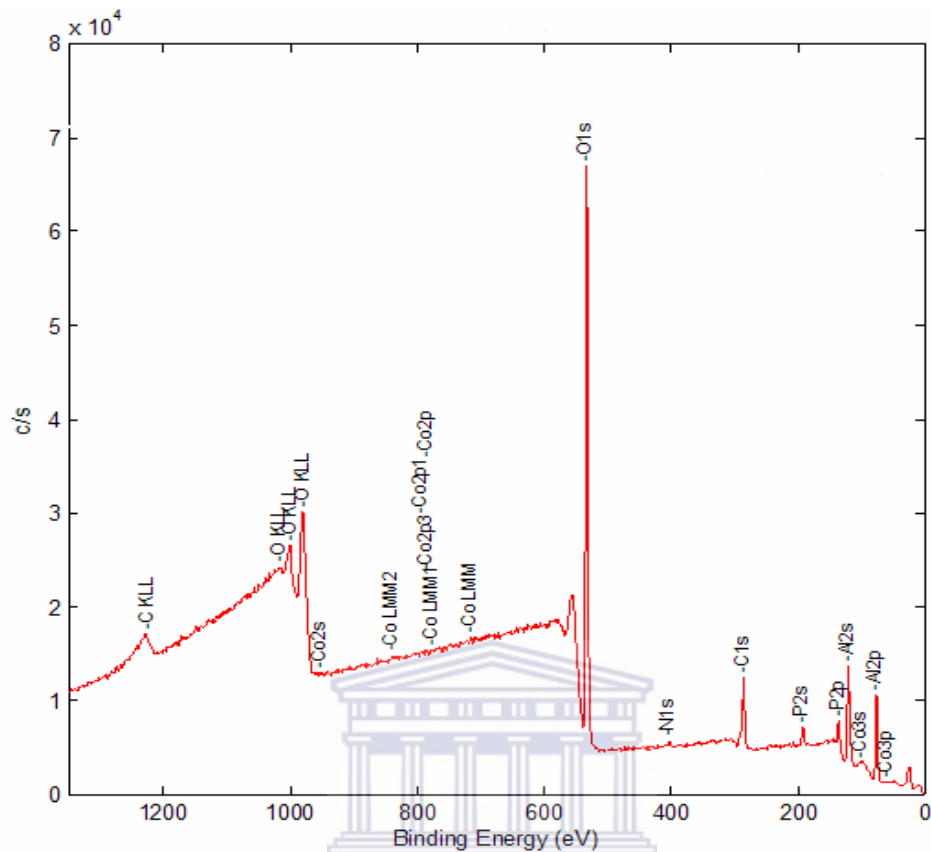


Figure 4. 13: XPS spectra Co nanostructures prepared on AAO template from a mixture of 0.12 M CoSO_4 and 0.49 M H_3BO_3 applying the voltage of -1.1 V.

The XPS spectra show the peaks for all the possible elements present in the sample. The peak of Co3s with binding energy of 101.35 eV was identified and corresponds to Co on the reference spectra. The peaks of $\text{Co}2p_{1/2}$ with the binding energy of 795.40 eV and $\text{Co}p_{3/2}$ with the binding energy of 780.40 eV were identified in the background noise (clearly illustrated in figure 4.14). These peaks correspond to the reference spectra of Co_2O_4 .

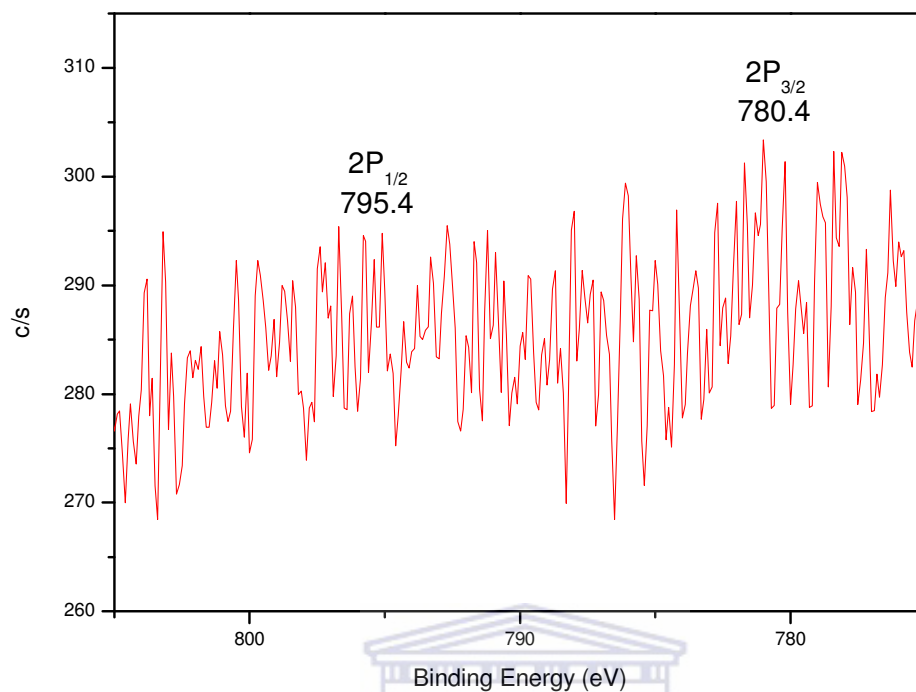


Figure 4. 14: A zoomed XPS spectra from the one in figure 4.13 of Co nanostructures with peaks corresponding to reference spectra of Co.

The results confirm the presence of Co element in the nanostructures supporting the XRD and EDX measurements. Peaks for Al come from alumina (AAO template), P is residual of phosphoric acid used for pore widening, C resulted from the residual of oxalic acid during template synthesis and O contributed to the formation of both Co and Co₂O₄.

4.2.3. Electrodeposition of Manganese oxide

Figure 4.15 illustrates the cyclic voltammogram of anodized alumina (AAO template) coated at the back with Au-Pd film in 0.3 M manganese (II) chloride

tetrahydrate ($\text{MnCl}_2 \cdot 4\text{H}_2\text{O}$). The reduction of Mn^{2+} to MnO_x ($x = 1,2$) started at +1.16 V. A bump at 0.3 V, 0.9 V, 0.84 V and 0.6 V show different possible phases of MnO_x ($x = 1,2$) deposition.

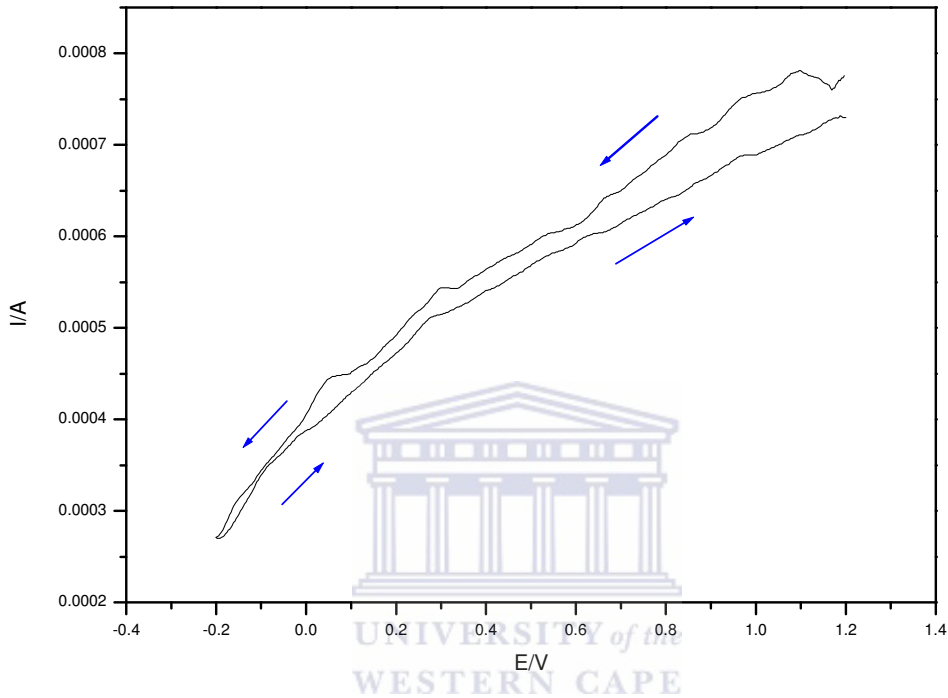


Figure 4. 15: Cyclic voltammogram on anodized alumina coated with Au-Pd film measured in a solution containing 0.3 M of manganese (II) chloride tetrahydrate ($\text{MnCl}_2 \cdot 4\text{H}_2\text{O}$).

When reversing at -0.2 V, the oxidation of MnO_x ($x = 1,2$) to Mn^{2+} could not be observed. This behavior suggests that the deposition of MnO_x ($x = 1,2$) was not reversible and this was probably caused by the formation of oxides. Based on the CV measurements, the voltage of +1.1 V was selected for the deposition of MnO_x ($x = 1,2$) nanostructures and the deposition times were varied between 30 to 60 minutes.

Figure 4.16(a) represents the AFM height topography of 2 μm x 2 μm area and (b) the SEM top view of MnO_x ($x = 1,2$) nanostructures prepared on AAO template from 0.3 M manganese (II) chloride tetrahydrate ($\text{MnCl}_2 \cdot 4\text{H}_2\text{O}$). The sample surface in figure 4.16(a) was uneven and the depositions of the structures larger than 100 nm were observed.

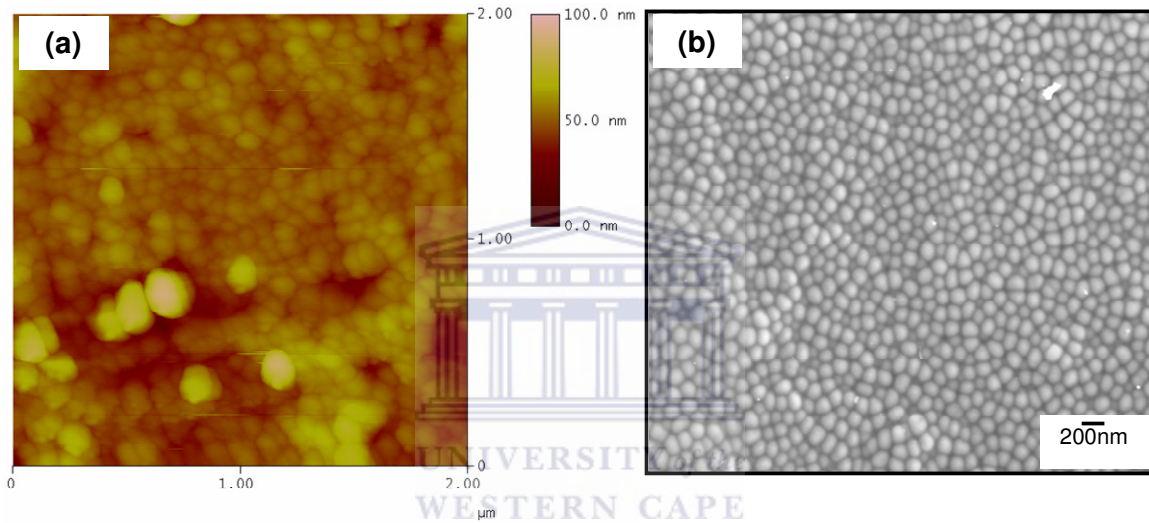


Figure 4. 16: AFM height topography (a) and SEM top view (b) of MnO_x ($x = 1,2$) nanostructures prepared on AAO template from a solution of 0.3 M $\text{MnCl}_2 \cdot 4\text{H}_2\text{O}$ when the voltage was set to +1.1 V.

The hexagonal array of the nanostructures could not be clearly identified. The tip artifacts also contributed to the poor imaging of the MnO_x ($x = 1,2$) nanostructures (as discussed in chapter three section 3.2.1.3). However, its corresponding SEM top view in figure 4.16(b) clearly shows ordered nanostructures. The presence of structures with sizes larger than 100 nm was also observed.

To determine the presence of Mn element, EDX measurements were done on MnO_x ($x = 1,2$) nanostructures prepared on AAO. Figure 4.17 illustrates EDX spectrum of MnO_x ($x = 1,2$) of nanostructures prepared on AAO. A peak of Mn at 5.9 keV confirms the presence of manganese element.

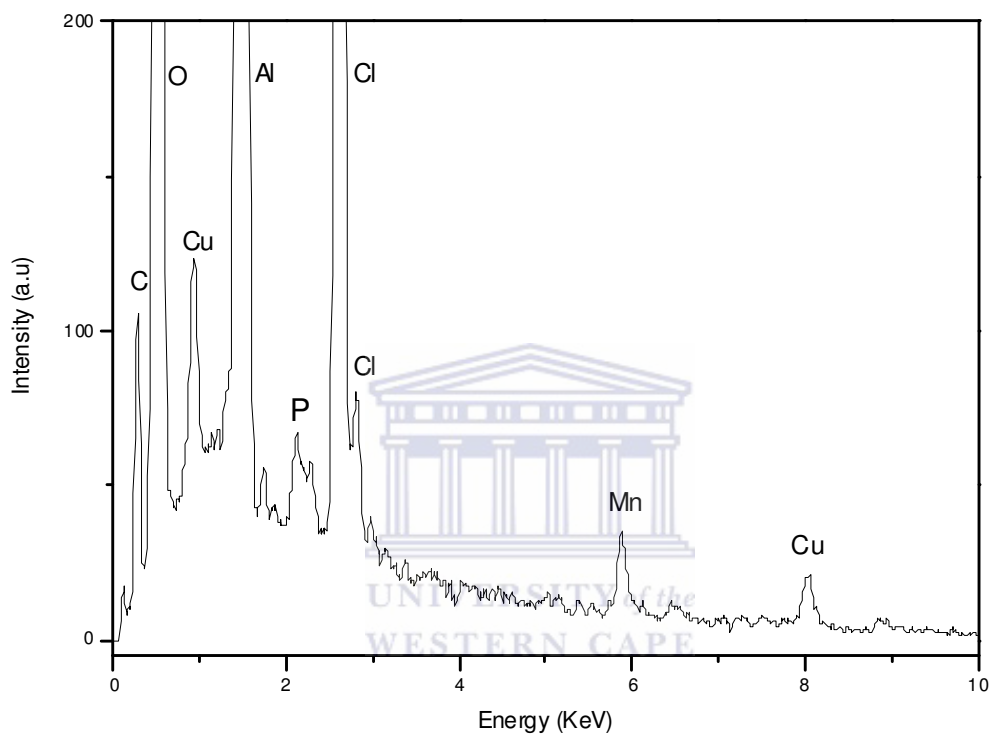


Figure 4. 17: EDX spectrum of MnO_x ($x = 1,2$) nanostructures prepared on AAO template from a solution of 0.3 M $\text{MnCl}_2 \cdot 4\text{H}_2\text{O}$ when the voltage was set to +1.1 V.

The O and Al peaks come from the template as well as the O from MnO_x ($x = 1,2$). Cu peaks come from the copper adhesive tape while Cl peaks results from the precursor and P is from phosphoric acid used for pore widening.

XRD measurements were performed on MnO_x ($x = 1,2$) nanostructures prepared on AAO template. ICDD cards were used to identify the peaks [4.11]. Figure 4.18 shows the XRD pattern of MnO_x ($x = 1,2$) nanostructures in which

MnO₂ (220) plane confirms the presence of manganese (IV) oxide. Cu (111), Cu (200), Cu (220) and Cu (311) planes result from the copper adhesive tape used to support the alumina during deposition. The Al₂O₃ (220) plane comes from the AAO template.

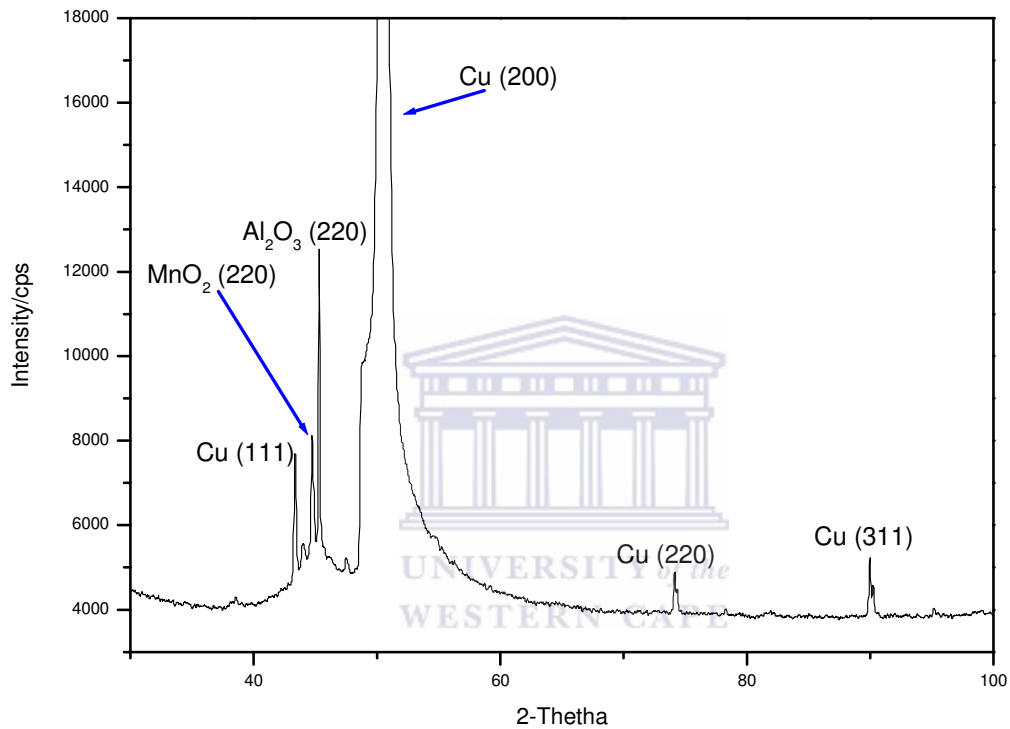


Figure 4. 18: XRD pattern of MnO_x (x = 1,2) nanostructures prepared on AAO template from a solution of 0.3 M MnCl₂.4H₂O when the voltage was set to +1.1 V.

X-ray photoelectron spectroscopy (XPS) measurements were done on MnO_x (x = 1,2) nanostructures prepared on AAO templates. The peaks for MnO_x (x = 1,2) were identified using the reference spectra listed in the Handbook of X-ray Photoelectron Spectroscopy [4.12]. Figure 4.19 shows the XPS spectra obtained from MnO_x (x = 1,2) nanostructures prepared on AAO template.

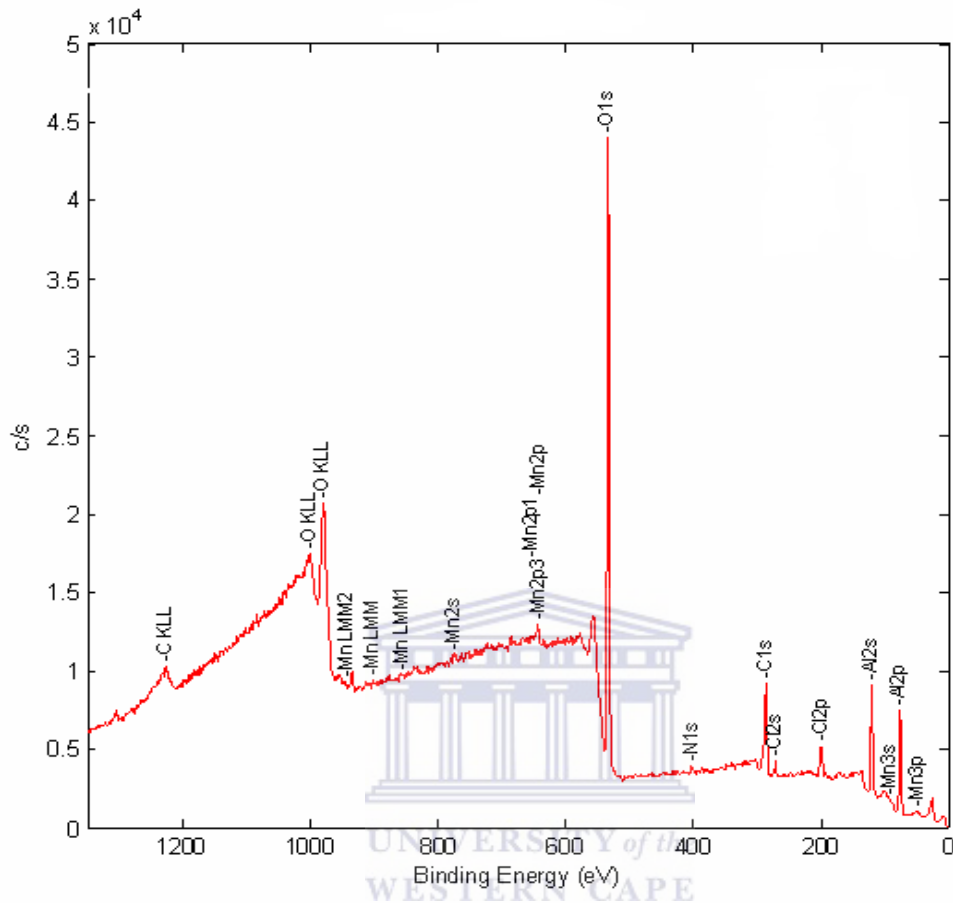


Figure 4. 19: XPS spectra MnO_x ($x = 1,2$) nanostructures prepared on AAO template from a solution of $0.3 \text{ M MnCl}_2 \cdot 4\text{H}_2\text{O}$ when the voltage was set to $+1.1 \text{ V}$.

The XPS spectra show the peaks for all the possible elements present in the sample. The following peaks Mn $2p_{1/2}$ with the binding energy of 653.64 eV and Mn $2p_{3/2}$ with the binding energy of 642.59 eV were identified (clearly illustrated in figure 4.20). These peaks correspond to the reference spectra of MnO_2 .

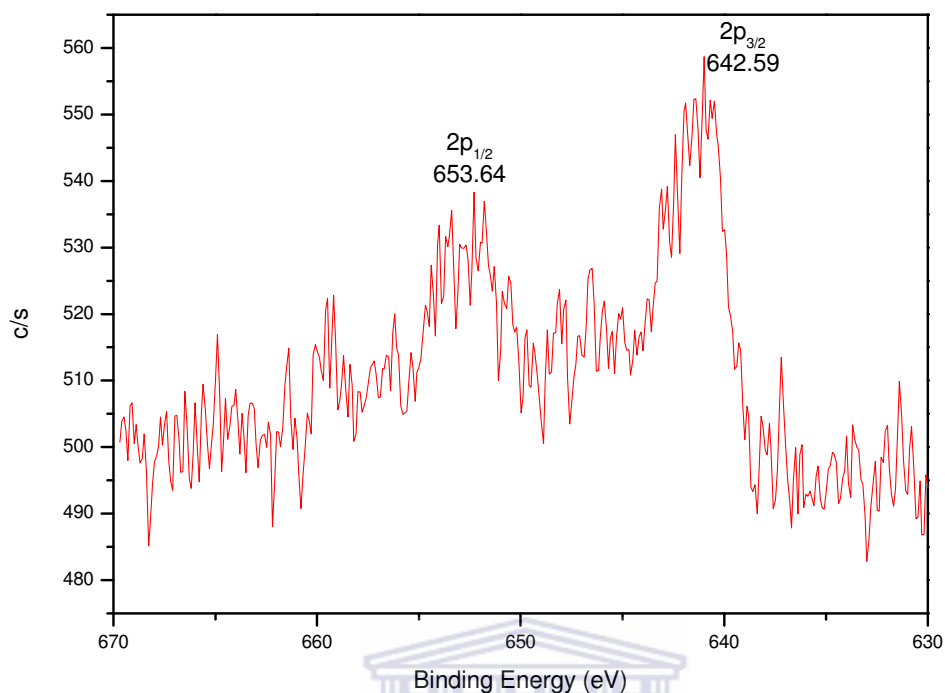


Figure 4. 20: A zoomed XPS spectra from the one in figure 4.16 of MnO_x (x = 1,2) nanostructures with peaks corresponding to reference spectra of MnO₂

Peaks of Mn2p_{1/2} with binding energy of 651.90 eV and Mn2p_{3/2} with binding energy of 640.85 eV were also identified, and they correspond to reference spectra of MnO. The results confirm the presence of MnO₂ in the nanostructures supporting the XRD measurements. Peaks for Al come from alumina (AAO template), Cl from the precursor, C resulted from the residual of oxalic acid during template synthesis and O contributed to the formation of both Al₂O₃ and MnO_x (x = 1,2).

4.3. CONCLUSION

The combinations of parameters suitable for synthesizing an AAO template with a highly ordered hexagonal structure were successfully identified. The results for anodization carried out at 40 V and 50 V in 0.4 M oxalic acid at ± 18 °C hardly produce a template with a highly ordered hexagonal array while anodization at 45 V produced a template with an improved pore hexagonal array. That is, anodization at 40 V produced pores with the average diameter of 40 nm while anodization at 45 V synthesized pores with the average diameter of 45 nm. This observation was in agreement the previous work done on the subject. However, when the voltages were increased from 45 V to 50 V, anodization at 50 V produced pore with an average diameter of 40 nm. This was in contrary to the previous work conducted on the subject. This observation was due to the shift on optimum parameters when only the anodizing voltage is varied while the other parameters are kept constant. Based on these results, the anodizing voltage of 45 V was selected for further investigations. The anodizing temperature lowered to approximately 8 °C and the anodizing was period extended from 60 to 120 minutes. The combination of parameters that successfully produced a template with a highly ordered hexagonal array were identified as follows: (i) the anodizing voltage of 45 V, (ii) 0.4 M of oxalic acid, (iii) temperature of about 8 °C and (iv) the anodizing period of 120 minutes. The average pore diameter of this template was found to be 103 nm.

Prior to deposition of Co and MnO_x ($x = 1,2$), CV measurements were performed to identify the voltages required to deposit these metals. The voltage

of -1.1V was identified for Co deposition while the voltage of +1.1 V identified for MnO_x ($x = 1,2$). The Co and MnO_x ($x = 1,2$) nanostructures were selectively deposited in the pores of the AAO template. The AFM topographies, confirmed that the array on both the Co nanostructures correspond to the ordered hexagonal array of pores of the AAO template. For MnO_x ($x = 1,2$) nanostructures, the hexagonal array could not be clearly distinguished with AFM. Tip artifacts contributed to the poor imaging. However, the SEM results showed the hexagonal array of both Co and MnO_x ($x = 1,2$) nanostructures. The diameter sizes of these nanostructures also corresponded to the pore diameters. EDX analysis confirmed that samples with Co nanostructures constitute Co element while XPS showed the presence of Co and Co_2O_4 . EDX on MnO_x ($x = 1,2$) confirmed the presence of MnO_2 while XPS results showed the presence of MnO and MnO_2 . The peaks corresponding to MnO_2 and the peaks corresponding to Co were identified. XRD results also showed the orientations for Co and MnO_2 .

REFERENCES

- [4.1]. J. P. O'Sullivan and G. C. Wood, Proc. Roy. Soc. Lond. A., 317 (1970) 511 – 543
- [4.2]. J. Choi, Fabrication Of Monodomain Porous Alumina Using Nanoimprint Lithography, Dr. –Ing. Dissertation, Martin-Luther-Universität Halle-Wittenberg, 05/02/2004
- [4.3]. L. Ba and W. S. Li, J. Phys. D: Appl. Phys., 33 (2000) 2527 – 2531
- [4.4]. G.D Sulka, K. G. Parkola, Electrochimica Acta, 52 (2007) 1880 – 1888
- [4.5]. O. Jessensky, F. Muller and U. Gosele, Appl. Phys. Lett. Vol. 72, No. 10 (1998) 1173 – 1175
- [4.6]. M. A. Kashi, A. Ramazani, J. Phys. D: Appl. Phys., 38 (2005) 2396 – 2399
- [4.7]. G. D. Sulka, K. G. Parkola, Thin Solid Films, 515 (2006) 338 – 345
- [4.8]. V. S. Bagotsky, Fundamentals of electrochemistry, Second edition, 2006
- [4.9]. L. H. Mendoza-Huizar, C. H. Rios Reyes, M. Rivera, C. A. Galan-Vidan, Azojomo (ISSN:1833-122X) Vol.3 (2007)1- 11, Doi: 10.2240/Azojomo0233
- [4.10]. J.T. Matsushima, F. Trivinho-Strixino, E.C. Pereira, Electrochimica Acta, 51 (2006) 1960–1966
- [4.11]. International Center for Diffraction Data, Card Numbers: Co[89-7373], Al₂O₃[75-0278], Al₂O₃[47-1770], Cu[3-1015] and Cu[3-1015].
- [4.12]. N. Ikeo, Y. Iijima, N. Niimura, M. Sigematsu, T. Tazawa, S. Matsumoto, K. Kojima, Y. Nagasawa, Handbook of X-ray Photoelectron Spectroscopy, JEOL, 1991

CHAPTER FIVE: MFM ANALYSIS

5.1. INTRODUCTION

The stray field of a magnetic sample can be measured by magnetic force microscope (MFM) that uses a ferromagnetic tip to scan over a samples surface. The interaction forces are obtained from the second derivative of the tip-sample interaction energy, a detailed discussion is in chapter two, section 2.1.3. MFM maps the polar magnetization component to image narrow domains of perpendicular magnetic materials as dark and bright contrasts depending on their polarity. The dark contrasts represent the attractive interactions between the sample and the tip while the bright contrasts illustrate the repulsive interactions between the sample and the tip. The magnetic domains are imaged when MFM operated in the lift mode using phase shift detection. However, imaging magnetic domains of ordered nanostructures with diameter sizes less than 200 nm is still desirable. This is because nanostructures with diameter sizes small than 200 nm are likely to have mono-domains and that three-dimensional nanostructures have different magnetic properties from those of a continuous film.

This chapter presents the results when silicon tips coated with CoCr and Fe thin film were employed to investigate the magnetic behavior of Co and MnO₂ nanostructures. The external magnetic field was applied perpendicular to the sample to ensure that the moments within the domains of the nanostructures

point upwards (perpendicular to the sample surface). The dark or bright contrasts on the MFM image provide information on domain orientations of the nanostructures. The sizes of the domains and the Bloch walls which are transition regions in which the moments change the orientations by 180° measured on the nanostructures will also be presented.

5.2. RESULTS AND DISCUSSION

5.2.1. MFM analysis on Co nanostructures

Prior the investigations, Si tip coated with thin film of Fe was magnetized normal to the sample surface (i.e. in the z-direction) with small magnetic provided by veeco which has a mass of about 4.1 g. The magnet was also used to apply an external magnetic field perpendicular to the surface of Co nanostructures. Figure 5.1 (a) depicts the $2\ \mu\text{m} \times 2\ \mu\text{m}$ AFM height topography of cobalt prepared on alumina, (b) its corresponding MFM image and (c) a zoomed $597\ \text{nm} \times 597\ \text{nm}$ area from square box on an MFM image. From the topography, the average diameter of the nanostructures was 110 nm. The separation distances between the nanostructures were ranging between 12 nm and 20 nm. The corresponding MFM image was obtained using phase shift detection at constant height of 5 nm. The diameters and separation distances of the nanostructures were found to be identical to the ones in the topography.

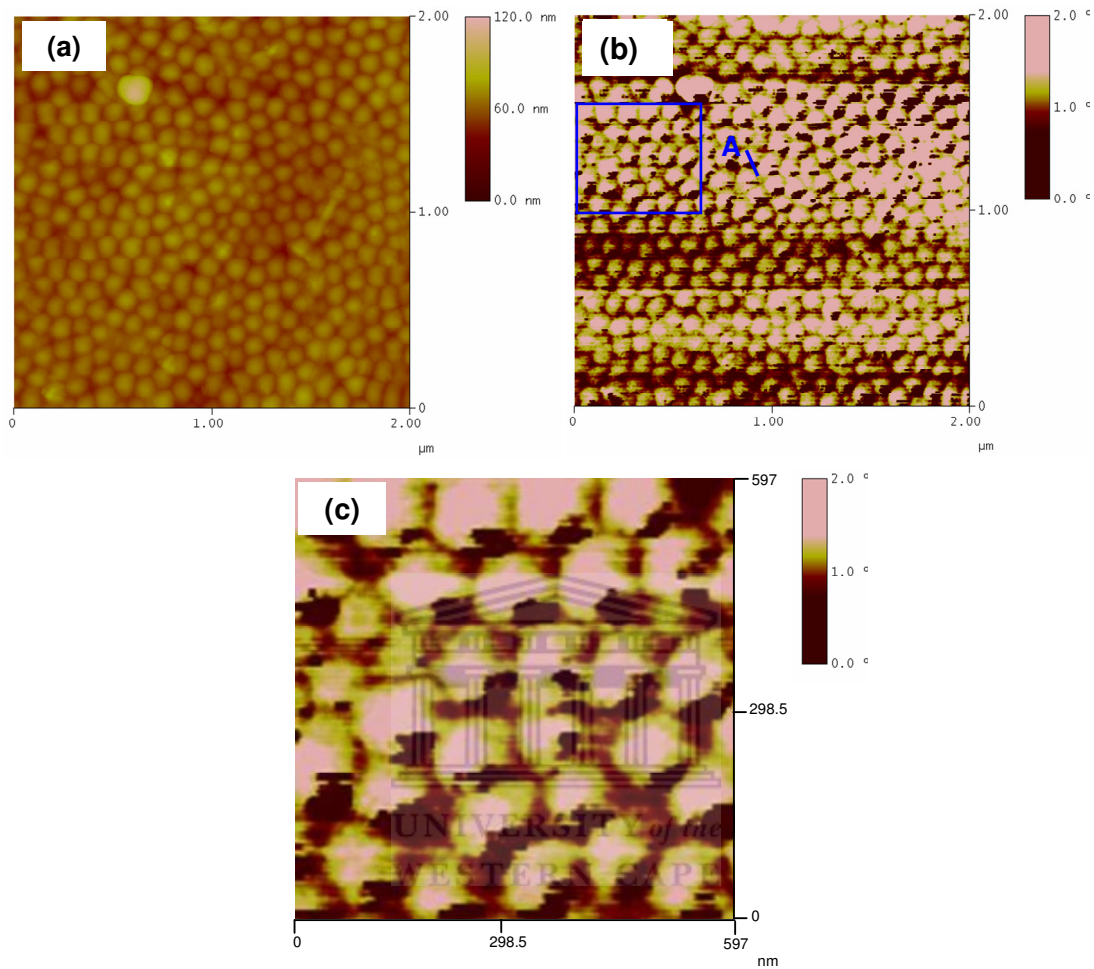


Figure 5. 1: (a) AFM height topography, (b) the corresponding MFM image and (c) a zoomed area from the square box on an MFM image of cobalt nanostructures prepared on AAO template imaged at the lift scan height of 5 nm.

Dark contrasts represent attractive interactions which lead to a negative phase shift while bright contrasts represent repulsive interactions which lead to positive phase shift. The dark and bright contrasts can be clearly seen in figure 5.1(c) which depicts a zoomed 597 nm x 597 nm area marked by square box on

an MFM image in figure 5.1(b). The line profile in figure 5.2 measured on a nanostructure marked “A” in figure 5.1(a) shows a domain with a size of about 33 nm with a phase shift of -0.32° .

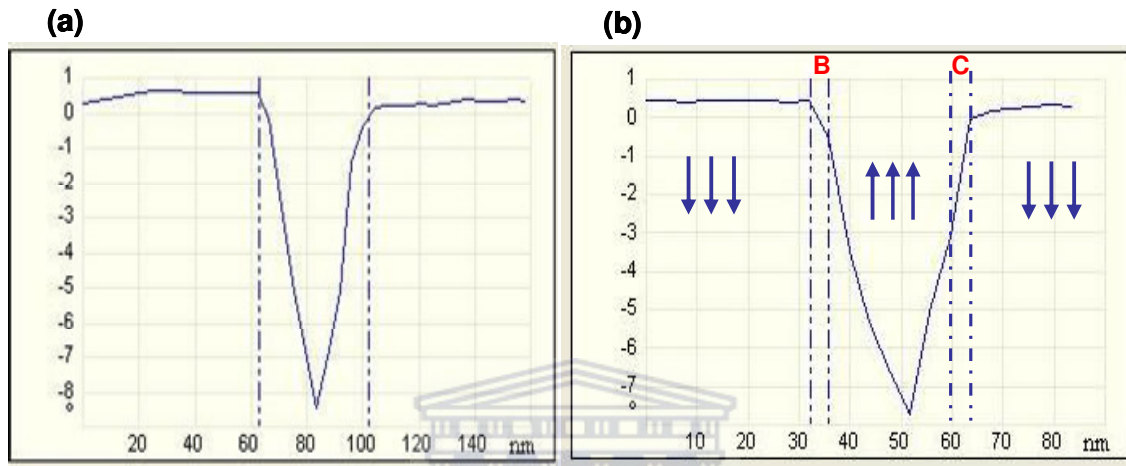


Figure 5. 2: (a) Line profile of the image contrast taken along a line perpendicular to a dark contrast, measured on the nanostructure marked “A” in figure 5.1 and (b) represents both the attractive (upwards arrows) and repulsive (downwards arrows) interactions on the nanostructure.

The areas marked by “B” and “C” in figure 5.2(b) represent the block walls which are the transition regions in which the direction of the moments changes, the detailed discussion is in chapter two section 2.1.2.4. The Bloch wall resulted when the orientation of the moments changed by 180° under a lateral distance of about 4 nm [5.1]. The downwards arrows represent the repulsive interaction (bright contrasts) and the upward arrows represent the attractive interactions (dark contrasts). Measurements on the other nanostructures revealed that the

sizes of the domains were ranging from 20 nm to 70 nm. The measurements on Co nanostructures indicate that dark contrasts represent regions with different orientations of moments from the bright contrasts. These observations confirm the presence of multi-domains in the nanostructures. The existence of multi-domains implies that moments have their preferential alignment when the external field applied perpendicular to the sample surface [5.2] and could also have been brought by the competition between the shape and magnetocrystalline anisotropy.

To further our investigations, the lift height was lowered to 4 nm using the Fe coated tip. Figure 5.3(a) is the 2 μm x 2 μm AFM height topography, (b) its corresponding MFM image and (c) a zoomed 597 nm x 597 nm area from a square box on an MFM image. The average diameter size of Co nanostructures was found to be 106 nm. The separation distances between them were also ranging from 12 nm to 20 nm. The corresponding MFM image shows the dark and bright contrasts with a much improved resolution of the dark contrasts compared to the ones in figure 5.1(b). The dark and bright contrasts can clearly be observed in figure 5.3(c) which represents a 597 nm x 597 nm area zoomed from a square box on an MFM image. The improved resolution was brought by the enhanced detection of magnetic signal when the tip-sample distance was reduced to 4 nm.

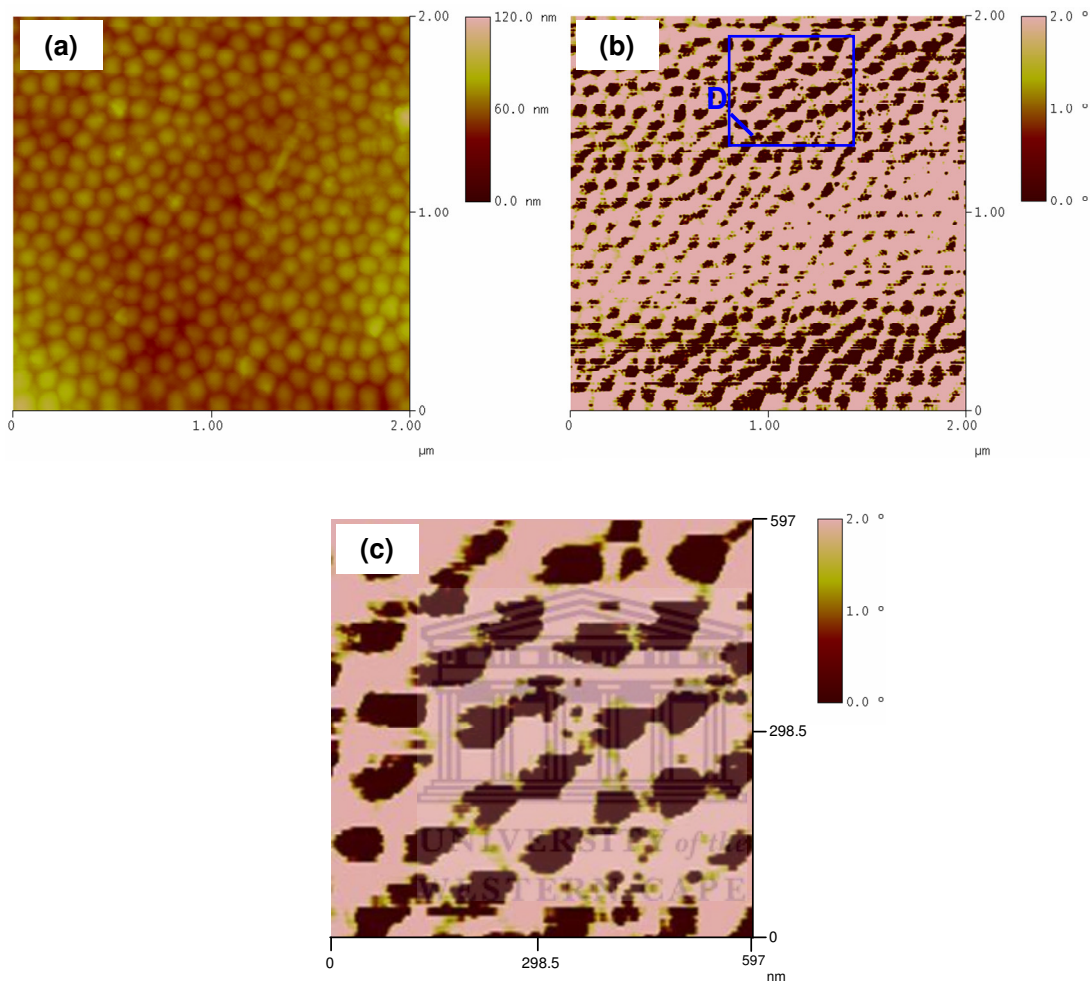


Figure 5. 3: (a) AFM height topography, (b) the corresponding MFM image and (c) a zoomed area of an MFM image of cobalt nanostructures prepared on AAO template imaged at the lift scan height of 4 nm.

Dark contrasts that formed a dark stripes and bright contrasts that formed bright stripes along the nanostructures were observed. Due to the small separation between the nanostructures, the formation of striped dark and bright contrasts can be ascribed to magnetic coupling between the nanostructures [5.3]. The tip acts like a small magnet when brought close to the sample, it influences the

orientations of moments on the sample during the scan and may also have contributed this behavior. Figure 5.4(a) shows a line profile measured on the nanostructure marked “D” in figure 5.3, the size of the domain found to be 49 nm with the phase shift of -0.21° .

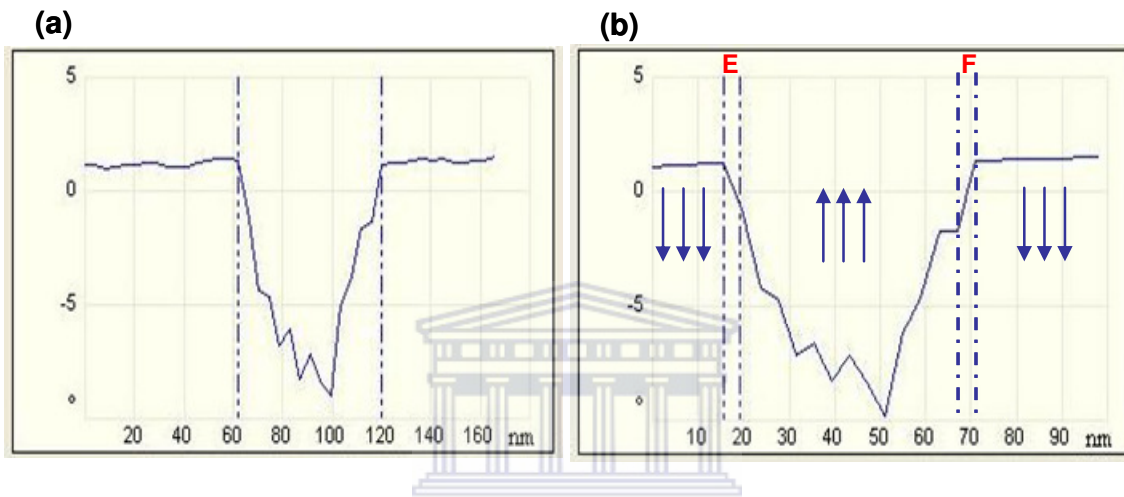


Figure 5. 4: (a) Line profile of the image contrast taken along a line perpendicular to the wall, measured on the nanostructure marked “B” in figure 5.3 (b) illustrates both the attractive (upwards arrows) and repulsive (downwards arrows) interactions on the nanostructure.

The sizes of the domains on other nanostructures were found to be ranging from 20 nm to 86 nm. The areas marked “E” and “F” represent region in which moments changed by 180° within a Bloch wall under a lateral distance of 4 nm. The downward arrows illustrate repulsive interactions while upward arrows depict the attractive interactions. This observation also confirmed the presence of multi-domains in some Co nanostructures caused by preferential alignments of domains when the external field was applied.

5.2.2. MFM analysis on MnO_x ($x = 1,2$) nanostructures

To investigate the MnO_x ($x = 1,2$) nanostructures, CoCr coated tips were used and the constant lift height was 8 nm. The tip was magnetized normal to the sample surface and the external magnetic field was applied perpendicular to the sample's surface. Figure 5.5 illustrates (a) the $2\ \mu\text{m} \times 2\ \mu\text{m}$ AFM topography of the MnO_x ($x = 1,2$) nanostructure, (b) its corresponding MFM image (c) a zoomed $597\ \text{nm} \times 597\ \text{nm}$ area from square box on an MFM image.

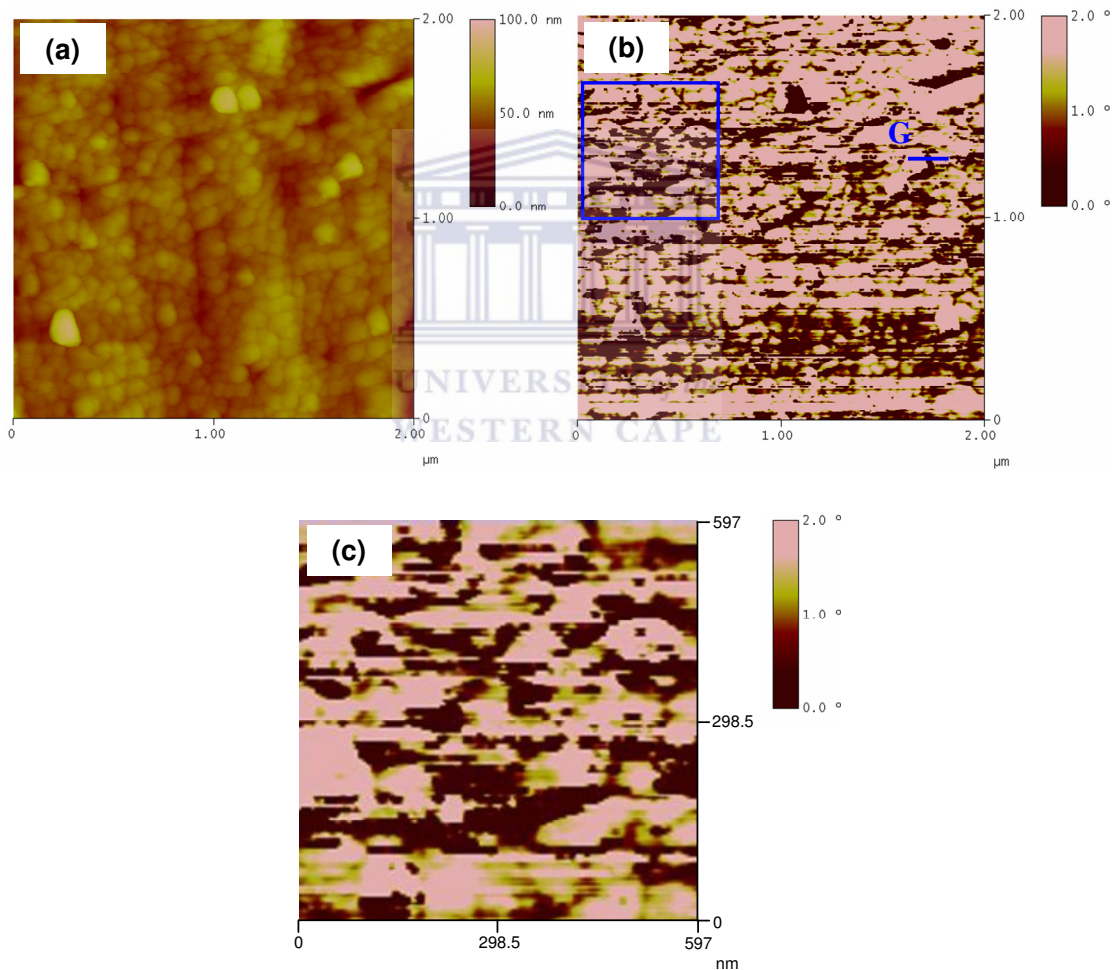


Figure 5. 5: (a) AFM height topography, (b) the corresponding MFM image and (c) a zoomed area from a square box on an MFM image of MnO_x ($x = 1,2$) nanostructures prepared on AAO template imaged at the lift scan height of 8 nm.

From the topography, the hexagonal distributions could not be clearly identified. Nanostructures with diameters sizes that range from 80 nm to 150 nm can be seen. Small separation distances between the MnO_x ($x = 1,2$) nanostructures were observed. The MFM image in figure 5.5(b) depicts some of MnO_x ($x = 1,2$) nanostructures with the dark and bright contrasts. The presences of dark and bright contrasts were due to the preferential alignment of the moments under an external applied field. These contrasts confirm the existence of multi-domains on MnO_x ($x = 1,2$) nanostructures. The line profile in figure 5.6 which was measured on the nanostructure marked “G” in figure 5.5 shows the domain with a size of about 35 nm with the phase shift of -1.32° .

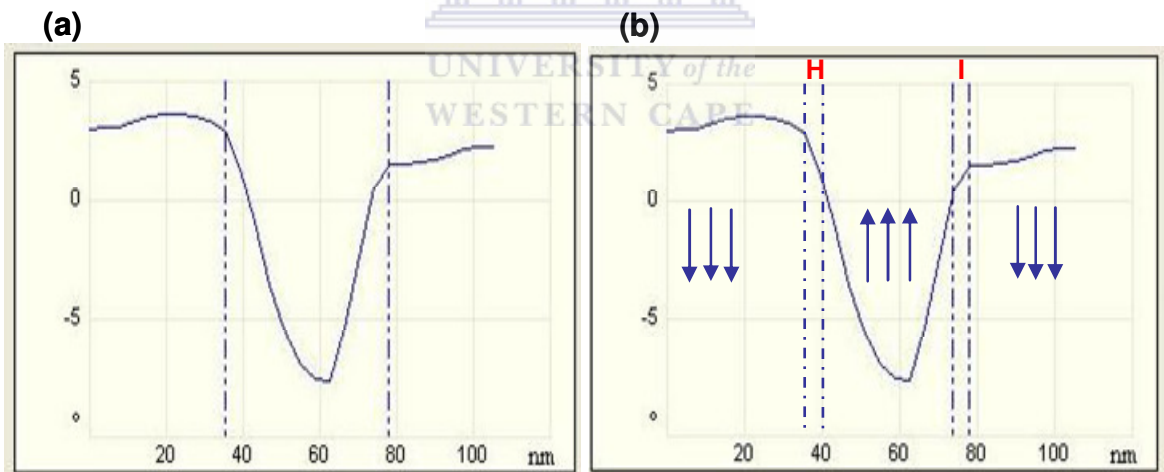


Figure 5. 6: (a) Line profile of the image contrast taken along a line perpendicular to the wall, measured on the nanostructure marked “B” in figure 5.3 (b) illustrates both the attractive and repulsive interactions on the nanostructure.

Figure 5.6 (b) illustrates the regions in which both the attractive interactions (upward arrows) and repulsive interactions (downwards) occurred. The areas marked by “H” and “I” show the regions in which the direction of the moments changes. It was found that the direction of the moments changed by 180° under a lateral distance of 4 nm. Several domains were measured and it was found that their sizes range from 20 nm to 102 nm. Larger domains were mainly observed in the structures larger than 120 nm. The change by 180° occurred under lateral distances of 4 nm within a Bloch found to be independent to sizes of the domains.

5.3. CONCLUSION

The dark and bright contrasts on Co and MnO_x ($x = 1,2$) nanostructures were successfully imaged by magnetic force microscopy (MFM) using Fe and CoCr coated tips respectively. The images for Co nanostructures were obtained when MFM was operated at lift heights of 5 nm and 4 nm using phase shift detection. The dark and bright contrasts confirm the presence of multi-domain on nanostructures of about 100 nm. The existence of multi-domains was due to the preferential alignment of the moments when the external field was applied perpendicular to sample surface and also brought by the competition of the shape and magnetocrystalline anisotropy. The sizes of the domains ranged from 20 nm to 86 nm for cobalt nanostructures. The Bloch walls or regions in which the orientation of the moments changes by 180° under a lateral distance of 4 nm were observed. The MFM image obtained at lift height of 4 nm had the striped

dark and bright contrasts along the Co nanostructures. This behavior was attributed to the magnetic coupling between the nanostructures brought by the small separation distances between them. Lowering the lift height to 4 nm also contributed to the imaging of striped dark and bright contrasts. The tip acts like a small magnet when brought close to the sample, it influences the orientations of moments on the sample during the scan.

Analysis of MnO_x ($x = 1,2$) using a CoCr coated tip also showed the presence of dark and bright contrasts which confirmed the existence of multi-domains on MnO_x ($x = 1,2$) nanostructures. Sizes of the domains ranged from 20 nm to 102 nm where larger domain walls were found in larger nanostructures. The orientation of the moments within a Bloch wall that changed by 180° under the lateral distance of 4 nm was seen.

Both Fe and CoCr coated tips successfully imaged the dark and bright contrasts on both Co and MnO_x ($x = 1,2$) nanostructures which are related to orientations of the magnetic domains. However, the results showed that sharper tips and the lowering of the lift height imaged the domains (dark and bright contrasts) with an improved resolution.

REFERENCES

- [5.1]. C. T. Hsieh, J. Q. Liu, J. T. Lue, *Applied Surface Science*, 252 (2005) 1899 – 1909
- [5.2] M. Kleiber, F. Kummerlen, M. Lohndorf, A. Wadas, D. Weiss, R. Wiesendanger, *Physical Review B*, Vol.58, No.9 (1998) 5563 – 5567
- [5.3] S. A. Koch, R. H. te Velde, G. Palasantzas, J. Th. M. De Hosson, *Applied Surface Science*, 226 (2004) 185–190



CHAPTER SIX: CONCLUSION

Nano-scale magnetism has been the subject of interest since the nineteen fifties due to their potential applications in magnetic storage devices, sensors, etc. Since then, the quest to synthesize nano-scale magnetic particles still continues. This is because smaller particles have higher data storage densities. The properties of these magnetic nanostructures depend on the size, shape, surface roughness and the particles distribution. The magnetic nanostructures are normally prepared by using AAO templates and electron beam lithography.

The magnetic properties of ordered Co structures with diameters larger than 300 nm were widely investigated with magnetic force microscopy (MFM). However, imaging and understanding magnetic structures with diameters smaller than 300 nm still poses challenges. Investigating nanostructures with MFM patterned by AAO template to diameter sizes of 100 nm and separation distances smaller than 20 nm still desirable.

This study focused on finding the combination of anodizing parameters suitable for synthesizing AAO templates with hexagonal pore array using a two-electrode electrochemical cell. The combinations of parameters were varied until the ones that produced a template with ordered hexagonal array were identified. These parameters are anodizing voltage, concentration of the electrolyte, temperature and time. The templates were further used to selectively deposit Co

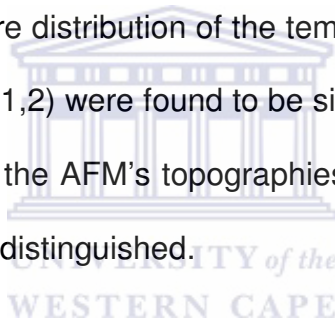
and MnO_x ($x = 1,2$) nanostructures in pore of the template which coated at the bottom by Au-Pd film.

The topographies of the AAO template, Co and MnO_x ($x = 1, 2$) nanostructures were investigated by atomic force microscopy (AFM) and high resolution scanning electron microscopy (HRSEM). X-ray diffraction (XRD), energy dispersive x-rays (EDX) and X-ray photoelectron spectroscopy (XPS) were used to confirm the presence of Co and MnO_x ($x = 1,2$) on the samples. Magnetic force microscopy (MFM) was used to study the magnetic properties of the nanostructures prepared on AAO templates.

The results in chapter four shows that the synthesis of AAO template was successfully conducted using a two-electrode electrochemical cell. It was observed that sizes of pore diameters increased when the anodizing voltage was increased from 40 V to 45 V. However, when anodizing voltage from 45 V to 50 V, sizes of the pore diameters decreased. Optimum parameters that produce a template with a hexagonal pore array were identified as follows: 0.4 M of oxalic acid, anodizing voltage of 45 V, temperature of approximately 8 °C and the period of 120 minutes.

Cyclic voltammetric measurements for Co deposition performed in solution of 0.12 M CoSO_4 and 0.49 M H_3BO_3 depicted that the reduction of $\text{Co}^{2+}_{(\text{aq})}$ to $\text{Co}_{(\text{s})}$ began at -0.9 V when proceeding further to negative voltages. The CV

measurements showed a reversible process. The CV measurements for MnO_x ($x = 1,2$) deposition conducted in a solution of 0.3 M $\text{MnCl}_2 \cdot 4\text{H}_2\text{O}$ showed that reduction of $\text{Mn}^{2+}_{(\text{aq})}$ to MnO_x ($x = 1,2$) commences at +1.16 V, followed by possible deposition of different phases of MnO_x ($x = 1,2$) when proceeding to negative voltages. The CV measurements revealed that the deposition process is irreversible, possibly due to the formation of oxide. The Co and MnO_x ($x = 1,2$) nanostructures were selectively deposited in the pore of AAO template which was coated at the back by Au-Pd film using atomic layer deposition technique (ALD). The array and the diameters of the Co nanostructures were found to correspond to hexagonal pore distribution of the template. The diameters and the distribution of the MnO_x ($x = 1,2$) were found to be similar to those of the template as observed by SEM. From the AFM's topographies, the hexagonal array of the nanostructures could not be distinguished.



In chapter five, MFM analysis on Co and MnO_x ($x = 1,2$) nanostructures illustrated the existence of multi-domains on some nanostructures. It confirmed that, even though the external magnetic field was applied perpendicular to the sample surface, different orientations of the moments in the nanostructures existed. The orientations of the moments which changed by 180° within a Bloch wall under the lateral distance of 4 nm were observed. The sizes of the domains were found to be ranging from 20 nm to 86 nm. It was concluded that the existence of multi-domains in some Co and MnO_x ($x = 1,2$) nanostructures resulted from the preferential alignments of the moments under applied external

field. At lower lift heights, switching of moments on the nanostructures was observed and was induced by the tip. Due to small separation between the nanostructures, the striped dark contrasts, were observed caused by the magnetic coupling between the nanostructures.

Both Fe and CoCr coated tips successfully imaged the dark and bright contrasts on Co and MnO_x ($x = 1,2$) nanostructures. However, Fe coated and lowering of the lift heights imaged the domains (dark and bright contrasts) of the nanostructures with improved resolution. This observation can also be attributed to sharper a tip.

For future work, different tips coated with different magnetic materials will be used to investigate their interactions with the samples. The superlattice of nano-wires will also be synthesized with ALD and dissolve the template to have the free standing nano-wires which can be used in technologies such as: sensors and spintronics of transistors.

APPENDIX A

Conference

3rd Nano Africa conference held at CSIR International Convention Centre, 2009

The 54th Annual Conference of the South African Institute of Physics, University of KwaZulu-Natal (Westville Campus), Durban, 2009

Postgraduate Open Day

The Science Faculty's annual Research Open Day, University of the Western Cape, 2009



Training

Atomic Force Microscopy of Polymers Course, University of Twente, The Netherlands, 2009